Investigation of Nonwetting System Failure and System Integration

A Dissertation
Presented to
The Academic Faculty

By

Peter T. Nagy

In Partial Fulfillment
Of the Requirements for the Degree
Doctor of Philosophy in Mechanical Engineering

Georgia Institute of Technology
December 2006

Investigation of Nonwetting System Failure and System Integration

Approved By:

Dr. G. Paul Neitzel, Chair
School of Mechanical Engineering
Georgia Institute of Technology

Dr. John McCuan
School of Mathematics
Georgia Institute of Technology

Dr. Ari Glezer
School of Mechanical Engineering
Georgia Institute of Technology

Dr. Michael Schatz
School of Physics
Georgia Institute of Technology

Dr. Marc K. Smith
School of Mechanical Engineering
Georgia Institute of Technology

Date Approved: November 14, 2006

To grandma and grandpa in heaven
And my family who have given me the strength
No words can portray my gratitude

A frog in a well cannot be talked with about the ocean. An insect of the summer cannot be talked with about ice. A scholar of limited views cannot be talked with about the Tao. Now you have come forth from between your banks and beheld the great sea. You have come to know your own ignorance and inferiority, and are in the way of being fitted to be talked with about great principles. **Zhuangzi**

ACKNOWLDEGEMENTS

I would like to take this opportunity to thank my adviser Professor Neitzel, who has inspired me through his elegant lectures, engineering philosophy, and guitar playing. Also my appreciation goes to the committee members, Professor Smith, Professor Glezer, Professor Schatz, and Professor McCuan for their support. My appreciation goes to Dr. Dell'Aversana and Dr. van den Doel for their insights into problems I had faced during the courses of research. Special thanks go to Professor Wepfer who accepted me to the ME department at first place. Of course, I could have not made it through without my colleagues; Jason Brown, Maria Carnasciali, Philippe Sucosky, and others with whom I shared the joy of graduate life. Now I look back on experience at Tech and realize that it makes sense.

TALBE OF CONTENTS

ACKNOWLDEGEMENTS **IV**

TALBE OF CONTENTS **V**

LIST OF TABLES **VII**

LIST OF FIGURES **VIII**

1. INTRODUCTION **- 1 -**

1.1. Mechanisms and Failure **- 2 -**
1.2. Application and Failures **- 5 -**
1.2.1. Nonwetting Applications - 5 -
1.2.2. Nonwetting System Failure - 6 -
1.3. Droplet Levitation and Translation for "Lab-On-a-Chip" **- 9 -**
1.3.1. Ideas and Concepts - 9 -
1.3.2. Preliminary Calculations - 14 -
1.4. Chapter Summary **- 16 -**

2. RELEVANT RESEARCH **- 18 -**

2.1. Permanent Nonwetting and Noncoalescence **- 18 -**
2.2. Lab-on-a-Chip and Liquid Handling **- 23 -**

3. NONWETTING-SYSTEM FAILURE **- 30 -**

3.1. Failure load measurement **- 30 -**
3.2. Experimental Apparatus **- 31 -**
3.3. Surface Evolver Computations **- 35 -**
3.3.1. Methodologies - 35 -
3.3.2. Results - 37 -
3.3.3. Shape Instability - 41 -
3.3.4. Correlating Failure Displacement Data to the Load - 46 -
3.3.5. Error Estimate - 48 -
3.4. Experimental Results: Static-Failure **- 50 -**
3.5. Film Failure **- 56 -**
3.5.1. Shear Rate as a Film-Failure Criterion - 58 -
3.5.2. Onset of Film Instability - 64 -
3.5.3. Other Remarks on Film Failure - 67 -
3.6. Pinning Failure **- 68 -**
3.7. Use of a Larger Disk **- 72 -**
3.8. Pendant V.S. Sessile Droplets **- 75 -**
3.9. Shape Transition of the Interface **- 77 -**
3.9.1. Displacement and Load - 77 -
3.9.2. Image Analysis - 79 -
3.9.3. Discussions Based on Normal-Mode Analysis - 82 -
3.9.4. Square-Pattern Formation - 84 -
3.9.5. Discussion - 86 -
3.10. Instability Caused by Anti-Wetting Coatings **- 87 -**

3.10.1. Inferred Evidence of Solutocapillary Effect - 88 -
3.10.2. Visualization of Solutocapillary Effect - 90 -
3.10.3. Hypothesis on Solutocapillarity Effect - 92 -
3.10.4. Discussion - 93 -
3.11. Experimental Results: Dynamic Failure - 94 -
3.11.1. Experimental Procedure - 95 -
3.11.2. Results and Discussions - 96 -
3.12. Concluding Remarks on Nonwetting Failure - 97 -

4. PROFILING OSCILLATING SURFACES - 100 -

4.1. Experimental Methods and Analysis - 101 -
4.1.1. Phase Estimation - 102 -
4.1.2. Phase Scanning Strategy - 103 -
4.1.3. Image Processing - 104 -
4.2. Results - 108 -
4.3. Discussions - 111 -

5. DROPLET LEVITATION AND TRANSPORT - 112 -

5.1. Experiments and Methodologies - 112 -
5.2. Demonstrations - 114 -
5.2.1. Droplet Levitation and Controlled Delivery - 114 -
5.2.2. Notes on the Translational Speeds - 119 -
5.3. Analysis of Levitated-Droplet Oscillations - 121 -
5.3.1. Continuous Oscillation of a Droplet - 121 -
5.3.2. Droplet Moving Away from the Heat Source - 123 -
5.3.3. Simple Model of Droplet Oscillation - 125 -
5.3.4. Discussion - 136 -
5.4. Encapsulation - 136 -
5.5. Levitated Droplet as a Mixing Chamber - 138 -
5.6. Evaporation Rate and Lifetimes of Droplets - 141 -
5.7. Contact Area Analysis - 143 -
5.7.1. Analysis Based on Lubricating Film Pressure - 144 -
5.7.2. Analysis Based on Capillary Pressure - 146 -
5.7.3. Surface Evolver Simulations - 147 -
5.7.4. Discussion on Droplet Squeezing - 150 -
5.8. The Flow Field around a Levitated Droplet - 154 -
5.8.1. Observations - 154 -
5.8.2. Propulsion Estimate Based on Pressure Distribution - 155 -
5.9. Final Remarks on Droplet Levitation - 159 -

6. CONCLUSION AND RECOMMENDATIONS - 161 -

BIBLIOGRAPHY - 163 -

VITA - 169 -

LIST OF TABLES

Table 1. Properties of silicone oils and air used for the computations. - 37 -

LIST OF FIGURES

Figure 1. Experimental observations of permanent (a) nonwetting and; (b) noncoalescence, driven by thermocapillarity. (b) from Dell'Aversana & Neitzel (1998) - 2 -

Figure 2. Drawings of thermocapillary convection within drops of permanent (a) nonwetting and; (b) noncoalescence. The drawings are not-to-scale. (c) is an interferometric visualization of the contact region of a nonwetting system, where each contour represents regions of equal film thickness. High pressure at the symmetry axis creates a dimple on the liquid surface. - 4 -

Figure 3. A high compression introduced on a nonwetting droplet. - 4 -

Figure 4. Dell'Aversana's compass. The magnet is supported by a series of noncoalescing droplets. The image shows bulged free-surface corresponding to the location of droplets, visualized by the presence of the thin film of air. - 5 -

Figure 5. Interferometric observation of the interface shape, which is disturbed by the presence of static charges on the glass surface. Image source: P. Dell'Aversana - 6 -

Figure 6. High speed sequence of a wetting process initiated by the electrical potential. The wetting starts at the center of the droplet where charges accumulate resulting in a Taylor-cone structure on the surface. Image source: P. Dell'Aversana. - 7 -

Figure 7. Interferometric image of a tilted interface. The interference pattern shows non-uniform film thickness just prior to film failure. The height variation is ~ 1.2 μm, determined from the changes in fringe pattern (white to black to white, *etc*.) on the periphery of the dimpled surface. - 7 -

Figure 8. High speed sequence of a) film; and b) pinning failure. Time intervals between the images are 1/2000 and 1/200 seconds, respectively. - 8 -

Figure 9. Demonstration of droplet levitation. The silicone-oil droplet is afloat on top of the bath of same liquid. - 9 -

Figure 10. Conceptual sketch of a droplet levitated above a solid surface. The mechanism is the same as nonwetting drop, except the energy input is derived from an isolated energy source, such as a CO_2 laser. - 10 -

Figure 11. Conventional test surface for LOC systems. Pumping mechanisms are generally required to push liquid through ducts and channels with characteristic dimensions of $O(10 – 100\ \mu m)$. The image is obtained from Agilent Technologies' website. - 11 -

Figure 12. Aqueous solution (dyed for a visualization purpose) engulfed within a nonwetting droplet of silicone-oil. Since these liquids do not mix, contamination on aqueous sample is virtually eliminated. - 11 -

Figure 13. Conceptual sketch of a migrating, levitated droplet. The symmetry in thermocapillary convection is broken due to an offset of the heat spot, leading to jetting of the surrounding gas. - 13 -

Figure 14. Control volume, viewed from top, for estimating the acceleration on a levitated droplet. The droplet is held in place by an application of virtual force.. - 15 -

Figure 15. Isothermal noncoalescence demonstrated by Dell'Aversana, *et al.* (1996). - 19 -

Figure 16. Shapes of an interface at different stages of compression applied on a nonwetting droplet. The captions a, b, and c correspond to 100, 200, and 300 μm. Source: Dell'Aversana, *et al*. (1997). - 20 -

Figure 17. Morphological instability of liquid on an open, curved channel. Instability creates bulges at the corners of the channel, reducing gaps between the liquids. These can be used to mix streams of liquid. Source: Gau, *et al.* (1999). - 24 -

Figure 18. Droplet translation induced by the surface acoustic wave. Image source: Wixforth, et al. (2004). - 25 -

Figure 19. Thermocapillary migration of droplets on a flat surface. (a)-(e) shows a sequence of drop-splitting. (f)-(l) shows translations of the droplet. Source: Darhuber, *et al.* (2003). - 26 -

Figure 20. Water droplet levitated over a radially flowing liquid film. The droplet stays in the region of hydraulic jump. The volume of the droplet is ~0.75 *ml.* Source: Screenivas, et al. (1999). - 27 -

Figure 21. Thermocapillary levitation of a droplet (silicone oil) over the bath of the same liquid. In this case, the temperature of the droplet is kept below that of the bath, resulting in thermocapillary convection flowing in the opposite direction from the one proposed in the present research. Source: Savino, *et al.* (2003). - 28 -

Figure 22. Comparison of loading curves between Surface Evolver (solid lines) and experiments (dots). The plot shows results for three *pendant* droplets of different volumes on a 3 *mm* disk. The curves from left to right correspond to small to large droplets. Source: Dell'Aversana & Neitzel (2004). - 30 -

Figure 23. Schematics of the experimental apparatus. - 31 -

Figure 24. Interference patterns on a nonwetting droplet a) just prior to a loading, with the intensity profile similar to Newton's Ring and; b) after a few-microns displacement, showing a flattened top. - 32 -

Figure 25. (a) Image of a droplet on a 3 *mm* disk. A sharp contrast at the liquid-gas interface is generated by passing light, placed behind the droplet, through a diffusing medium. (b) Binary image after applying MATLAB's edge-detection algorithm. - 34 -

Figure 26. Evolved surfaces of a droplet. (a) Pinned droplet under an action of gravity, without squeezing. (b) Same droplet after some squeezing. The gravity vector is shown as an arrow. - 35 -

Figure 27. Surface Evolver computations of the load on droplets as a function of relative squeezing against a nonwetting plane. (a) Properties of 5 *cSt* silicone oil on a 3 *mm* disk support. (b) 10 *cSt* silicone oil on a 3 *mm* disk support. The legend indicates the size of the volume in mm^3. - 38 -

Figure 28. Surface Evolver computations of the load on droplets as a function of relative squeezing against a nonwetting plane. The result is for 10 *cSt* silicone oil on a 5 *mm* disk support. The legend indicates the size of the volume in mm^3. - 39 -

Figure 29. Surface Evolver computations of the load on droplets as a function of relative squeezing against a nonwetting plane. The result is for *pendant* droplets with properties of 5 *cSt* silicone oil on a 3 *mm* disk. - 40 -

Figure 30. (a) Comparisons of loading characteristics between pendant and sessile droplets for two different volumes. Equilibrium profiles for (b) pendant and; (c) sessile droplets with the volume 8.0 mm^3. - 40 -

Figure 31. Sequence of shape instability from a Surface Evolver simulation. The droplet translates laterally and spills off from the disk. The process effectively reduces the overall energy of the system. Result is from 5 *cSt* silicone oil, with volume 9.0 mm^3, on a 3*mm* disk. - 41 -

Figure 32. (a) Displacement; (b) load; (c) energy and; (d) pinning contact angle at onset of shape instability for various sizes of droplet. The result is for the droplets with the properties of 5 *cSt* silicone oil on a 3 *mm* disk. - 43 -

Figure 33. Diagram showing the relevant parameters to estimate the pinning contact angle at the onset of shape instability. The values were above 90 ° for all the cases. - 44 -

Figure 34. Images of nonwetting droplet (a) in early stages of loading with an axisymmetric profile and; (b) prior to pinning failure with a bulged interface (towards left of the droplet). - 44 -

Figure 35. Energy of the droplet as a function of relative displacement. A sudden decrease in the energy occurs at the instance of shape instability. Arrows indicate before (A) and after (B) shape instability occurring over a 1.5875 μm displacement. Surface Evolver outputs corresponding to these locations are shown on the right. The case is for $\mathscr{V}$ = 5 mm^3, ν_l = 5 *cSt*, *d* = 3 *mm*. - 45 -

Figure 36. Load surface generated from a series of loading curves. The surface is for the case ν_l = 5 *cSt* and *d* = 3 *mm*. Bilinear interpolation is used to determine the failure loading. - 46 -

Figure 37. (a) Illustration of the surface used by the bilinear interpolation. The load is estimated at the data point, $F_e = F_e$ ($\mathscr{V}_e$, $\mathscr{D}_e$). (b) Data point lying outside of interpolation range (red-cross) must be evaluated by extrapolation scheme. - 47 -

Figure 38. Surfaces of (a) $|\partial F/\partial \mathscr{V}|$; (b) $\partial F/\partial \mathscr{D}$ and; (c) w_R. The majority of the error is derived from volume-measurement, indicated by two-order-of-magnitude higher values of $|\partial F/\partial \mathscr{V}|$ than $\partial F/\partial \mathscr{D}$. The result in (c) is for 5 *cSt* oil on a 3 *mm* disk, and is based on $\Delta\mathscr{V}$ = 0.2 mm^3 and $\Delta\mathscr{D}$ = 10 μm. - 49 -

Figure 39. (a)-(c) Failure displacement of nonwetting, silicone oil droplets of ν_l = 5 *cSt* on a *d* = 3 *mm* disk. They correspond to the temperature differences at ΔT = 2, 5, and 20 °C, respectively. (d)-(f) Corresponding failure load. The results are for sessile droplets. - 51 -

Figure 40. (a)-(c) Failure displacement of nonwetting, silicone oil droplets of ν_l = 10 *cSt* on a *d* = 3 *mm* disk. They correspond to the temperature differences at ΔT = 6, 10, and 20 °C, respectively. (d)-(f) Corresponding failure load. The results are for sessile droplets. - 52 -

Figure 41. (a)-(c) Failure displacement of nonwetting, silicone oil droplets of ν_l = 10 *cSt* on a d = 5 *mm* disk. They correspond to the temperature differences at ΔT = 6, 10, and 20 °C, respectively. (d)-(f) Corresponding failure load. The results are for sessile droplets. - 53 -

Figure 42. (a) Failure displacement of nonwetting, silicone oil droplets of ν_l = 5 *cSt* on a d = 3 *mm* disk. The temperature difference is at ΔT = 5 °C. (b) Corresponding failure load. The results are for *pendant* droplets. - 54 -

Figure 43. Film failure loadings for (a) 5 *cSt* and; (b) 10 *cSt* silicone droplets at various ΔT. The diameter of the disk is 3 *mm* for both cases. There is a tendency for the failure load to increase with the temperature, indicating the stability of the film at higher ΔT. - 56 -

Figure 44. Comparison of the film-failure loading between 5 and 10 *cSt* liquids at ΔT = 5 and 6 °C. Higher load carried by 5 *cSt* oil at lower ΔT values indicate more stable film flow due to faster speed induced on the free surface. - 57 -

Figure 45. Isotherms computed from numerical analysis. The temperature gradient is predominantly directed along the axial direction of the droplet. (a) and (b) are the computations extracted from Sumner, *et al.*, (2003) and Monti, *et al.*, (1996). - 59 -

Figure 46. Side views of droplet shapes and estimates of radii of curvatures. These outputs from Surface Evolver show the shapes of squeezed droplets at film failures. (a) and (b) correspond to $\mathscr{V}$ = 6.75 and 3.36 mm^3, respectively. - 60 -

Figure 47. Contact radius as a function of displacement computed from Surface Evolver. The radius is evaluated at 10 μm below the nonwetting plane (or the top of the flattened droplet). The egends are the sizes of the volume in mm^3. - 61 -

Figure 48. Initial heights of droplet on d = 3 *mm.* "S" and "P" *are* used to indicate sessile and pendant droplets, respectively, in the legend provided in (a). - 62 -

Figure 49. Shear rate corresponding to film and pinning failures for various similar systems with d = 3 *mm.* S and P are used to denote sessile and pendant droplet systems, respectively. - 63 -

Figure 50. (a)-(c) Growth of disturbance visualized from fringe patterns. (a)-(b) Disturbance starts to grow at top right corner of an uneven film, reducing the film thickness locally. (b)-(c) Propagation of disturbance into azimuthal direction. After the image in (c) wetting takes place. The wetting event cannot be resolved by the regular frame camera used for this recording. Time interval between each frame is 1 *s*. - 65 -

Figure 51. (a) Coordinate system used for the analysis of the disturbance growth. (b) Temporal changes in the interface positions as a function of time. The wave propagates in azimuthal direction, along the periphery of the dimpled interface. - 66 -

Figure 52. Pinning-failure load for (a) 5 and; (b) 10 *cSt* silicone-oil droplets at various ΔT. The diameter of the disk is 3 *mm* for both cases. Experimental load data is compared to the load at the onset of shape instability obtained from Surface Evolver. - 68 -

Figure 53. Pinning contact angles computed from Surface Evolver at failure displacement. The contact angle is small when the temperature difference is also small. The results are compared to the values at the onset of shape instability obtained from Surface Evolver. - 70 -

Figure 54. Comparison of pinning-failure loadings between two systems at ΔT = 20 °C. Given the tendency, where higher load is sustained by 10 *cSt* silicone oils, a dynamically similar system seems impossible between 5 *cSt* at ΔT = 20 °C and 10 *cSt* at ΔT = 40 °C. - 71 -

Figure 55. Temporal variation of pixel intensity at the periphery of the dimple on a droplet. The data is taken from a 10 *cSt* droplet on a 5 *mm* disk. - 73 -

Figure 56. 1st mode characteristic frequency of isothermal, pinned droplet on a disk of different diameters. The frequency decreases with the increase in the surface area, and thus the capillary pressure, which results due to an increase in the volume size. - 74 -

Figure 57. Comparison of (a) failure displacement; (b) film-failure loading and; (c) pin-failure loading between pendant and sessile droplets. The case is for ν_l = 5*cSt*, *d* = 3*mm*, ΔT = 5 °C. - 76 -

Figure 58. Fringe patterns (a) before and; (b) after the shape transition obtained from a smaller droplet. The transition process takes about 1 *s* to complete. - 77 -

Figure 59. (a) Displacement and; (b) load of shape transition of various nonwetting systems. The legend indicates the viscosity and the temperature difference of the systems in the present analysis. - 78 -

Figure 60. Marangoni number at the onset of shape transition, plotted against a dimensionless volume parameter ($\mathscr{V}/R_0^3$). - 79 -

Figure 61. Fringe pattern at the onset of shape-transition process. The interfacial structure is reconstructed in the highlighted region. The fringe patterns outside this region are not resolved due to a high curvature of the free-surface of the droplet. - 80 -

Figure 62. Fringe patterns from three instances of time, corresponding to (a) $t = 0$; (b) $t = 1$; (c) $t = 2.5$ *s*. (d) Spatio-temporal representation of the fringe pattern at the center of the droplet. The dotted lines in (a)-(c) are also drawn in (d). *r* and *t* are the radial and time axes, respectively. - 81 -

Figure 63. Shape of the interface reconstructed from the spatio-temporal interferogram in Figure 62(e). The free-surface is displaced by ~ 5 μm towards the glass surface, placed somewhere above this image, as the time elapses. The entire process takes about 3 seconds. - 82 -

Figure 64. (a) Raw interferogram at $t = 0$ *s* and; (b) its power spectrum showing the components of frequency. (c), (d) Same analysis at $t = 2.88$ *s*. The power is concentrated in the lower spectrum in (d) than (b), indicating a flatter interfacial shape after the shape transition. - 83 -

Figure 65. (a)-(c) Various interface shapes exhibited by a shallow nonwetting droplet by imposing a high temperature gradient. The relative displacement increases from (a)-(c). The interface shown in (b) is unsteady. - 84 -

Figure 66. Transition in the square-cell patterns in Bérnard-Marangoni convection. (a) and (b) corresponds to Ma ~ 410 and ~ 688, respectively. Source: Schatz & Neitzel (2001). - 85 -

Figure 67. Comparisons of failure (a) displacement and; (b) loading between two coatings. The result is for a system with $\nu_l = 5$ *cSt*, $\Delta T = 20\ ^{o}$C, $d = 3$ *mm*. The new data include film failures, which did not occur with Scotchgard. - 88 -

Figure 68. Comparisons of failure (a) displacement and; (b) loading between two coatings. The result is for a system with $\nu_l = 10$ *cSt*, $\Delta T = 20$ °C, $d = 3$ *mm*. - 89 -

Figure 69. (a) Raw interferogram showing solutocapillary effect on the free surface of a nonwetting droplet. (b) Center region affected by the solutocapillary flow. (c) The shape of the interface obtained from (b). - 91 -

Figure 70. (a)-(c) Same as Figure 69 after an additional squeezing was applied to the same droplet. - 92 -

Figure 71. (a) Surface-tension gradients generated by thermocapillary (TC) and solutocapillary (SC) effects on top-center of a nonwetting droplet. (b) Non-uniformity of the concentration gradient introduces pressure variations on the free surface. Chemical species are indicated by ball-squiggle shape, and the magnitude of the gradient-vectors is indicated by the length of the arrows. - 93 -

Figure 72. Experimental apparatus used for the measurement of failure under dynamic environment. The rest of the system remains the same as the one used for the static-failure experiment. - 95 -

Figure 73. Comparison of the failure displacement of static and dynamic systems for $\nu_l = 10$ *cSt*, $\Delta T = 20$ °C, $d = 3$*mm*. The forcing frequency is at 60 *Hz*. - 96 -

Figure 74. High-mode excitation of isothermal, pinned droplet, showing an azimuthal component of the free-surface response. - 97 -

Figure 75. (a)-(c) Raw fringe patterns taken from the recorded sequence of the forced oscillations, excited at 17 *Hz.* (d) Spatio-temporal interferogram constructed from the recording. The dotted lines correspond to those shown in (a)-(c). (e) Interferogram after image processing. The dashed line is used to define the region containing the phase information. Source van den Doel, *et al.,* (2005) - 105 -

Figure 76. Same as Figure 75, except the sequence contains the damped oscillation towards the end of the recording. The input frequency is 54 *Hz.* - 106 -

Figure 77. Reconstructed shape of interface during the (a) forced and ;(b) damped oscillations. The forcing frequencies are about 17 and 54 *Hz,* respectively. - 108 -

Figure 78. (a) Amplitude response of the surface at the center of the droplet from the forced oscillation. (b) Power spectrum of the Fourier-transformed signal of the oscillation shows the maximum peak around 17 Hz *and* small contributions from higher frequencies at 33 and 50 *Hz.* - 109 -

Figure 79. (a) Amplitude response of the surface at the center of the droplet from the damped oscillation. The forcing is terminated roughly around t = 0.06 *s.* (b) Power spectrum of the Fourier-transformed signal during the forced-portion of the oscillation shows the dominant peak around 54 *Hz* with contributions from higher frequencies at 108, 162, and 216 *Hz.* - 109 -

Figure 80. Power spectrum corresponding to the freely-decaying portion of the damped oscillation. The data is taken from (t > 0.07 *s)* of the original data presented in Figure 79(b). This graph shows a single peak around 67 *Hz,* which could correspond to the natural frequency of the system. - 111 -

Figure 81. Schematic of an experimental apparatus used for droplet levitation and transport. A CO_2 laser is used for the heating of the silicone oil, and a steerable mirror is used to control the position of the laser beam on the glass surface. - 112 -

Figure 82. Droplet levitated above a glass surface. The viscosity is 5 *cSt* and the diameter of the droplet is about 1.6 *mm.* - 114 -

Figure 83. (a) Image showing a droplet from three instances in time. The positions of the droplet, from left to right, correspond to time at t = 0, 18.5, and 37 *s.* (b) shows the history of the droplet position, measured from the left edge of the image, as a function of time. - 115 -

Figure 84. Image sequences (a)-(f) showing a levitated 5 *cSt* silicone droplet moving in a circular path. Condensation is observed on the cooled glass surface, which comes from the warmer levitated droplets. - 117 -

Figure 85. Image sequences (a)-(f) showing a levitated 10 *cSt* silicone droplet moving in a (∞) path, rotated by 90°. Again, condensation from the warmer droplet is observed on the cooler glass surface, helping to visualize the path. - 118 -

Figure 86. Sketch of a levitated droplet oscillating about the heat source. The intensity profile of the laser beam is approximately Gaussian. The diameter of the beam is ~3 *mm* where as the droplet is ~1.6 *mm.* - 120 -

Figure 87. Image analysis of the droplet's oscillatory behavior. (a) The original image from the recording used to define the coordinate system. Data corresponding to the droplet's; (b) x-component of the position, velocity and acceleration and; (c) y-component of the position, velocity and acceleration. The spline function is used to fit the raw position data for velocity and acceleration computations. - 122 -

Figure 88. Plots showing position, velocity, and acceleration of a droplet heated above some threshold value. As a result of overheating, the droplet is accelerated and escapes from the heat source. (a) shows the coordinate system used for the image analysis. (b) plots the positions of droplet as a function of time, starting at $(x,y) = (0,0)$. (c) shows the x- and y-components of the position, velocity, and acceleration of the droplet as a function of time. The position data are fitted and they are used to compute the velocity and acceleration. - 124 -

Figure 89. Result of the droplet dynamics around the heat spot. The Stokes drag is used for the present analysis. The system shows characteristics of an underdamped oscillation. - 130 -

Figure 90. Result of the droplet dynamics around the heat spot. The drag coefficient is adjusted to $C_1 = 4\pi$. The system exhibits less effective damping than the one with the Stokes drag, indicated by higher velocity at the end of integration period, $t = 30$ *s*. - 131 -

Figure 91. Drawing showing droplets with perfect (bottom) and imperfect (top) thermal responses. The arrows indicate the forcing vectors as a function of three positions. The forcing on the perfect drop switches the sign as it passes $x = 0$, whereas a delay is expected for a realistic droplet. - 132 -

Figure 92. Transformation of droplet position used for the modified model. The modification mimics the latent thermal response of an actual droplet. - 133 -

Figure 93. Result from the modified model. Due to the delayed thermal response, the droplet is set into a continuous oscillation. - 134 -

Figure 94. Simulation of a droplet with a sluggish thermal response ($C_2 = 1.7$). The droplet escapes from the energy source and never returns to oscillation. - 134 -

Figure 95. Simulation where a droplet diverts from the heat source after a sudden increase in the energy input at $t = 20$ *s*. The increase in the energy is imitated by an increase in the value of $\Delta T_0 = 30$ to 40 °C. The model uses the Stokes drag law and $C_2 = 1.0$ for the thermal response. - 135 -

Figure 96. An encapsulated water droplet within a levitated 10 *cSt* silicone oil droplet. - 137 -

Figure 97. Merging of two levitated droplets, demonstrating a possible use of the coalesced droplet as a mixing chamber. A step function is used to levitate two droplets simultaneously, where the amplitude of the voltage is reduced to approach them together as seen in (a)-(c). The droplets are observed to oscillate about the heat spot due to an excess energy received from the laser. This oscillation is minimized by reducing the energy input. - 139 -

Figure 98. Various collision regimes of hydrocarbon droplets in 1 atm. air. Regimes (I) and (III) are coalescence, (II) is bouncing, (IV) is near head-on separation and (V) is off-center separation. The results from Qian & Law, (1997). - 140 -

Figure 99. Changes in square of diameter of a levitated droplet over a period of ~ 1 *hour*. A consistent evaporation process reduces the diameter from 1.6 to 1.5 *mm*. 5 *cSt* silicone oil, which is more volatile than 10 *cSt* oil, is used for this experiment. - 143 -

Figure 100. Schematics showing the force balance of a levitated droplet. The weight of the droplet is balanced by the lubricating pressure acting over the contact area. - 144 -

Figure 101. Static droplet profiles computed from Surface Evolver. The volumes (and the radii) are (a) 2.5 (0.81); (b) 1.25 (0.67); (c) 0.6 (0.52) and; (d) 0.005 (0.106) mm^3 (*mm*). These images are to-scale to one another. - 147 -

Figure 102. Sizes of contact radii as a function of the droplet radii. The data from Surface Evolver are shown as the dotted legend. The two scaling arguments are used for the fits through the data points. In addition, the result from Charles & Mason (1960) (C&M in the legend) is compared with the data from Surface Evolver. - 148 -

Figure 103. Flattened droplet with original radius R_d, squeezed by applying a force, F. The flattened droplet has a height $2H$, with the contact radius R_c. - 151 -

Figure 104. Ratio of the forces from lubricating film and that required to induce deformation. The properties of 5 *cSt* silicone oil and air at 25 °C are used, with the initial droplet radius of 100 μm and ΔT = 10 °C. - 153 -

Figure 105. (a) Flow visualization of around a statically levitated droplet. The incense particles trace out a circular path, driven by the free-surface motion of the droplet. Due to symmetry in the flow (and pressure) field, the droplet can be positioned stably at this location even when there is air current to push the droplet off from the heat source; (b) schematics of a generalization of axisymmetrical flow pattern around the droplet. - 154 -

Figure 106. Spherical coordinate-system used for the estimate of the propulsive force. The shape of the droplet is assumed to be spherical. - 156 -

Figure 107. Variation of the surface-velocity profile around the azimuthal direction on the free surface of the droplet. - 158 -

LIST OF SYMBOLS

A	Amplitude
A_c	Contact area of a nonwetting droplet
A_f	Amplitude of forcing at failure
A_1	Background illumination
A_2	Amplitude modulation
a	Acceleration
B	Ratio of lengths between the centers of masses and the sum of the radii of droplets
Bo	Bond number
b	Damping rate
C_1	Drag constant
C_2	Constant
Ca	Capillary number
D	Droplet diameter
$\mathscr{D}$	Displacement
$\mathscr{D}_e$	Displacement data from experiment
$\mathscr{D}_{eq}$	Equivalent displacement
$\mathscr{D}_{1,2}$	Displacement below, and above the data point $\mathscr{D}_e$, respectively at $\mathscr{V}_1$
$\mathscr{D}_{3,4}$	Displacement below, and above the data point $\mathscr{D}_e$, respectively at $\mathscr{V}_2$
$\Delta\mathscr{D}$	Error estimate in a measurement of the relative displacement
d	Diameter of the disk support where a nonwetting droplet is pinned
E	Energy
$\hat{e}_x$	Unit vector in x-direction
$\hat{e}_r$	Unit vector in r-direction
F	Force
$F_{A,B}$	Interpolated force at $(\mathscr{V}_1, \mathscr{D}_e)$ and $(\mathscr{V}_2, \mathscr{D}_e)$, respectively
F_e	Force estimated at location $(\mathscr{V}_e, \mathscr{D}_e)$ from bilinear interpolation
F_{lub}	Lubricating force
F_{drag}	Drag force
f	Frequency
g	Gravity constant ($= 9.81\ m/s^2$)
H	Height of a droplet
H_0	Height of an undeformed droplet
h	Height
I	Intensity
I_0	Intensity of the laser at the center ($x = 0$)
K_{evap}	Evaporation rate
k	wave number in radial direction
L	Effective radius of a Gaussian profile
l	Length scale associated with the cross section of a duct
l_{cap}	Capillary length scale

m	Wave number in azimuthal direction
Ma	Marangoni number
N	Random noise in a raw image
n	Wave number in axial direction
P_{cap}	Capillary pressure
P_{lub}	Lubricating pressure
P_s	Gage pressure on the free surface of a droplet
ΔP	Pressure jump across an interface
q	Marker function for indicating worked pixel
r	radius
R_0	Radius of the disk support
R_a, R_b	Principle radii of curvature
R_c	Radius of the contact area (or equivalently radius of curvature)
R_d	Radius of undeformed droplet
R_p	Radius of circumference
$\underset{\sim}{S}$	Surface-area vector
S_x	Standard deviation characterizing the waist of laser beam
s	Growth rate of disturbance
T	Temperature
T_C	Temperature of a cooler surface in a nonwetting/noncoalescing system
T_H	Temperature of a warmer surface in a nonwetting/noncoalescing system
T_0	Reference temperature or room temperature ($25\ \text{C}^{\text{o}}$)
ΔT	Temperature difference
ΔT_0	Arbitrary temperature difference on a droplet at the center of the laser beam
t	Time
t_{cap}	Capillary time scale
t_ν	Viscous time scale
t_θ	Time scale associated with thermocapillary convection
U_d	Droplet velocity
U_e	Fluid velocity at the outlet region 2 of the control volume analysis
U_i	Fluid velocity at the inlet region 1 of the control volume analysis
U_s	Speed of the free surface driven by thermocapillary convection
U_w	Speed of a moving wall
U_θ	Speed of the free-surface of a droplet
U_ϕ	Meridional component of the free-surface speed
$\underset{\sim}{u}$	Velocity vector
$\underset{\sim}{u}'$	Disturbance velocity vector
$\underset{\sim}{\hat{u}}$	Amplitude vector of the disturbance
$\mathscr{V}$	Volume of a droplet
$\mathscr{V}_e$	Volume data from experiment
$\mathscr{V}_{1,2}$	Volume below and above $\mathscr{V}$

$\Delta\mathscr{V}$	Error estimate in a volume measurement
V	Voltage
V_0	Voltage input for *x*- and *y*-axes
W	Work
W_d	Weight of a droplet
We	Weber number
w_R	Total uncertainty in a measurement
x	Position or a coordinate
$\hat{x}$	Transformed coordinate
X_d	Position of a droplet
X_0	Amplitude of sinusoidal motion of a droplet
z	Coordinate
α	Thermal diffusivity
β	Regularization coefficient
χ	Phase offset
δ	Average film thickness
∇_s	Surface Laplacian
ε	Pixel coordinate inside region Ω
ϕ	Phase or meridional angle
ϕ_0	Estimated phase from the minimization algorithm
γ	Temperature coefficient of surface tension ($= \partial\sigma/\partial T$)
η	Pixel coordinate inside region Ω
λ	Wavelength
μ_l	Viscosity of liquid
μ_g	Viscosity of gas
μ	Ratio of viscosity = μ_g / μ_l
ν_l	Dynamic viscosity of liquid
ν_g	Dynamic viscosity of gas
θ	(Azimuthal) Angle
θ_p	Pinning angle
ρ_l	Density of a liquid
ρ_g	Density of gas
$\Delta\rho$	Density difference ($= \rho_l - \rho_g$)
σ	Surface tension
σ_0	Surface tension at reference (room) temperature
τ_l	Shear stress on liquid phase
ω	Circular frequency
ξ	Speed parameter
Ω	Summation region
Ψ	Cost function

ψ Angle (= $\pi - \theta$)
$\zeta_{1,2}$ First order plane used to estimate the phase

SUMMARY

A droplet may be prevented from wetting a solid surface by the existence of a lubricating film of a different fluid, such as air, between the droplet and solid surfaces. In this research, thermocapillarity is exploited to induce free-surface motion on a droplet, dragging air with it. The noncontact nature and the load-carrying capability of a nonwetting droplet lead to potential engineering applications, *e.g.*, low-friction bearings. The present research consists of two thrusts. The first is aimed at quantifying nonwetting-system failures (film and pinning) triggered by application of a mechanical load, gaining insights to failure mechanisms. Experimental results show that film failure occurs over a wide range of droplet volumes when the temperature difference ΔT between the droplet and the plate, the driving potential of the free-surface motion, is small. Interferometric observations reveal flow-instability just prior to film failure, with the growth of a nonaxisymmetric disturbance on a free surface ($m = 1$). Pinning failure becomes more prevalent as ΔT is increased, stabilizing the film flow. As part of the present investigation, a system was devised, allowing an oscillating free-surface to be reconstructed from a series of interferograms. The dynamic responses of the free surface reveal mode coupling, with harmonics of the input frequency excited through nonlinearity.

The second thrust of the research succeeded in levitating and translating a droplet using the mechanism of permanent nonwetting. In this scheme, the droplet is heated by a CO_2 laser and is placed above a cooled glass surface in order to drive the lubricating film that supports the weight of the drop. Furthermore, the position of the droplet can be controlled by moving the heating location, which leads to an asymmetry of the flow fields, driving air from the cooler-end of the droplet and propelling it towards the heat source. These demonstrations suggest the technique's potential use as a liquid-delivery scheme in a Lab-On-a-Chip system. Modeling is carried out to estimate propulsive forces on the droplet and to explain oscillatory behavior observed when excessive heating is applied on the drop. The concept to sandwich a droplet between two plates, a necessary configuration for levitating smaller droplets (less than *mm*-scale), is also discussed.

1. Introduction

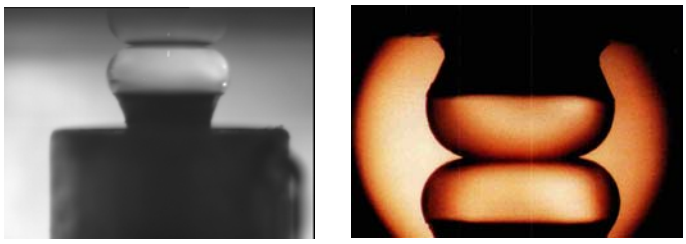
The phenomena of permanent nonwetting and noncoalescence owes to a thin film of air that continuously lubricates the space between the droplet and another surface of concern (Dell'Aversana, *et al.* (1996)). The focus of the present research is on nonwetting systems that exploit thermocapillary convection as the driving force, which sets the surrounding air into motion. Under restricted conditions, the supply of air is maintained by the intrinsic nature of the system: The variation of temperature on the surface of a droplet autonomously keeps thermocapillary convection in motion, lubricating the gap that separates the two surfaces of interest, and thus preventing them from making molecular contact. These systems are sometimes referred to as "self-lubricated" system (Dell'Aversana, *et al*.).

Due to their low-friction, non-contact nature and their ability to sustain loads, self-lubricating systems can potentially be used as low-friction bearings in low-load applications. In addition, an effective energy dissipation of tiny droplets can be exploited as a mechanical damper. One of the aims of this research is to promote the use of a permanent nonwetting droplet in such load-bearing systems. In order to optimize their designs, it is necessary to quantify the failure criteria associated with the application of mechanical loadings on a nonwetting droplet and to characterize the surface dynamics within the contact region. The result from this study will provide application-engineers an operation range in which nonwetting is assured.

Another part of this research aims to demonstrate the concept of droplet levitation and controlled translation. This concept is derived from the underlying physics of permanent nonwetting; the weight of the droplet is supported by a film of air driven under the droplet via thermocapillary convection. The concept is very useful in a Lab-On-a-Chip (LOC), where small biological and chemical specimens are moved from one location to another for laboratory testing purposes. Because a levitated droplet is not in a direct physical contact with the test surface, droplet contamination is minimized or eliminated, and allows for a droplet to be placed anywhere on the surface, which is difficult with the conventional fluid-delivery schemes proposed by different researchers.

1.1. Mechanisms and Failure

Temporary noncoalescence can be observed in many parts of our daily lives. For example, a swimmer, breathing sharply on the pool surface, can observe tiny beads of droplets being ejected from the pool and staying afloat over it for a short period of time before coalescing. The temporary nature of these noncoalescing droplets is explained by the momentary presence of an air film between the droplet and the pool surface. This film acts as a cushion, keeping the surfaces of concern apart from each other. As time elapses, the droplets settle under the action of gravity, squeezing the air in the interface until the two bodies merge due to intermolecular forces.



(a) (b)

Figure 1. Experimental observations of permanent (a) nonwetting and; (b) noncoalescence, driven by thermocapillarity. (b) from Dell'Aversana & Neitzel (1998).

In cases of permanent noncoalescence and nonwetting, where a droplet is prevented from wetting a solid surface (Figure 1 (a)) or from coalescing with the same liquid body (Figure 1 (b)), there is a constant supply of air between the surfaces of concern. The flow of air continuously lubricates the interface, preventing the surfaces from touching indefinitely. This feat is accomplished by a tangential motion of either one or both of the two involved surfaces, which helps to drag the surrounding air between the mating surfaces. The focus of the present research is on the system of permanent nonwetting, which can be realized by exploiting thermocapillary convection to set the necessary tangential motion on the free surface of the droplet.

Thermocapillary convection is set by exploiting the thermocapillarity of a liquid, which describes the surface tension's dependency on the temperature. A simple relationship can be expressed as

$$\sigma = \sigma_0 - \gamma\left(T - T_0\right) \qquad (1)$$

where σ and σ_0 are the local and reference surface-tension forces evaluated at the local and the reference temperatures, T , and T_0 , respectively, and $\gamma\left(=-\partial\sigma/\partial T\right)$ is the temperature coefficient of surface tension, which exhibits an inverse relationship with temperature ($\gamma > 0$) in common liquids. As a consequence, an imposed temperature-gradient on a free surface of a liquid will result in a surface-tension gradient opposing it, pulling the surface towards the regions with higher surface tension (lower temperature). Through the action of viscosity, the fluid layers (both liquid and gas) adjacent to the free surface are set into a motion called thermocapillary convection.

To achieve a state of permanent nonwetting or noncoalescence by exploiting thermocapillarity, a heated droplet is placed near a (solid- for nonwetting, liquid- for noncoalescence) surface at a lower temperature. A locally cool spot having a high surface-tension is generated on the apex of the heated droplet near the contact region. Owing to thermocapillarity, the surface of the droplet is pulled from the heated region at the disk support towards the apex of the droplet. The surrounding air is dragged by the free-surface motion, moving towards the center of the contact region, where it reverses and exits again from the entrance region. The sketch in Figure 2(a) is used to show the sense of thermocapillary convection within a nonwetting system at the contact region. In the case of a noncoalescing system, the flow of air is aided by counter-rotating convection in the adjacent, cooler droplet as shown in the sketch of Figure 2(b). A dimple is formed on the free surface of a nonwetting droplet due to a high pressure exerted at the center of the contact region where the flow reverses its direction. The deformed interface structure can be interpreted from the interferometric image presented in Figure 2(c), where each interference pattern (black or white line) corresponds to a contour of the liquid-gas interface.

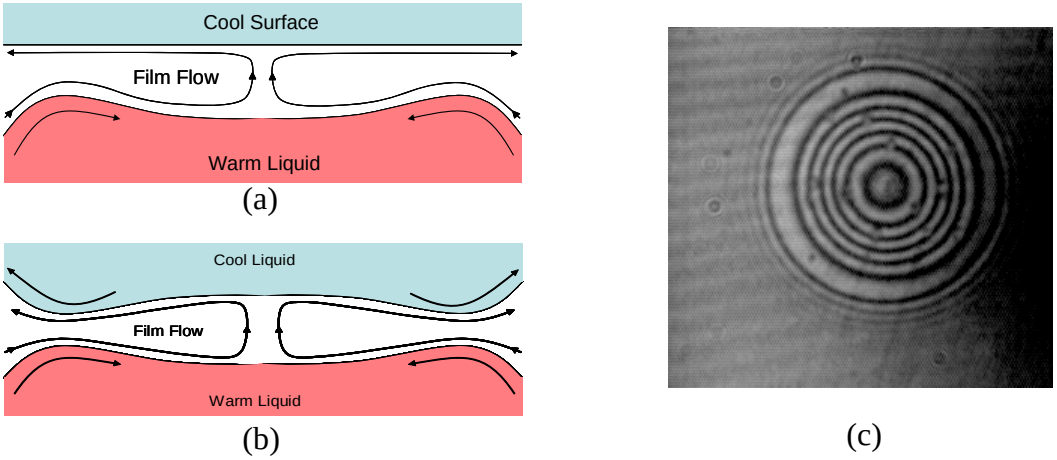


Figure 2. Drawings of thermocapillary convection within drops of permanent (a) nonwetting and; (b) noncoalescence. The drawings are not-to-scale. (c) is an interferometric visualization of the contact region of a nonwetting system, where each contour represents regions of equal film thickness. High pressure at the symmetry axis creates a dimple on the liquid surface.

The lubricating film exerts sufficient pressure to keep two surfaces apart. The resulting distance between the surfaces is typically on the order of a few μm as measured by Dell'Aversana, *et al.* (1997). This is a few orders of magnitude thicker than the length scale at which the van der Waals force causes the surfaces to be attracted to each other.

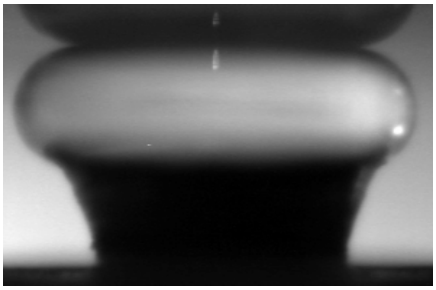


Figure 3. A high compression introduced on a nonwetting droplet.

Due to the over pressure from the lubricating film, the droplet can be squeezed well into a solid surface without wetting it. With a sufficient compression, the interface of the droplet becomes distorted from a spherical to an oval shape, as seen in Figure 3. Associated with such high compression is an increase in capillary pressure, which increases with the curvature of the interface. At the same time, the lubricating film's

pressure also increases in order to balance this effect. The ability of the lubricating film pressure to adjust itself to the changes in capillary pressure confirms that a nonwetting system is capable of supporting a load. For example, Dell'Aversana & Neitzel (2004) experimentally measured the load of $O(100\ \mu N)$ on a droplet pinned to a 3 *mm* disk pedestal, which is slightly higher than its own weight (*e.g.*, the weight is roughly 60 μN for a half-hemispherical droplet of silicone oil).

1.2. Application and Failures

1.2.1. Nonwetting Applications

Several engineering applications of permanent nonwetting (and noncoalescence) system have been proposed (and demonstrated) in the past. The nonwetting and noncoalescing systems are attractive for a centering device in low-gravity environment, load-bearing systems, and possibly for studying interactive forces between liquids (Dell'Aversana & Neitzel (1998)) due to low internal friction, non-contacting nature of the surfaces, and their load-carrying capabilities. A load-bearing system has been demonstrated by Dell'Aversana; by supporting a magnet on a series of non-coalescing drops he created a compass as shown in Figure 4. The magnet can rotate on the bath surface very smoothly due to the non-contact nature of the system.

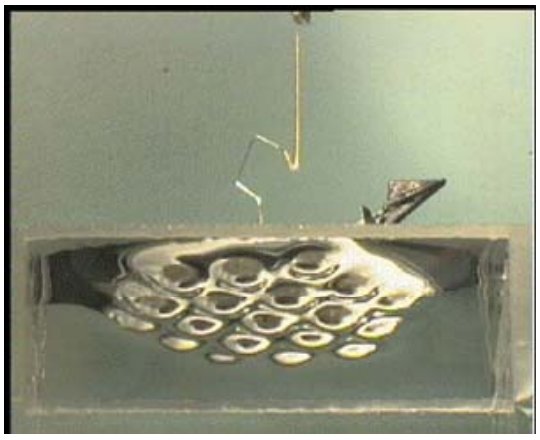


Figure 4. Dell'Aversana's compass. The magnet is supported by a series of noncoalescing droplets. The image shows bulged free-surface corresponding to the location of droplets, visualized by the presence of the thin film of air.

In order to optimize such load-bearing systems, knowledge of the loading-limit will help to sort out a range of safe operation for a nonwetting system. It is known that the system does fail if certain threshold criteria are exceeded, even though the lubricating film is provided. Therefore, a portion of the present research is aimed at quantifying thresholds of nonwetting-system failure associated with an application of a mechanical loading on a droplet.

1.2.2. Nonwetting System Failure

Past studies on the subject of nonwetting have indicated several different mechanisms of failure, which are attributed to instabilities of the film flow and the liquid-gas interface. For example, the interface of a droplet can become unstable due to the presence of electric charges on a glass plate against which the droplet is compressed (Neitzel, et al. (2000), Figure 5). In addition, application of an electric potential of $O(100\ V)$ across a droplet and the solid surface causes the surface of the droplet to be "pinched off" at the center of the droplet, leading to a wetting (Dell'Aversana & Neitzel (2004), Figure 6). This is similar to Taylor-cone instability (Taylor (1964)) observed on electrically-conducting liquids. Silicone oil, typically used in nonwetting experiments, is leaky-dielectric (poor-conducting) (Basaran (2002)), surface of which also may be influenced by an electric field.

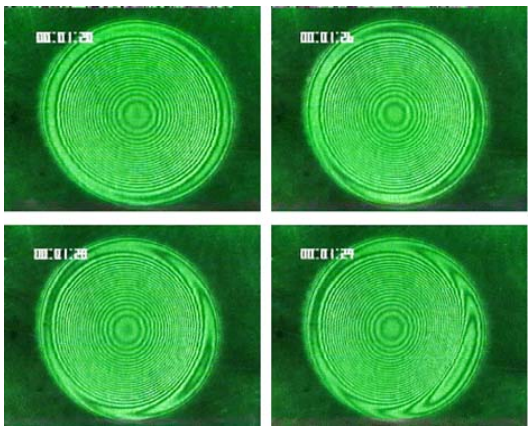


Figure 5. Interferometric observation of the interface shape, which is disturbed by the presence of static charges on the glass surface. Image source: P. Dell'Aversana.

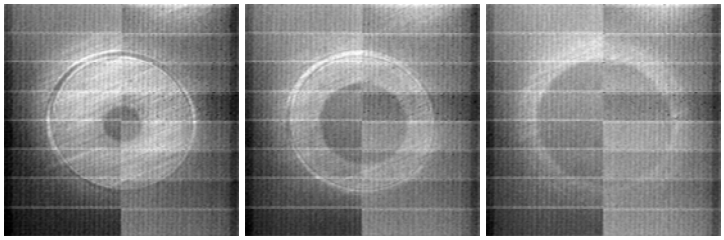


Figure 6. High speed sequence of a wetting process initiated by the electrical potential. The wetting starts at the center of the droplet where charges accumulate resulting in a Taylor-cone structure on the surface. Image source: P. Dell'Aversana.

Other types of failures are triggered purely by mechanical means. For example, film and pinning failures, discussed in the present study, are associated with an application of a high compressive loading on a droplet.

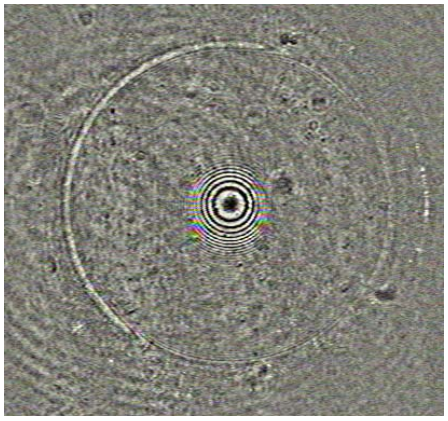
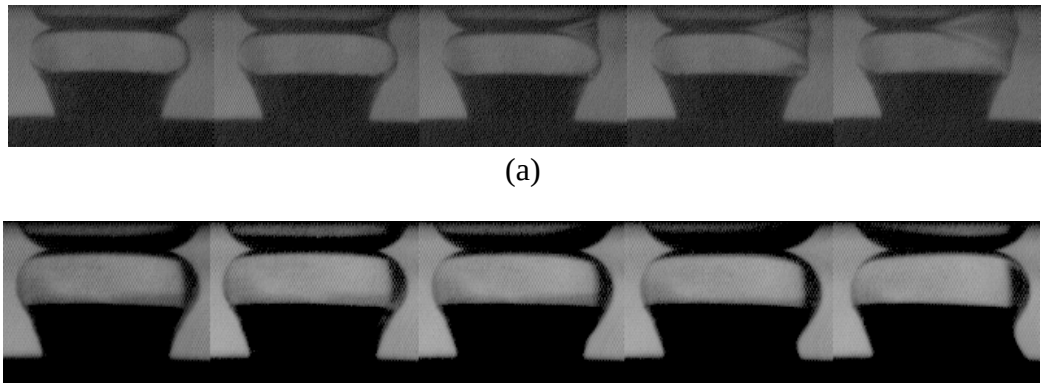


Figure 7. Interferometric image of a tilted interface. The interference pattern shows non-uniform film thickness just prior to film failure. The height variation is ~ 1.2 μm, determined from the changes in fringe pattern (white to black to white, *etc*.) on the periphery of the dimpled surface.

Film failure occurs when the maximum allowable loading is surpassed, resulting in the thinning of the film and the growth of instability. At an early stage of loading, the lubricating film becomes thinner uniformly around the perimeter of the dimple. As the loading increases, the film thickness becomes uneven while the system may remain stable at this point. The nonuniform film thickness can be seen from interferometric observations, such as the one presented in Figure 7, which shows height variation of roughly ~1.2 μm half-way around the perimeter of the circular pattern. With a further compression from this point, surpassing some critical threshold, the growth of instability

is initiated at a location on the periphery of the dimple, and leads to a wetting event. Multiple observations of film failure, such the high-speed sequence in Figure 8(a), confirm that film failure is initiated at a location on the periphery of the dimple, where the film thickness is thinnest, and propagates across the contact region. These observations show that the droplet is unstable to an azimuthal perturbation with $m = 1$ mode, where m is the azimuthal wavenumber.



(a)

(b)

Figure 8. High speed sequence of a) film; and b) pinning failure. Time intervals between the images are 1/2000 and 1/200 seconds, respectively.

In other instances, the flow of the lubricating film may become more stable, for example by increasing temperature differences between respective surfaces, allowing the droplet to be squeezed well against the glass surface. In this circumstance, a highly deformed droplet fails at its pinning boundary, somewhere on the disk support, and spilling some portion of its volume from the edge as seen in Figure 8(b). This is called pinning failure.

The present studies will be focused on quantifying film- and pinning-failures triggered during an application of mechanical loading, under static and dynamic environments. The goal is to characterize these failures, which can be used as a guide line in designing a load-carrying system using permanent nonwetting.

1.3. Droplet Levitation and Translation for "Lab-On-a-Chip"

1.3.1. Ideas and Concepts

In addition to quantifying the failure-thresholds of a nonwetting system, the present research explores the concept of levitation, where a droplet is levitated and steered above a solid surface by manipulating the mechanisms of permanent nonwetting. This idea follows from the demonstration of droplet levitation by Dell'Aversana in Figure 9, with a silicone-oil droplet floating over a bath filled with the same liquid. Here, the droplet is prevented from coalescing with the bath by receiving thermal energy from a hot plate placed above it, maintaining thermocapillary convection. A levitated droplet such as shown in this picture needs to be placed on an under-filled bath to prevent it from rolling off to a side due to gravitational pull.

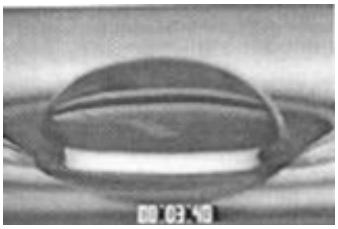


Figure 9. Demonstration of droplet levitation. The silicone-oil droplet is afloat on top of the bath of same liquid.

The present research will attempt to levitate a droplet above a solid substrate. In addition the positions of the droplet will be controlled. This type of droplet handling has promising application in a Lab-On-a-Chip (LOC) environment, where traditional laboratory testing, such as pre-treatment, detection, reaction, are integrated on a very small test surface, increasing efficiency due to the reduced time and cost of the analysis by requiring small sample sizes. In addition, LOC is capable of performing these tasks in parallel. By exploiting today's fast processors and the shorter reaction times obtained from the high volume-to-area ratio of chemical specimens, testing can be faster than traditional methods, yielding a high throughput (Weigl, *et al.* (2003), Jain (2003)).

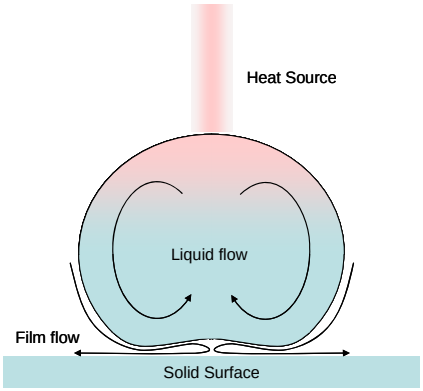


Figure 10. Conceptual sketch of a droplet levitated above a solid surface. The mechanism is the same as nonwetting drop, except the energy input is derived from an isolated energy source, such as a CO_2 laser.

Figure 10 shows the basic conceptual drawing of a levitated drop. The droplet receives heat from an isolated energy source and is cooled at the bottom by the solid plate, generating thermocapillary convection. At least some portion of the incident thermal energy needs to be absorbed by the liquid in order to raise the temperature and introduce convection. A CO_2 laser ($\lambda = 10.6\ \mu m$) has been very effective for achieving the task.

The use of a levitated droplet in LOC has certain advantages over conventional systems where pumps are typically used to push liquids through tiny ducts and channels, such as shown in Figure 11. One of the concerns associated with the liquid delivery used in a conventional LOC system is the possibility of contamination that may arise from moving a liquid across a surface that has already been traversed by another specimen, which may have left traces in the form of a very thin film. On the other hand, a levitated droplet is not in a contact with any surfaces; it minimizes or even eliminates contamination. This feature is especially attractive when a delicate specimen, such as a DNA sample, is to be handled, as it demands minimal contamination in order to carry out an accurate analysis.

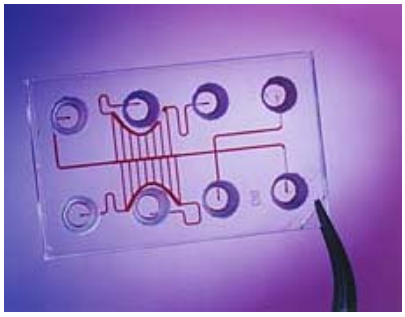


Figure 11. Conventional test surface for LOC systems. Pumping mechanisms are generally required to push liquid through ducts and channels with characteristic dimensions of *O*(10–100 μm). The image is obtained from Agilent Technologies' website.

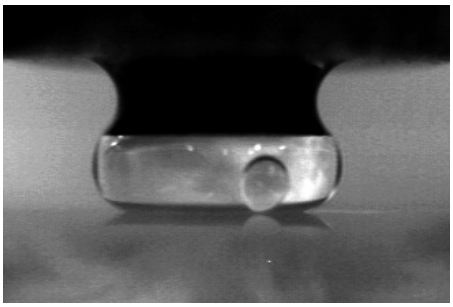


Figure 12. Aqueous solution (dyed for a visualization purpose) engulfed within a nonwetting droplet of silicone-oil. Since these liquids do not mix, contamination on aqueous sample is virtually eliminated.

Contamination may virtually be eliminated by encapsulating a specimen within a protective layer of an immiscible liquid. For example, an aqueous solution commonly used as a carrier for DNA strands can be engulfed completely within inert oil, such as silicone oil, without mixing. The concept of encapsulation is shown in Figure 12, where a dyed water-droplet is engulfed within the layer of a nonwetting silicone-oil droplet. The inner aqueous sample is not exposed to the environment, assuring that it remains free from contaminants from the environment. By exploiting this fact, an aqueous droplet is to be encapsulated within a levitating droplet (of silicone oil) while it is being delivered on a test surface.

In addition, the delivery of a levitated droplet allows versatility and flexibility in the LOC's test configurations. Because there's no predetermined path for the liquid, a levitated droplet is free to be positioned anywhere on the test surface depending on the needs and requirements of an analysis. As a result, testing can be carried out at any

location on a surface; it is not restricted by the locations of reaction chambers and channels.

Furthermore, the delivery of a levitated droplet does not require pumps that are typically used by a conventional system to push liquids through ducts. This eliminates a demanding task of generating a very large pressure difference to overcome the viscous stress and contact-angle hysteresis. For example, the Hagen-Poiseuille law states that the pressure gradient increases as $O(l^{-4})$ (where l is the length scale of the cross-section of a duct) while maintaining a required flow rate.

These inherent resistances make the delivery processes rather slow in the conventional systems. On the other hand, a levitated droplet is exposed to a minimal resistance. When placed statically above a solid substrate (as shown in Figure 10), a levitated droplet is exposed to a vanishingly small viscous resistance from the surrounding gas due to the axisymmetric nature of the system. While it is in a translation, the resistance should stay very small, allowing the droplet to achieve higher speed, moving from one location to the next relatively quickly. A fast translational time is advantageous for LOC applications where fast processing speed is desired for analyzing large number of samples.

In order to move a levitated droplet, symmetry in thermocapillary convection must be broken. This is done by shifting the location of a heat spot towards one side of the droplet, resulting in a net flux of surrounding air from the other side of the droplet (Figure 13). Due to an imbalance of the momentum flux, a propulsive force is generated towards the direction of the heat source. A steerable mirror or arrays of digitally addressable mirrors (*e.g.*, DLP™ by Texas Instruments) can be used to modulate intensity and control the positions of the heat spot in a desired fashion. For example, Garnier, *et al.* (2003) used digitally-addressable mirrors to create thermal perturbations on a thin liquid film, suppressing the fingering instability of a film during the spreading process.

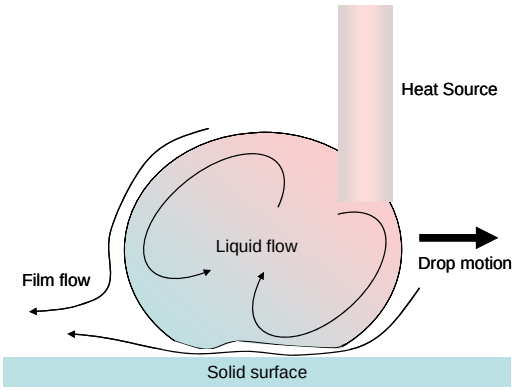


Figure 13. Conceptual sketch of a migrating, levitated droplet. The symmetry in thermocapillary convection is broken due to an offset of the heat spot, leading to jetting of the surrounding gas.

The present research is aimed at demonstrating the controlled delivery of a levitated droplet. Simple thought experiments can be used to argue some requirements for the prospective speeds of the heat source and the droplet during the delivery process. For instance, the migration speed of a levitated droplet must remain below the induced speed of thermocapillary convection in order to prevent wetting; as these speeds approach one another, the effect of lubricating film vanishes. In another situation, levitation ceases to exist if the heat source is moved faster than the droplet moves, whereby the droplet achieves a thermal equilibrium with the solid surface without the heat input. In addition, the heat source must be carefully brought to a halt since the inertial effect can cause the translating droplet to overshoot the source. These issues may be of importance for achieving successful control of a levitated droplet.

The next section will discuss scaling arguments for estimating the characteristic size and the acceleration of a levitated droplet that may be achieved in a simple experimental setup. These preliminary calculations are used to conclude that levitation of a droplet and manipulation of its position on a surface are feasible tasks.

1.3.2. Preliminary Calculations

To argue whether the delivery of a levitated droplet is ever feasible, the size and acceleration (at time = 0) of a levitated droplet were estimated by employing physical arguments and existing experimental data. In order to levitate a droplet, its weight, W_d, must be supported by the force generated by the lubricating film, F_{lub},

$$F_{\text{lub}} = W_d \sim \rho_l g R_d^3 \qquad (2)$$

where ρ_l is the density of the droplet, g is the gravitational-acceleration constant, and R_d is a nominal radius of an undeformed, levitated droplet. Upon rearranging, the size of a droplet that can be levitated for a given lubrication force is

$$R_d \sim \left(\frac{F_{\text{lub}}}{\rho_l g} \right)^{1/3}. \qquad (3)$$

The estimate of the lubricating force is $F_{\text{lub}} = O(100\ \mu N)$ based on the load measurement of a nonwetting system reported in Dell'Aversana & Neitzel (2004), where they measured $O(100\ \mu N)$ from a 5 *cSt* silicone-oil droplet on a 3 *mm* disk. By using $\rho_l = O(1000\ kg/m^3)$ and $g = O(10\ m/s^2)$, the radius of a droplet that can be levitated is estimated to be $R_d = O(1\ mm)$. It should be noted that this analysis is a first-order estimate: The loading characteristics should be different between the pinned droplet studied by Dell'Aversana & Neitzel and the levitated droplet due to the difference in the boundary conditions.

The acceleration of the droplet is estimated from a control-volume analysis. This control volume, viewed from the top of a droplet, is shown Figure 14. The motion of the droplet is confined to 1-D translation along the *x*-direction. The heat source is incident on the right-hand side of the droplet, inducing thermocapillary convection with the free-surface speed U_s. The system of concern is assumed to be stationary due to the application of the fictitious force *F* at the "leading" edge of the droplet, holding it in this position. According to mass conservation, there is a finite mass flux at the inlet region 1 (with a fluid velocity, U_i) and at the control surface on the sides. By extending surface 1

sufficiently far from the droplet, the mass flux there can be considered to be negligibly small ($U_i \sim 0$).

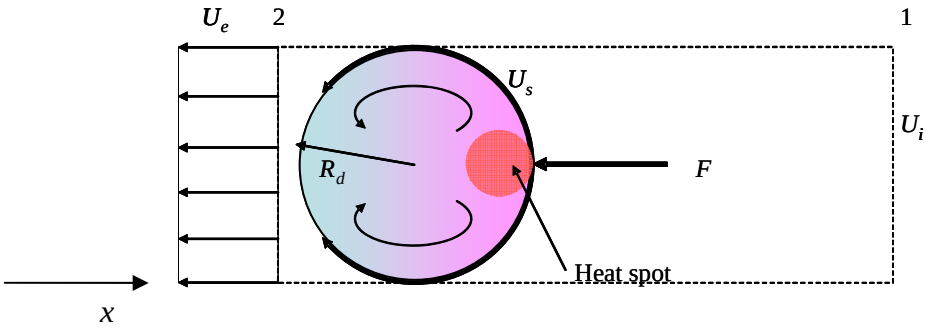


Figure 14. Control volume, viewed from top, for estimating the acceleration on a levitated droplet. The droplet is held in place by an application of virtual force.

The flow profile of the fluid exiting from surface 2 is assumed uniform and round, having the same radius as the droplet. The magnitude of exiting velocity is U_e. By placing the control surface 2 very near the droplet, the velocities of the free surface and the jetted gas are assumed to be of the same order, $U_e \sim U_s$. Under these assumptions, the steady-state momentum equation leads to

$$\rho_g U_s^2 \pi R_d^2 = F\,, \tag{4}$$

where ρ_g is the density of gas. The acceleration is determined from Newton's 2nd Law for a constant mass, $F = ma$, and by releasing the droplet from the restraining force at time $t = 0$. The result yields

$$\rho_l \frac{4}{3} \pi R_d^3 a = \rho_g U_s^2 \pi R_d^2\,, \tag{5}$$

where a is the acceleration of the droplet. Upon rearranging expressions, a is expressed as

$$a = \frac{3\rho_g U_s^2}{4\rho_l R_d} \tag{6}$$

This expression states that the acceleration is proportional to the ratio of the densities between the surrounding gas and the droplet, to the square of the surface velocity, and is inversely proportional to the radius of the droplet.

To complete the analysis, the surface velocity U_s is estimated from the thermocapillary-velocity scale,

$$U_s \sim \frac{\gamma \Delta T}{\mu_l} \qquad (7)$$

which is derived from a tangential stress balance at the interface. In equation (7), ΔT can be considered as the temperature difference between "hot" and "cold" regions of the droplet, and μ_l is the viscosity of the droplet. Nominal values for μ_l, γ, and ΔT are $O\left(0.001\, kg/m/s\right)$, $O\left(10^{-5}\ N/m/K\right)$, and $O\left(10\ K\right)$, respectively, which are representative values of a permanent nonwetting system using silicone oil with the density $\rho_l = O\left(1000\ kg/m^3\right)$. The density of the jetting air is $\rho_g = O\left(1\ kg/m^3\right)$. Equations (7) and (6) yield a surface velocity of O(10 *cm/s*) and an acceleration of a liquid droplet of O(10 *mm/s*^{2}), respectively. The results from this section suggest that a *mm*-scale droplet can be levitated and steered with a considerable acceleration by manipulating the mechanisms of nonwetting.

1.4. Chapter Summary

There are several goals to this research, the results of which will promote the use of nonwetting drops in engineering applications. First, the criteria for failure loading are determined experimentally for the permanent nonwetting system. The analysis will be useful for designing a nonwetting droplet as a load-bearing device, as it is important to know how much a system withstands the mechanical load and characterization of failures. A series of experiments has been carried out to determine the maximum allowable loading on the droplet. Next, the technique, which enable the dynamics of the free surface be reconstructed and be analyzed, will be discussed. The technique will be useful for characterizing dynamic responses of a droplet to external forcing. Finally, the droplet

levitation and the above-described delivery concept will be demonstrated experimentally. The study will provide a new delivery mechanism to be realized in LOC applications and will provide future investigators the basis upon which to improve these concepts.

2. Relevant Research

2.1. Permanent Nonwetting and Noncoalescence

The present research is aimed at the understanding of nonwetting-system failure, and at promoting the system for engineering applications. As described before, the mechanism of permanent nonwetting depends on the continuous supply of the intervening film between the mating bodies. A thermocapillary-driven nonwetting system is self-lubricating since it provides its own lubricating film as long as sufficient temperature difference is maintained between respective surfaces of concern.

On the other side of the spectrum of permanent noncoalescence and nonwetting, the temporary nature of these phenomena is a well-studied topic. Because of its importance in diverse engineering applications such as design of efficient heat-transfer systems, combustion processes, rain formation, *etc*., the research in the field of temporary noncoalescence has expanded since the early scientific investigations of Rayleigh (1879) and Reynolds (1881). The studies of temporary behaviors of noncoalescence and nonwetting are diverse, and will not be discussed in detail in this thesis. The readers are advised to consult Neitzel & Dell'Aversana (2002) for an overview of the permanent and temporary natures of the phenomena.

The first observation of permanent noncoalescence dates to a Space Lab mission studying thermocapillary convection within liquid bridges. Napolitano, *et al.* (1986) reported that a broken bridge had difficulty in reconnecting while a temperature difference was imposed between the two rod ends. The mechanism of the seemingly counterintuitive result relies in the provision of a lubricating film at the region where two surfaces apparently touch each other, as explained by Dell'Aversana, *et al.* (1995),and Dell'Aversana, *et al.* (1996)

From the knowledge that coalescence of two droplets can be hindered using temperature differences, Dell'Aversana, *et al.* (1996) conducted systematic studies on permanent noncoalescing droplets. The authors demonstrated that two droplets in apparent contact could be kept separated for as long as hours, by imposing a temperature difference between them; the droplets would coalesce only when the temperature difference was reduced below some threshold. The investigators attributed the relative

tangential motion between the surfaces as the mechanism, which helps to entrain the surrounding gas into the contact region. To support this idea the authors demonstrated permanent noncoalescence under isothermal conditions. In this scheme, a droplet is squeezed against a rotating bath of the same liquid, which drags the surrounding gas into the interstitial space. Figure 15 is taken from their isothermal noncoalescence experiment, in which a wake is formed on the bath surface behind the compressed droplet. In addition, Dell'Aversana, *et al.* (1996) performed a molecular-dynamics simulation of isothermal noncoalescence. From the simulation, they were able to show that a sheared motion prevents the droplet from stretching towards the bulk phase by inducing rotation on the droplet.

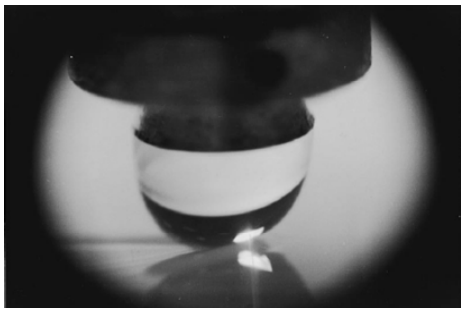


Figure 15. Isothermal noncoalescence demonstrated by Dell'Aversana, *et al.* (1996).

Employing interferometry, Dell'Aversana, *et al.* (1997) determined the shape and the thickness of the interface of a permanent nonwetting system. Their experiments revealed an axisymmetric dimple on the surface of a droplet, at the center of the contact region. The deformation is largest at the center of the drop, decreasing towards the edge of the dimple. The measurement of the film thickness showed the variation within the contact region, with ~ 10 μm at the center of the droplet, where the pressure is highest, to ~ 5 μm at the periphery of the dimpled surface. The corresponding distance between the surfaces is sufficiently kept apart, that intermolecular forces, such as van der Waals forces that act in the range $O(1\ nm)$, cannot come into play to attract the surfaces together. The authors also have studied the variations of interstitial shapes at different stages of squeezing applied on a droplet at a fixed temperature difference. The squeezing results in widening of the dimple while the film at the center thickens and thins at the periphery of

the dimple (Figure 16). The authors also commented on an oscillatory behavior observed for a large noncoalescing droplet squeezed against a liquid bath. This behavior is very similar to thermocapillarity instability of a liquid bridge used for studying float-zone crystal growth (Sumner & Neitzel (2001)).

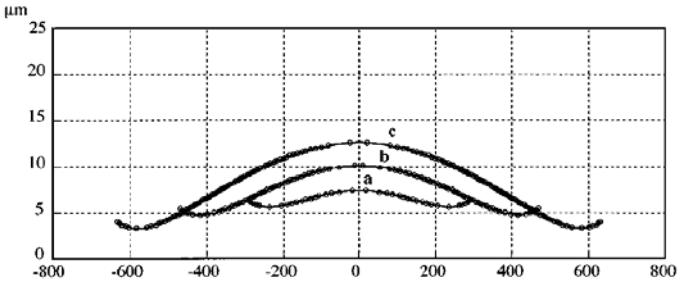


Figure 16. Shapes of an interface at different stages of compression applied on a nonwetting droplet. The captions a, b, and c correspond to 100, 200, and 300 μm. Source: Dell'Aversana, *et al*. (1997).

Because the film of air lubricates the interface in permanent nonwetting and noncoalescence, the ambient pressure affects their performances. Dell'Aversana & Neitzel (2004) studied effects of the ambient pressure on noncoalescing systems by placing the droplets in a pressure chamber. The authors showed that the coalescence pressure (at which coalescence occurs) decreases with increasing temperature difference between the droplets. The ability of the droplets to remain apart in the low-pressure atmosphere is due to the nature of convection, which drives the surrounding gas more vigorously at an elevated temperature difference. In addition, the authors used Surface Evolver (Brakke (2005)) to compute loads on a *static* droplet pressed against a surface. A remarkable agreement was found between the load measured from their experiments and the one computed from Surface Evolver. The result suggests that the load on a nonwetting droplet can be computed from an increase in capillary pressure associated with the deformation experienced by the droplet. Thermocapillary convection provides the means to balance the increased capillary pressure within the contact region.

In addition to these experiments and the molecular-dynamics simulation, several authors have attempted to tackle the continuum modeling of isothermal and thermocapillary nonwetting and noncoalescence. The following models provide quantitative details of the physics and parameters that affect the lubricating mechanism.

The first continuum modeling of a permanent noncoalescing system was carried out by Monti & Savino (1996). Although their simulation agreed qualitatively with their experimental observations, the model incorporated *ad hoc* arguments. For example, the shape of the droplet was computed *initially* using the Young-Laplace equation, instead of using hydrodynamic pressure balance. In addition, a flat channel was assumed for the air flowing inside the contact region, which also does not agree with the actual, dimpled interface as seen in Figure 16. Savino & Monti (1997) discussed details of their numerical computations in their earlier studies, including iterative procedures that can be used to correct for the variations in the interface profile, which arises due to the pressure distribution inside of the contact region. The authors concluded that the interstitial profile is not significantly affected by the pressure distribution, and thus the first-order (flat interface) solution is sufficient for the purpose of comparing the results from simulation with their experimental data. For an instance, the computed film thicknesses agreed with their experimental measurement over a wide range of temperature differences.

Monti, *et al.* (1998) modeled a permanent nonwetting system employing the similar treatment used in permanent noncoalescence. Their computational results agreed qualitatively with the experimental measurement of film thickness, showing the thinning of the lubricating film with decreasing temperature difference between the surfaces.

Sumner, *et al.* (2003) carried out a lubrication analysis of a 2-D nonwetting system with a small aspect ratio (height/radius). Using the perturbation method, the leading- and higher-order perturbation equations were solved numerically. The authors found that leading-order solution failed to capture the dimple formation on the free surface, but succeeded with the higher-order corrections. They concluded that the viscous and inertial effects from the surrounding air were important in the dimple formation.

Smith & Neitzel (2006) tackled a 2-D isothermal-nonwetting problem, using a multiple-scaling argument, and resolving the computational difficulty associated with the nonwetting problem. Their approach was to split up the problem into two domains, with the inner and outer flows having length scales of the film thickness ($\sim \mu m$) and of the

droplet (~ *mm*), respectively. In order to reduce the computational effort, a lubrication approximation was used for the gas flow inside the contact region, coupling to the outer problem solved by the commercial finite-element code, Femlab (in addition to external code written to keep track of deforming surface). Although their results showed unstable solutions for some cases of droplet squeezing, intriguing features were detected in some situations. These features include the existence of counter rotating vortices and the drop deformation opposing the bulk flow of the gas. The two dimensional nature of the problem, however, imposes restrictions not found in experiments, such as the fact that the gas cannot flow *around* the droplet. The blockage of the gas is not present in a 3-D, axisymmetric droplet.

Kuo, *et al.* (2005) and Chen, *et al.* (2005) used the commercial finite-element package FIDAP to solve the 2-D isothermal- and thermocapillary-nonwetting problems, respectively. The numerical simulation for the isothermal nonwetting showed counter rotating vortices, as was reported by Smith & Netizel (2006), and the agreements were remarkable between these simulations. The simulations were carried out using properties of silicone oil and water, and the result lead the authors to conclude that water is also capable of achieving isothermal and thermocapillary nonwetting. This conclusion is fascinating, for a successful permanent nonwetting with water droplets has not been reported experimentally to-date. Their argument states that the Weber number

$$We = \frac{\rho_l U_w^2 R_0}{\sigma_0}, \tag{8}$$

with U_w being the speed of the moving wall and R_0 being the radius of the disk support, and the capillary number

$$Ca = \frac{\gamma \Delta T}{\sigma_0} \tag{9}$$

of a water droplet are smaller than those associated with a silicone-oil droplet. As a result, they concluded that water was a bad choice for inducing permanent nonwetting.

The investigations mentioned above have contributed toward the basic understanding of permanent nonwetting and noncoalescing systems, from the concept of

lubrication of the air film, its thickness, and its characteristics under various temperature differences and the pressure. These studies have shown that the underlying physics of permanent nonwetting/noncoalescence can be exploited for a development of engineering applications, such as load-bearings and near-frictionless droplet translation.

2.2. Lab-on-a-Chip and Liquid Handling

Lab-on-a-chip (LOC) is the generic name given to a class of devices designed to carry out conventional laboratory testing on a small surface. In the past decade, the fluid-mechanics research community has paid close attention to LOC applications, investigating various methods for handling small volumes of liquid in the very demanding environment posed by viscosity- and surface-tension-dominated environments encountered in the LOC. Today, the majority of LOC devices on the market rely on scaled-down delivery method by using miniaturized pipes and ducts (Stone, *et al.* (2004)).

LOC environments pose difficulties in providing accurate control over a liquid flow when mechanical pumps (such as peristaltic and piston-syringe pumps) are employed. In addition, design and fabrication of the mechanical pumps can become more complicated as the length scale of the pipes becomes smaller and as the applications become more complex with more fluid networks (Schwartz, *et al.* (2004)). In order to eliminate these difficulties associated with the mechanical pumps, different authors have resorted to the use of electrical potential to drive streams of liquid and discrete droplets (Bousse, *et al.* (2000), Jones (2001)). On the other hand, the use of electrical potential has several inherent problems associated with the application of high electrical potential of $O(100\ V)$, which may result in an unwanted electrochemical reactions of the chemical species, in addition to high Ohmic heat-generation that can damage the sample specimen (Whitesides & Stroock (2001)).

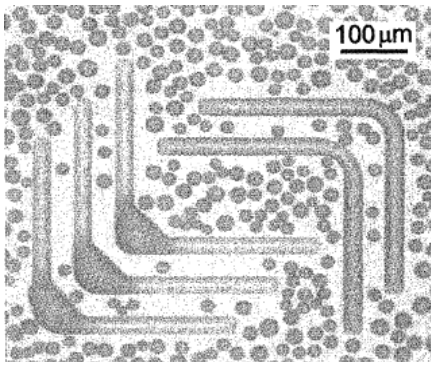


Figure 17. Morphological instability of liquid on an open, curved channel. Instability creates bulges at the corners of the channel, reducing gaps between the liquids. These can be used to mix streams of liquid. Source: Gau, *et al.* (1999).

Other methods are available, avoiding the use of mechanical pump or the application of high voltages completely. For example, the method from Yuan & Prosperetti (1999) generates a net motion within a liquid stream through successive generations and collapsing of bubbles by manipulating heaters embedded underneath a channel. The method described by Lam, *et al.* (2002) exploits capillary wicking of the liquid that is confined between two surfaces separated by a very short distance. The idea presented by Gau, *et al.* (1999) exploits morphological instability and associated "bulge" generated on the free-surface of a droplet on a channel in order to connect two different streams of samples and mix them together (Figure 17).

The system presented in Gallerdo, *et al.* (1999) moves particles suspended in a liquid by controlling the surface tension of the pool through an electrochemical method. In this method, "on" and "off" states of surface-active species are switched by applying a very low voltage supply of $O(1\ V)$. The technique of Darhuber, *et al.* (2003) drives a stream of liquid by imposing a temperature gradient along a channel, actuating the thermocapillarity effect on the free surface of liquid.

The liquid-delivery schemes mentioned above involve motions of a "continuous" stream of liquid in a duct or on an open channel. On the other hand, the use of continuous streams for the delivery of specimens is sometimes not desired, due to the increasing complexity of pumping mechanism, dead volumes that are wasted, and difficulty in manipulating branched channels due to continuity (Schwartz, *et al.* (2004)).

In fact, droplet-based delivery is often desired for various LOC applications, because it enhances certain types of chemical reactions owing to the larger surface-to-volume ratio. In addition, the use of droplets in an open channel reduces experimental noises since there is no container wall which lowers the sensitivity of measurement (Miller & Synovec (2000)). The following paragraphs list some delivery concepts that have succeeded in driving discrete droplets in LOC environments.

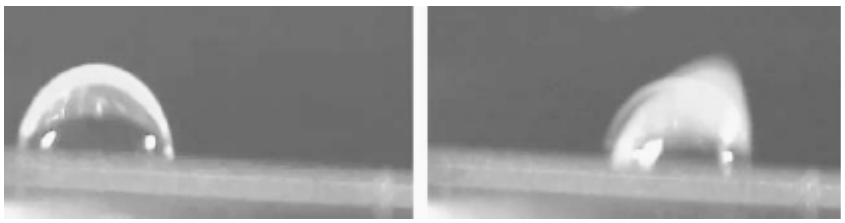


Figure 18. Droplet translation induced by the surface acoustic wave. Image source: Wixforth, *et al.* (2004).

The method described in Wixforth, *et al.* (2004) exploits the surface acoustic wave, generated on a piezo-electric material to move a droplet on a test array. The surface acoustic waves are similar to earth-quakes; the energy input from the vibration transfers energy into the fluid, inducing a translation of a viscous droplet (Figure 18).

As an alternative to this type of "mechanical" actuation, many other investigators manipulate the surface-tension force to push the droplet in a certain direction. For example, the method described in Chaudhury & Whitesides (1992) moves a droplet along the surface-energy gradient, generating nonequilibrium contact angles between the front and rear sides of the droplet. The "thermocapillary pumping" described by Sammarco & Burns (1999) exploits the difference in the capillary pressure across a droplet generated by localized heating. In this method, heating is applied at the front (rear) end of a hydrophobic (hydrophilic) droplet confined between two plates, resulting in pressure difference across the droplet and generating the propulsive force. Darhuber, *et al.* (2003) demonstrated "thermocapillary migration" of a droplet on an open channel, by differentially heating the droplet using individually-addressable heaters placed underneath a channel (Figure 19). Theoretical treatments of the thermocapillary migration has been investigated by Ford & Nadim (1994) and Smith, *et al.* (2003). The electrowetting method of Cho, *et al.* (2003) moves a droplet by changing the wetting

characteristics of a droplet by an application of electric potential. All of these demonstrations have proven their utility as the delivery scheme to move a droplet *on* a solid surface.

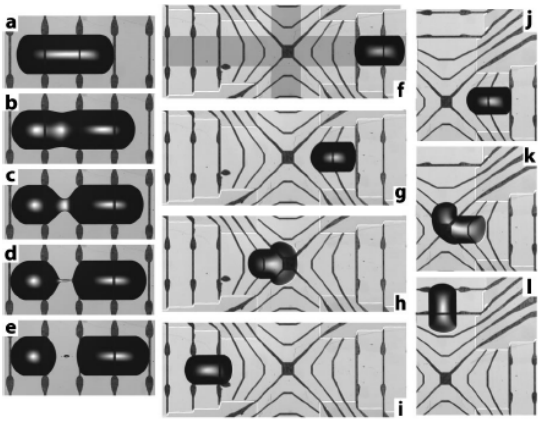


Figure 19. Thermocapillary migration of droplets on a flat surface. (a)-(e) shows a sequence of drop-splitting. (f)-(l) shows translations of the droplet. Source: Darhuber, *et al.* (2003).

One goal of this research is the successful demonstration of the concept of droplet levitation and its controlled handling, both of which are made possible by exploiting the basic mechanisms of a permanent nonwetting system. The study aims at showing the applicability of these concepts to LOC environment where miniaturized droplet-based testing is carried out. The concept of levitation relies on the lubricating film of air for supporting the weight of a small droplet. The droplet shall be moved by manipulating thermocapillary convection via shifting the heat spot on the droplet. The advantages associated with the use of levitated droplet in a LOC application is its "containerless" configuration, where the droplet is not in a direct contact with any surfaces, eliminating contaminations that degrade quality of analysis.

Various levitation schemes, different from the one pursued in this research, have been studied in the past and have shown their potential in applications. For example, acoustic levitation was used by Omrane, *et al.* (2004) for studying concentrations of species inside a floating droplet. Chung & Trinh (1998) used an electrostatic method to levitate a droplet and grow a crystal inside. Lyuksyutov, *et al.* (2004) showed magnetic levitation and transportation of a diamagnetic droplet for microfluidics applications. Linke, *et al.* (2006)'s method exploits Leidenfrost effect to levitate a droplet and moves it

along a surface with saw-tooth patterns, which create asymmetry in the vapor pressure underneath the droplet. The mechanisms of these successful schemes used in levitation are different from the one proposed in this work. Therefore, further details of these schemes will not be discussed.

The focus of the present research is a levitation scheme that exploits the lubricating film of air. Although, there have been reports of droplet levitation that owes to the presence of the film flowing underneath the droplet, they tend to be either nonpermanent or can't be manipulated easily. If the proposed technique from this research is proven plausible, then the system may find many engineering applications and thus warrants further detailed investigations in the future.

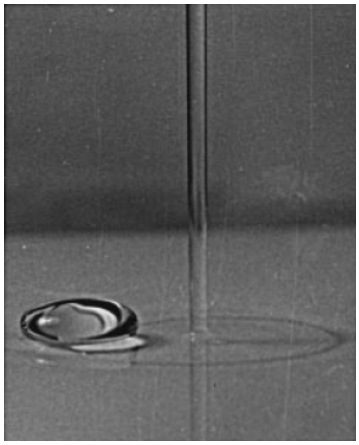


Figure 20. Water droplet levitated over a radially flowing liquid film. The droplet stays in the region of hydraulic jump. The volume of the droplet is ~0.75 *ml*. Source: Screenivas, et al. (1999).

In order to appreciate the levitation scheme of the present research, several other examples of levitations, which are also enabled by the presence of a thin lubricating film, will be discussed. A study by Sreenivas, *et al.* (1999) reported that droplets of various sizes could be supported above a flow of a rapidly moving, radially flowing liquid film (Figure 20). The mechanism here is the same as that of isothermal noncoalescence from Dell'Aversana, *et al.* (1996). Such levitated droplet is reported to stay at the location of the hydraulic-jump. The investigators also observed that the droplet can be set into motion in the azimuthal direction, along the ridge of the hydraulic jump, by changing the flow rate of the liquid film.

A different levitation scheme, studied by Couder, *et al.* (2005), imposes a vertical vibration on the liquid bath in order to supply the film of air at the interface between the droplet and the bath. The study has shown that, if the vertical acceleration of the bath exceeds a threshold criterion, the droplet bounces from the bath's interface indefinitely without coalescing. In addition, the authors have noted a different noncoalescence regime where a droplet simply floats on the bath surface after the vibration amplitude of the bath has been reduced. The life time of such noncoalescing droplet is related to the rate of drainage of the film between the droplet and the bath.

Other schemes exploit modification of the surface-tension force on the free surface of a droplet instead to provide the lubrication. For example, Amarouchene, *et al.* (2001) showed that the residence time of a noncoalescing water droplet, resting above a water bath, can be prolonged by releasing a surfactant on the droplet. In this scenario, the presence of the surfactant, and hence the solutocapillary effect, resists the free-surface motion from moving outward from the region of mating surfaces, thus retarding the film-drainage process.

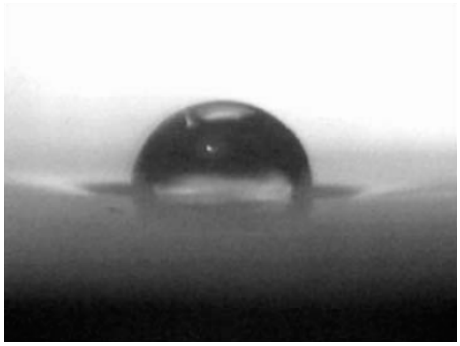


Figure 21. Thermocapillary levitation of a droplet (silicone oil) over the bath of the same liquid. In this case, the temperature of the droplet is kept below that of the bath, resulting in thermocapillary convection flowing in the opposite direction from the one proposed in the present research. Source: Savino, *et al.* (2003).

Savino, *et al.* (2003) presented a droplet flotation enabled by the presence of thermocapillary convection. Their flotation scheme is very similar to Dell'Aversana's demonstration shown in Figure 9, with the only difference being the prescribed temperatures on the respective surfaces. In Savino's demonstration (Figure 21), the

temperature of the droplet is kept below that of the liquid bath underneath, which is opposite from the Dell'Aversana's demonstration using a warmer droplet above a cooler bath. As a result, the directions of the motion of thermocapillary convection between these two situations are opposite to one another. In fact, the system studied by Savino, *et al*. will not be able to levitate a droplet if tried on a **solid** surface because the free-surface motion helps drain the film instead of supplying one. Although these levitation schemes are intriguing from physical perspectives, they may be not be easily integrated into an application due to a lack of controllability over the motion of the droplet.

A well-known method to induce a motion to bubbles and droplets in a suspending medium or microgravity is to impose a temperature gradient. For example, Balasubramaniam, *et al.* (1996) and Xie, *et al.* (1999) were able to show that droplets in microgravity moved with speeds $O(1\ mm/s)$ in a temperature gradient field of $O(1\ K/mm)$. Furthermore, the speed of motion increased with the increasing magnitude of the temperature gradient. On the other hand, these schemes are not well-suited for LOC applications on earth, due to the need for a suspending fluid phase in order to make the droplet neutrally buoyant.

The proposed idea of droplet levitation that exploits mechanisms of thermocapillary nonwetting can be of a very practical interest if proven feasible. The advantages of the presented levitation scheme were discussed in the previous section. These advantages include: (1) no necessary prefabrication of microchannels and mechanical pumps; and as a result, (2) no complications associated with the flow control; (3) versatility of the test surface that allows a variable system configuration depending on the demand of the testing; and (4) minimization of sample contamination by encapsulating a droplet within a protective layer of another liquid.

The following sections will discuss the methodologies used in the present research in order to realize a reliable operation of permanent nonwetting s a load-bearing system (Chapters 3 and 4) and demonstrations of droplet levitation and its controlled transport (Chapter 5).

3. Nonwetting-System Failure

3.1. Failure load measurement

One of the important constraints when designing a load-bearing system that exploits thermocapillary permanent nonwetting is the maximum allowable load. For example, a design engineer is interested in finding whether a given load can be sustained by a particular system's configuration, such as temperature difference and the viscosity of the liquid. By understanding characteristics of the failure load associated with these variables of interest, an engineer can design reliable systems.

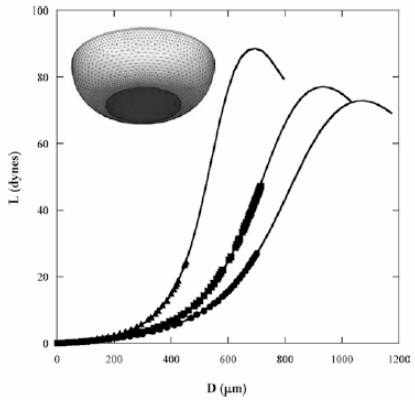


Figure 22. Comparison of loading curves between Surface Evolver (solid lines) and experiments (dots). The plot shows results for three *pendant* droplets of different volumes on a 3 *mm* disk. The curves from left to right correspond to small to large droplets. Source: Dell'Aversana & Neitzel (2004).

The present work is aimed at quantifying failure load. Here, an indirect method has been implemented in order to determine the load on a droplet with the aid of Surface Evolver. This method is based on a demonstration presented in Dell'Aversana & Neitzel (2004), in which Surface Evolver was employed for evaluating deformation-induced loads on a nonwetting droplet. Their result in Figure 22 shows a remarkable agreement between the loading characteristics obtained from Surface Evolver (solid lines) and the experiment (dots) for three volumes of pendant, silicone oil (5 *cSt*) droplets, pinned to a 3 *mm* disk. One important observation is deduced from their result. The load on a droplet is solely determined from an increase in capillary pressure induced by the deformation. This idea is incorporated into the present studies of failure loading. The experiment measures the relative displacement of a nonwetting system at failure and Surface Evolver is used to compute the corresponding failure load.

3.2. Experimental Apparatus

An experimental apparatus has been devised to measure the failure displacement of a nonwetting system. Figure 23 shows a schematic of the system primarily used for the present study. The relative displacement is measured from the point of "initial" contact, defined as a reference point where a deformation (and corresponding load) is introduced on a droplet. This point is detected by interferometry, which enables the contours of liquid-gas interface to be visualized as black-and-white interference patterns. Once the droplet is deformed, the interference pattern changes accordingly.

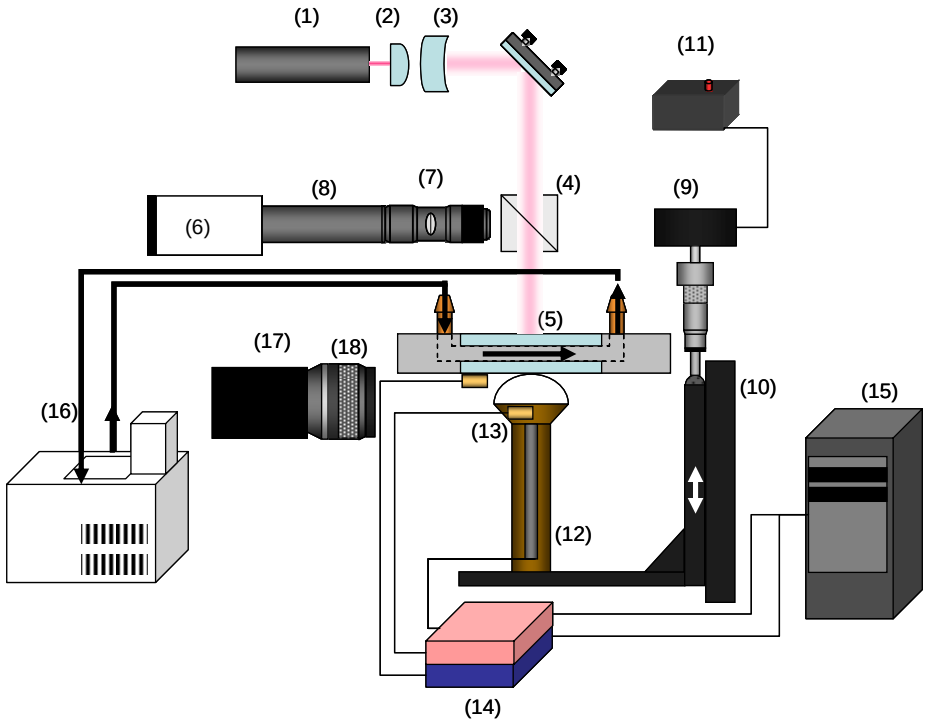
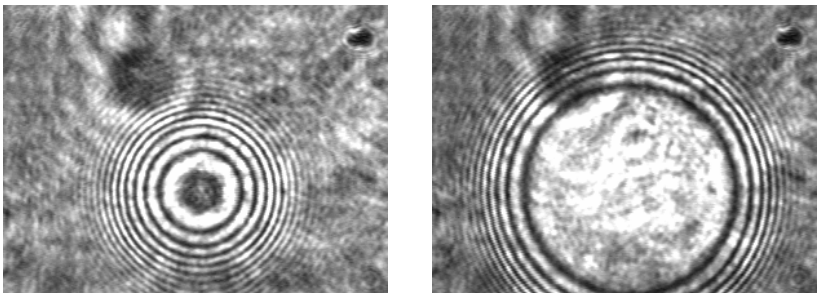


Figure 23. Schematics of the experimental apparatus.

A Fizeau interferomer is employed in the experimental apparatus for visualizing droplet deformations. It is comprised of a He-Ne laser beam with a wavelength, $\lambda = 632.8\ nm$ with an output of $< 5mW$ (1: Melles Griot, Model No. 6628002-003), passing through diverging- (2: Newport, CA1) and converging- (3: Newport, LFM-1) lenses, acting as a beam expander. The expanded beam is directed toward a beam splitter

(4: Melles-Griot, 03BSL043), and down onto a cooled glass surface (5). The reflected portion of the laser from the bottom of the glass acts as the reference wave, which interferes with another portion that reflects off of the deformed free-surface of the droplet. The optical path difference between these beams generates interference patterns, yielding contours of the free-surface.



(a) (b)

Figure 24. Interference patterns on a nonwetting droplet a) just prior to a loading, with the intensity profile similar to Newton's Ring and; b) after a few-microns displacement, showing a flattened top.

The initial contact is detected by observing changes in interference patterns associated with a deformation induced on the surface of a droplet. A CCD camera (6: Dage, MTI-CCD 72), equipped with a microscope objective (7: Navitar, Zoom 6000) and 2× adaptor tube (8: D.O. Industries, Cat. No. 6030), is used to monitor the interference patterns at the top of a nonwetting droplet. Just prior to a loading, the interference pattern takes on a shape of Newton's Rings due to the quasi-hemispherical nature of an undeformed droplet (Figure 24(a)). The pattern is disturbed when the droplet is displaced from the contact point, flattening the top of the droplet due to applied load, as shown in Figure 24(b). The reference point is determined manually by placing the droplet back to the point where the initial deformation is detected.

Following the establishment of the reference point, the droplet is squeezed against the glass plate, coated with tin-oxide (AFG Industries). The coating is necessary for grounding the surface, in order to eliminate static electrical charge from building up and disturbing the surface of the silicone-oil droplet.

The squeezing is applied by a stepper-motor (9: Vexta, PH266M-E06) coupled to a 1-inch linear translation stage (10: Daedal Inc.). The number of steps displaced by the

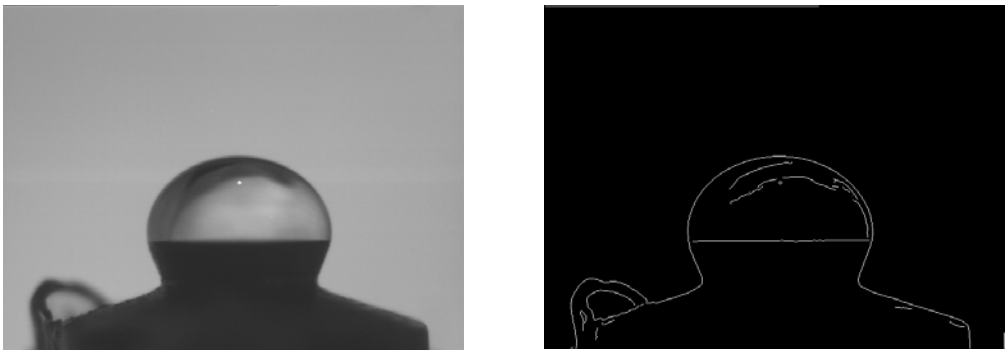
motor is counted by a custom-made controller (11) designed by the Mechanical Engineering Electronics Shop at Georgia Tech. Each step (0.9^{o}) corresponds to a linear displacement of 1.5875 μm.

The temperature difference, the driving force of thermocapillary nonwetting, is introduced by heating the droplet and cooling the glass surface. The droplet is heated by a cartridge heater (12: Watlow, C2A5-L12T) placed inside the copper pedestal. The temperature is measured about 3 *mm* below the tip of the disk, using a thermistor (13: Oven Industries, TS136-170) with a ± 0.1 °C resolution. The hot-side temperature is actively regulated by a proportional-integral-derivative (PID) controller (14: Oven Industries, 5C7-362) interfaced with a personal computer (15: Dell Dimension 4600, 2.8GHz CPU and 1GB of RAM). This PID controller is designed for controlling a thermoelectric module, the temperature of which is regulated by passing electrical current in one direction for heating and another for cooling. Due to this bi-directionality of the controller's operation, the resistive (cartridge) heater used in the apparatus would be heated up continuously. To avoid this, a diode was placed on the electrical circuit of the cartridge-heater, restricting the electrical current to flow only in one direction. The surface of the glass is cooled by passing water above it, the temperature of which is regulated by a circulator (16: Haake, D8-GH). Because the temperature of the glass surface is stable, there was no need for an elaborate controlling mechanism. The mean temperature T_m, defined by the average between the hot and cold side temperatures ($T_m = \left(T_H - T_C\right)/2$) has been maintained at room temperature (nominally 25 °C) throughout the experiment. The standard deviation of the temperature fluctuation of these surfaces is less than ± 0.1 °C, which is below the resolution of the thermistor.

Another variable from the experiment is the volume of the droplet. In order to determine the volume, an algorithm based on image analysis was developed. The method gives more accurate results than are obtained by reading pipette dispensers. For example, an error, as high as 30%, has been noted from pipette readings.

The volumes are evaluated from images containing the droplet. The images are recorded by a CCD camera (17: Pulnix, Progressive Scan-TM9701) with a camera lens (18: Minolta MD 50*mm*) to zoom into a droplet for a more accurate measurement. To

proceed with the volume computation, the profile of the droplet's interface must be distinguished from the background. This is done by diffusing the light behind a droplet, generating a sharp contrast at the liquid-gas interface as seen in Figure 25(a). An edge-detection algorithm ("canny method") in MATLAB is applied to the image, resulting in a binary image as seen in Figure 25(b). The value of "threshold" for the edge-detection has been kept around 0.1 throughout the experiment.



(a) (b)

Figure 25. (a) Image of a droplet on a 3 *mm* disk. A sharp contrast at the liquid-gas interface is generated by passing light, placed behind the droplet, through a diffusing medium. (b) Binary image after applying MATLAB's edge-detection algorithm.

The volume is then computed from the binary image using an integral that assumes axisymmetry of the droplet profile

$$\mathscr{V} = \pi \int_0^H r^2(z)\,dz, \qquad (10)$$

where $r(z)$ is the half-width of the droplet at any vertical height z above the pedestal and H is the droplet height. Simpson's 1/3 rule is used to integrate equation (10). Because the unit of the volume is given in $pixels^3$, a multiplier (in the unit of *mm/pixels*) is needed to convert the unit to mm^3. This multiplier is calculated from a calibration involving the known diameters of the disk (3 or 5 *mm*), and counting the number of pixels between the edges of the disk.

Two different techniques have been implemented for depositing droplets onto the disk. The first method employs a stepper motor, coupled to a linear translation stage, to dispense a liquid from a syringe. The working fluid is passed through a length of

Tygon® tubing and through a tiny hole (~ 200 μm) machined in the center of the disk support. The method produces relatively consistent volume sizes. The second method is more conventional, using a syringe and needle to place a droplet directly on a disk. In this case, the disk has no hole.

Two silicone oils with dynamic viscosities ν_l = 5 and 10 *cSt* (Dow Corning, 200® Fluids) have been tested. All of the experiments were carried out on a vibration-isolation table (Technical Manufacturing Corporation), minimizing transmission of vibrations from the environment.

3.3. Surface Evolver Computations

3.3.1. Methodologies

The loading curves obtained from Surface Evolver have been used to correlate failure displacements and failure loadings. The loading curve is unique for each droplet volume, therefore the computations will be time consuming if carried out for individual experimental runs. Instead, the loading curves have been evaluated for several volume sizes, and the failure load has been estimated at a point of interest by interpolation.

The following paragraphs outline the algorithms and procedures employed by the present Surface Evolver simulation. First, an equilibrium shape of a pinned droplet under the action of gravity must be obtained. The surface evolves into a shape of a sessile (or pendant) droplet, as Surface Evolver iterates its computation, minimizing the energy of a droplet. A typical output of a sessile-droplet is presented in Figure 26(a).

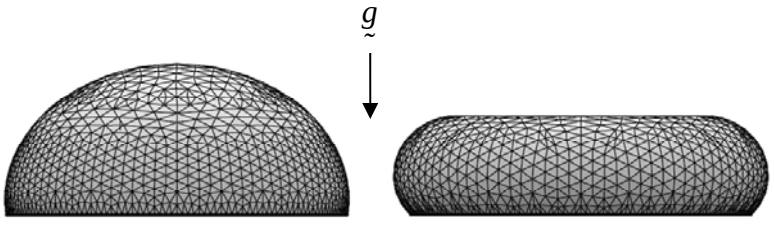


Figure 26. Evolved surfaces of a droplet. (a) Pinned droplet under an action of gravity, without squeezing. (b) Same droplet after some squeezing. The gravity vector is shown as an arrow.

In order to mimic the nonwetting solid surface, a "nonpositive" constraint is prescribed to a virtual plane restricting the fluid elements from surpassing beyond it. This constraining plane, initially placed at some distance above the droplet before the loading process, is brought down to the top of the droplet. The contact of the plane with the apex of the droplet is detected from a change in the system energy. The system energy remains the same while the plane moves in the empty space above the droplet, changing only when a deformation (due to the nonpositive-constraint) is applied on the droplet. This location is defined as the "initial" contact point, from which the load is defined.

A relative compression is applied from this point, by lowering the constraining plane. During early stages of the compression, the plane is lowered by 10 μm at a time. During the final stages of the compression, the step size is reduced to1.5875 μm, which is the same increment size as the linear translation stage, and the squeezing is applied until shape instability (discussed in more detail in the section 3.3.3 Shape Instability) is triggered.

Each time the droplet is deformed by lowering the plane, the energy of a droplet is minimized, yielding an equilibrium shape as seen in Figure 26(b). The criterion for the global energy-minimum at each squeezing of the droplet is determined to be the point when energy changes between each iteration becomes less than 1.0×10^{-7}. After the system's energy is minimized for each displacement of the plane, the load F is computed from

$$F = -\frac{\delta E}{\delta z} \qquad (11)$$

where E is the minimized energy of the system and z is the coordinate along which the hypothetical nonwetting plane is displaced. A 2nd-order-accurate, finite-difference expression is used to compute the derivative in equation (11). Details of the load computation are discussed in the Surface Evolver manual, Example 3.7, **Column of the Liquid Solder** section, which can be downloaded from website (http://www.susqu.edu/facstaff/b/brakke/evolver/). Specifically, the formulation described in the **Ball Grid Array Example** from the online tutorials

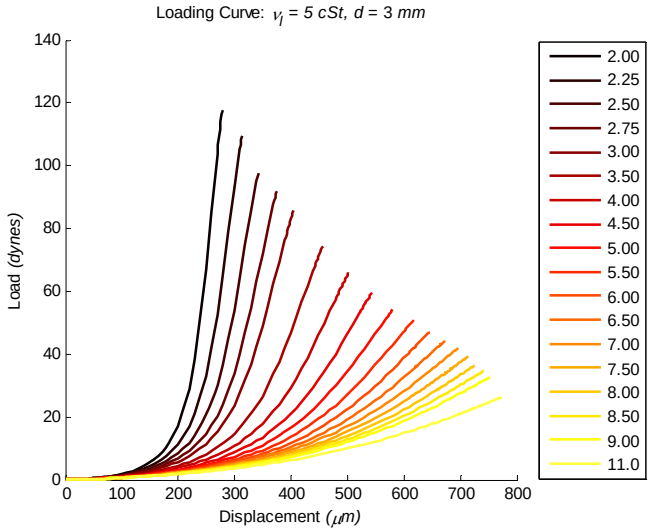
(http://www.susqu.edu/brakke/evolver/bga/bga.htm) has been implemented for the present analysis.

3.3.2. Results

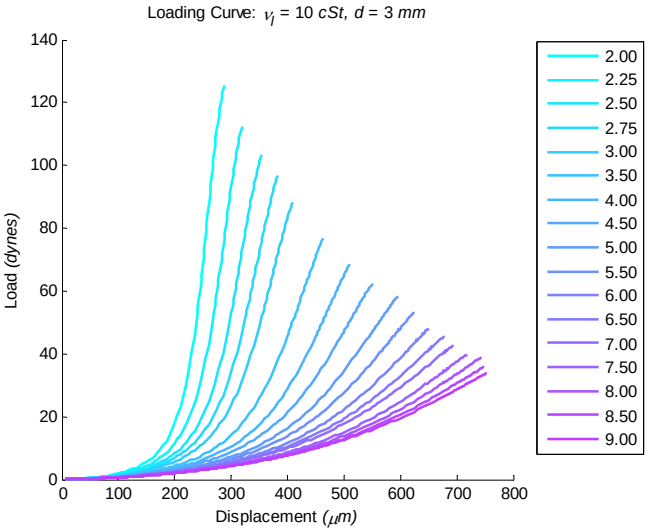
Surface Evolver simulations are carried for droplets using the surface tension σ and density ρ of silicone oils (5 and 10 *cSt*), contact line of which is pinned to a circular boundary with 3 and 5 *mm* diameters. Because the mean temperature between the hot and cold surfaces has been maintained at room temperature (25 °C), the fluid properties at this temperature are employed. Some of the relevant properties of the liquid and the air are included in Table 1. In the following sections, the results from Surface Evolver will be presented in terms of (the fluid properties associated with) the viscosity of the droplet.

Table 1. Properties of silicone oils and air used for the computations.

	Dow Corning 5 *cSt* silicone oil	Dow Corning 10 *cSt* silicone oil	air
$\nu \quad (m^2\, s^{-1})$	5×10^{-6}	10×10^{-6}	1.6×10^{-5}
$\rho \quad (kg\, m^{-3})$	913	935	1.18
$\alpha \quad (m^2\, s^{-1})$	9.0×10^{-8}	9.5×10^{-8}	
$\sigma \quad (kg\, s^{-2})$	1.97×10^{-2}	2.01×10^{-2}	
$\gamma \quad (kg\, s^{-2}\, K^{-1})$	6.9×10^{-5}	6.9×10^{-5}	
$C_p \quad (J\, kg^{-1}\, K^{-1})$	1632	1506	



(a)



(b)

Figure 27. Surface Evolver computations of the load on droplets as a function of relative squeezing against a nonwetting plane. (a) Properties of 5 *cSt* silicone oil on a 3 *mm* disk support. (b) 10 *cSt* silicone oil on a 3 *mm* disk support. The legend indicates the size of the volume in mm^3.

The loading curves presented in Figure 27(a) and (b) show relationships between the load (*dynes*) and the relative displacement (μm) for droplets of various volumes. The results are obtained using the fluid properties of 5 and 10 *cSt* silicone-oil droplets with dynamic viscosities on a disk having the diameter $d = 3\ mm$. The legends indicate the

volume of droplets in mm^3. As indicated by a high rate of change in the load with respect to the displacement, small droplets exhibit greater "stiffness" that large ones. This is due to the high curvature changes (and thus capillary-pressure increases) resulting from squeezing a small droplet. Figure 28 presents the load curve for using the properties of 10 *cSt* silicone-oil droplets with on $d = 5\ mm$.

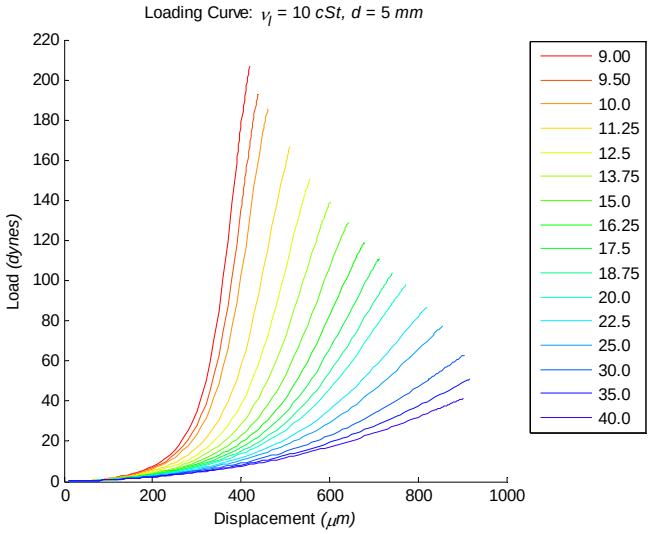


Figure 28. Surface Evolver computations of the load on droplets as a function of relative squeezing against a nonwetting plane. The result is for the properties of 10 *cSt* silicone oil on a 5 *mm* disk support. The legend indicates the size of the volume in mm^3.

Figure 29 is the load curve for **pendant** silicone-oil droplets with $\nu_l = 5\ cSt$ and $d = 3\ mm$. By comparing the loading curves between sessile and pendant droplets, as shown in Figure 30(a), the results from the latter case are slightly shifted towards the right (for the same droplet volumes). That is to say, given a relative displacement the resultant load on the pendant droplet is smaller than on the sessile one. The difference in the loading characteristics between these systems is due to their initial static shapes assumed under the gravitational field. Figure 30(b) and (c) are inserted to illustrate this effect, showing the pendant droplet to sag under its weight while the sessile droplet is flattened. Because of the sagging, it takes a larger squeezing on a pendant droplet to equal the capillary pressure (and thus the applied load) of a sessile drop. The discrepancy between the loading curves becomes more significant with the increase in droplet volume,

resulting in more sagging imparted on the larger pendant drop, as can be seen in the result for $\mathscr{V} = 8.0\ mm^3$ in Figure 30(a).

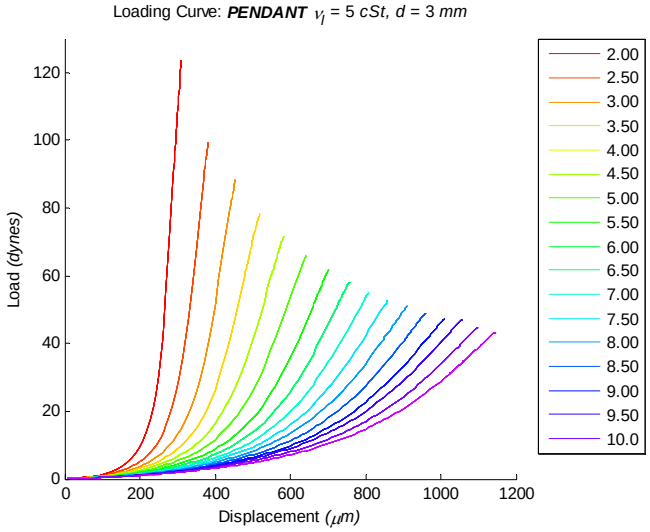


Figure 29. Surface Evolver computations of the load on droplets as a function of relative squeezing against a nonwetting plane. The result is for *pendant* droplets with properties of 5 *cSt* silicone oil on a 3 *mm* disk.

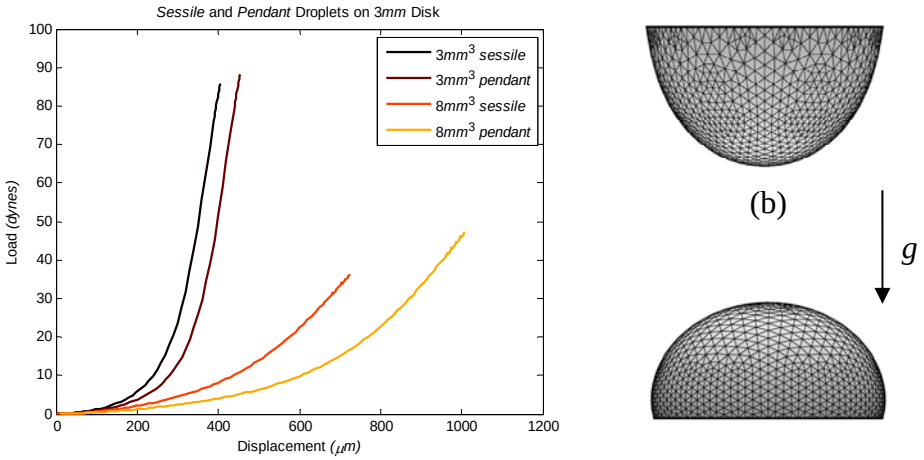


Figure 30. (a) Comparisons of loading characteristics between pendant and sessile droplets for two different volumes. Equilibrium profiles for (b) pendant and; (c) sessile droplets with the volume 8.0 mm^3.

3.3.3. Shape Instability

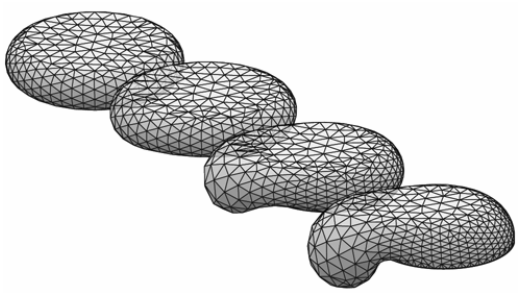


Figure 31. Sequence of shape instability from a Surface Evolver simulation. The droplet translates laterally and spills from the disk. The process effectively reduces the overall energy of the system. Result is from 5 *cSt* silicone oil, with volume 9.0 mm^3, on a 3*mm* disk.

All of the Surface Evolver simulations are carried out until "shape instability" is triggered. The sequence of shape instability is presented in Figure 31 for a 5 *cSt* droplet with $\mathscr{V} = 9.0\ mm^3$. Before instability sets in, the shape of the droplet stays axisymmetric. As some threshold of squeezing is exceeded, the droplet suddenly bulges out on one side, resulting in a lateral translation. In the end, the droplet "spills" from the disk (although the computation does not capture the actual pinning-failure due to the perfectly pinned contact line at the disk edge). As a consequence of the process, the overall energy of the system is reduced abruptly. It is noted here that the appearance of shape instability is very sudden. This process occurs over a one step increment in the displacement of the nonwetting plane (1.5875 μm). The sudden nature of the process resembles a buckling instability of a slender bar, initiated as a result of load application along the symmetry axis of the bar.

This shape instability was observed in all of the simulations. Initially, it was considered that numerical errors were responsible for the appearance of such behavior. In order to test this idea, a simulation was repeated with a finer mesh. Comparison of the results obtained for the finely and coarsely meshed droplets shows that instability is insensitive to the mesh size, eliminating the numerical errors as the cause of the event, although they certainly serve as the source to permit the growth of unstable modes. It is worthwhile to note that shape instability was not mentioned in the similar numerical computations carried out by Dell'Aversana & Neitzel (2004). Their model allowed for even larger displacement, well beyond the point of instability, where applied load

decreased with the relative displacement, resulting in the appearance of a maximum point on the loading curve. In the present analysis, however, shape instability was triggered before the loading curve reached its maximum point. It is suspected that the simulations from Dell'Aversana & Neitzel may have imposed an axisymmetric constraint, making a droplet insensitive to nonaxisymmetric perturbations.

The displacement, load, energy, and pinning contact-angles at the onset of instability are presented in Figure 32(a), (b), (c), and (d) respectively, for the liquid properties of 5 *cSt* silicone-oil droplets on 3 *mm*-diameter disk. As seen from the plot in Figure 32(a), larger droplets can accommodate larger displacements than smaller droplets. The cubic fit

$$\mathscr{D} = 0.3455\mathscr{V}^3 - 13.92\mathscr{V}^2 + 184.9\mathscr{V} - 36.55 \qquad (12)$$

has been obtained from the data, characterizing the displacement $\mathscr{D}$ (μm) as a function of the volume $\mathscr{V}$ (mm^3), with an R-squared value of 0.99. The load, on the other hand, shows an inverse relationship with the volume. This is due to the stiffness of the smaller droplet having a reduced height. An analogy can be drawn again to the buckling process; a stiff (short and wide) bar can tolerate a higher load than a soft (long and thin) one. The power law is used to fit the load F at the onset of shape instability, resulting in the expression

$$F = 215.6\mathscr{V}^{-0.8529}. \qquad (13)$$

Here the fit has an R-squared value of 0.99. Finally, the energy of the system at the onset of shape instability has been fitted with a linear function

$$E = 0.341\mathscr{V} + 1.502 \qquad (14)$$

with an R-squared value of 0.99.

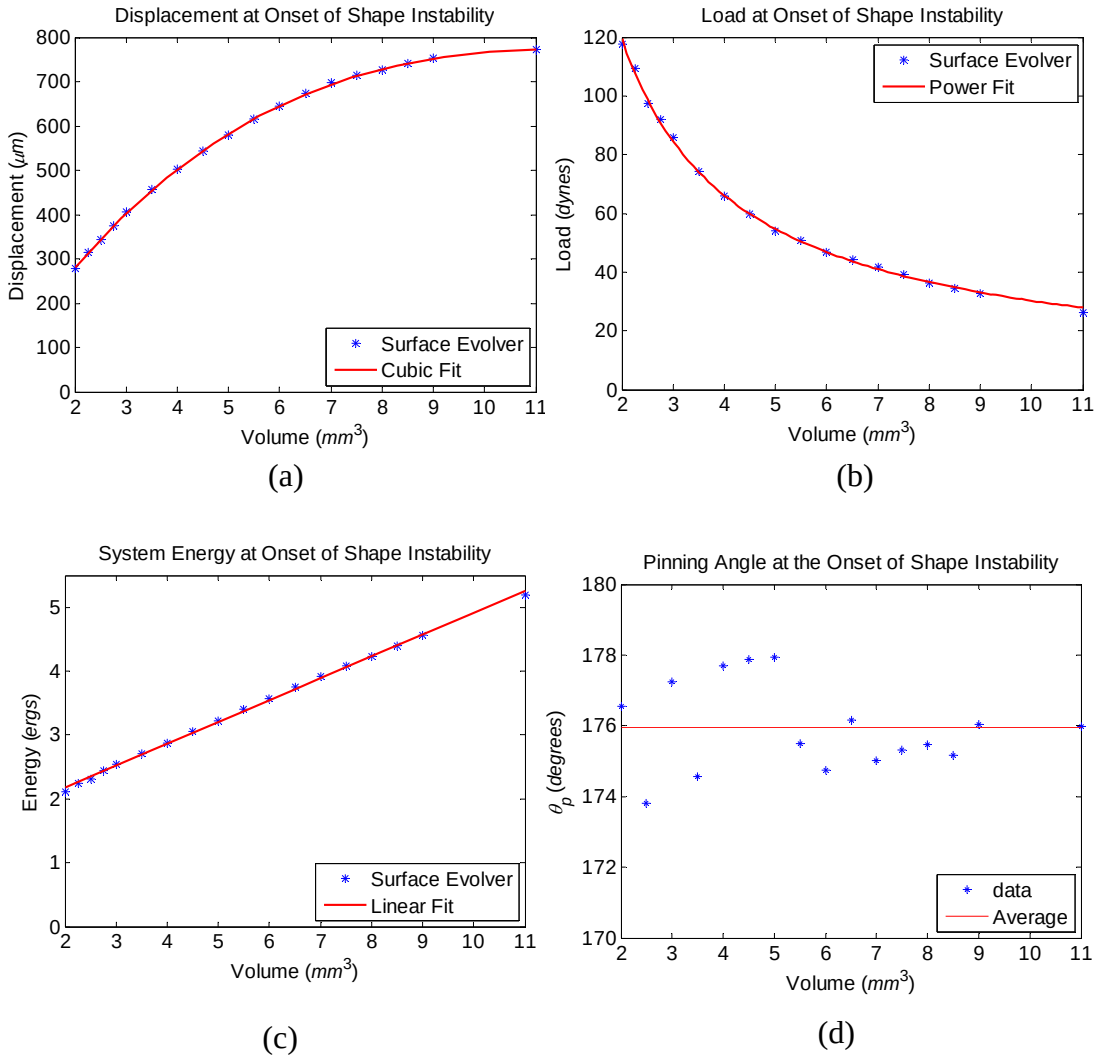


Figure 32. (a) Displacement; (b) load; (c) energy and; (d) pinning contact angle at onset of shape instability for various sizes of droplet. The result is for the droplets with the properties of 5 *cSt* silicone oil on a 3 *mm* disk.

The contact angle at the onset of shape instability is determined by the following argument. A virtual plane is defined in Surface Evolver, and is used to slice across the droplet at some arbitrary height h above the pinning contact line. Brakke's subroutine "slice", has been used to measure the circumference of a circle, obtained by intersecting the virtual plane and the surface of the droplet at height h (= 10 μm). The first-order estimate used in this analysis evaluates the pinning angle θ_p by

$$\theta_p = 90 + \tan^{-1}\left(\frac{R_p - R_0}{h}\right), \qquad (15)$$

where R_p and R_0 are the radii of the circle (of intersecting surfaces) and the pinned contact-line, respectively (see Figure 33). Since the result seems to be independent of the volume sizes, the average value of 176° has been used to characterize the trend. The standard deviation of the data about the average is 1.25º. Generic trends for all of these curves are similar for the droplets with properties of 10 *cSt* silicone oil and on a 5 *mm* disk.

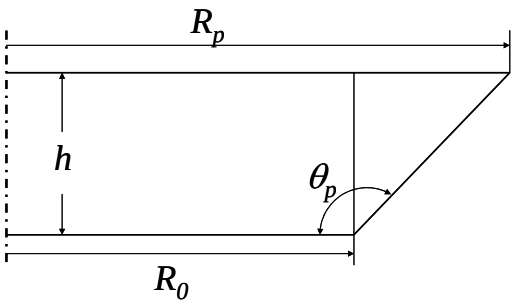
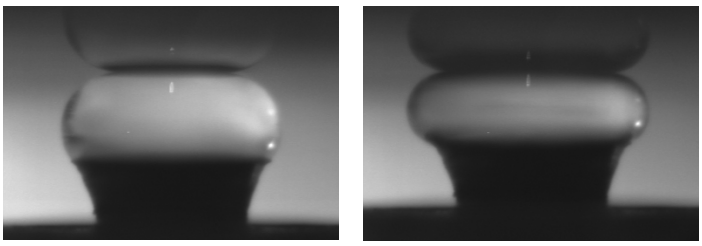


Figure 33. Diagram showing the relevant parameters to estimate the pinning contact angle at the onset of shape instability. The values were above 90 ° for all the cases.

Shape instability has been witnessed in experiments as well. During the early stages of squeezing, the shape of a droplet is axisymmetric as shown in Figure 34(a). Just prior to pinning failure, however, the symmetry is broken, resulting in a slight bulging of the interface, which is displaced towards left side of the image, as can be seen in Figure 34(b). A rough estimate of the pinning contact-angle from this image is 150º, which is less than the one inferred from Surface Evolver. A speculation on the causes of these differences will be discussed in the final paragraph of this section. Interferometric observations have also revealed the lateral translation, indicated by a shift of the fringe patterns just before pinning failure.



(a) (b)

Figure 34. Images of nonwetting droplet (a) in early stages of loading with an axisymmetric profile and; (b) prior to pinning failure with a bulged interface (towards left of the droplet).

A similar instability has been investigated by Bradley & Weaire (2001), who used Surface Evolver to squeeze two droplets against each other, mimicking the situation encountered in a permanent **noncoalescence** system. The authors reported that the two droplets maintain symmetry during the early stages of squeezing, until instability is triggered and the droplets slide apart from each other.

It is plausible that any droplet compressed against a surface slides to one side in an attempt to reduce the system energy. As can be seen in Figure 35, the energy of a system ($\mathscr{V}$ = 5 mm^3, ν_l = 5 cSt, d = 3 mm) is abruptly reduced at the onset of shape instability. This happens over a one-step increment in the nonwetting-plane's displacement, which corresponds to 1.5875 μm.

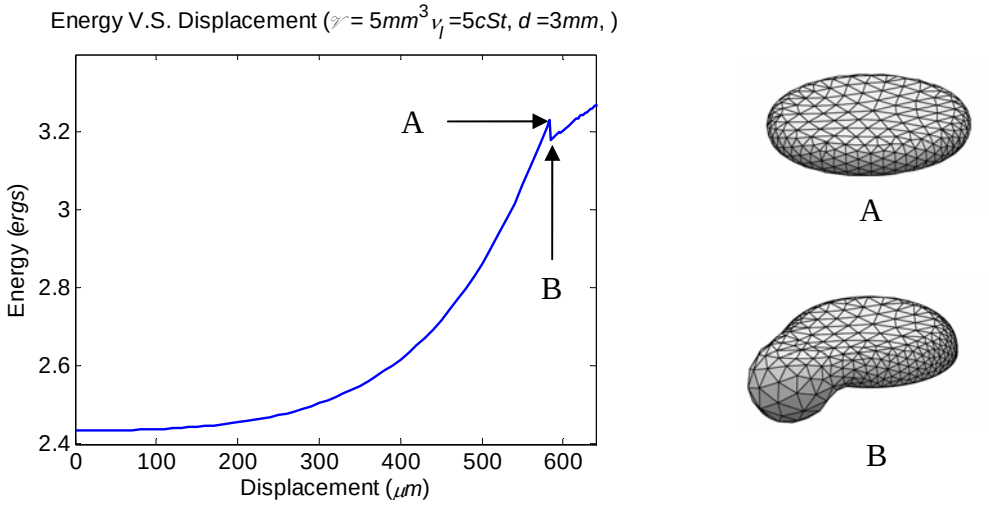


Figure 35. Energy of the droplet as a function of relative displacement. A sudden decrease in the energy occurs at the instance of shape instability. Arrows indicate before (A) and after (B) shape instability occurring over a 1.5875 μm displacement. Surface Evolver outputs corresponding to these locations are shown on the right. The case is for $\mathscr{V}$ = 5 mm^3, ν_l = 5 cSt, d = 3 mm.

Droplets in Surface Evolver can be squeezed further against the nonwetting plane to cause shape instability, than the actual droplets from the experiments resulting in a lateral translation. The discrepancy is believed to be due to a slight misalignment between the disk and the glass planes that exists in the experiment, resulting in the translation of the droplet an early stage of squeezing due to unbalanced pressure distribution in the drop. Also, uneven film thickness within the contact region (Figure 7)

may introduce an uneven pressure distribution, thereby pushing the liquid to a side. In addition, the boundary condition at the pinning contact-line is imperfect in the experiment, allowing the droplet to move at the disk edge, whereas it is prohibited from moving in Surface Evolver simulation.

3.3.4. Correlating Failure Displacement Data to the Load

The failure-displacement data gathered from experiments must be converted to failure loads. This is done by interpolating on a loading surface, which relates the load F to the relative displacement $\mathscr{D}$ for a given volume size $\mathscr{V}$ of a droplet. In general, the loading surface depends on displacement and the volume, $F = F\left(\mathscr{D};\mathscr{V}\right)$. An example of the loading surface is presented in Figure 36 for the case of $\nu_l = 5\ cSt$ and $d = 3\ mm$.

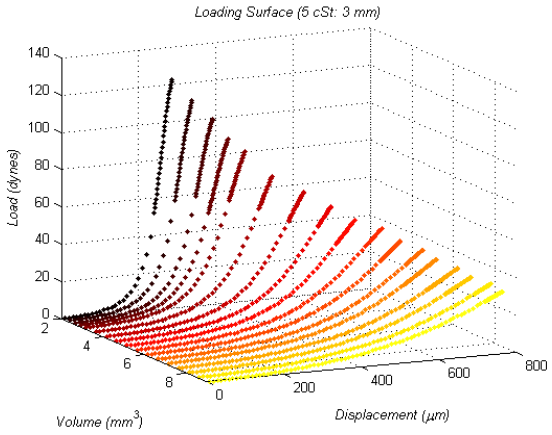


Figure 36. Load surface generated from a series of loading curves. The surface is for the case ν_l = 5 *cSt* and *d* = 3 *mm*. Bilinear interpolation is used to determine the failure loading.

Bilinear interpolation is used to estimate the load F_e at the data points $\left(\mathscr{D}_e,\mathscr{V}_e\right)$ from a surface prescribed by $F = F\left(\mathscr{D};\mathscr{V}\right)$. Figure 37(a) is inserted for naming conventions employed by the present interpolation scheme. In the present analysis, the following conditions are assumed to hold

$$\mathscr{D}_1 < \mathscr{D}_e < \mathscr{D}_2, \tag{16}$$

$$\mathscr{D}_3 < \mathscr{D}_e < \mathscr{D}_4 \tag{17}$$

$$\mathscr{V}_1 < \mathscr{V}_e < \mathscr{V}_2, \tag{18}$$

with

$$F_i = F_i\left(\mathscr{V}_1, \mathscr{D}_i\right) \qquad i = 1,2 \tag{19}$$

$$F_j = F_j\left(\mathscr{V}_2, \mathscr{D}_j\right) \qquad j = 3,4 \tag{20}$$

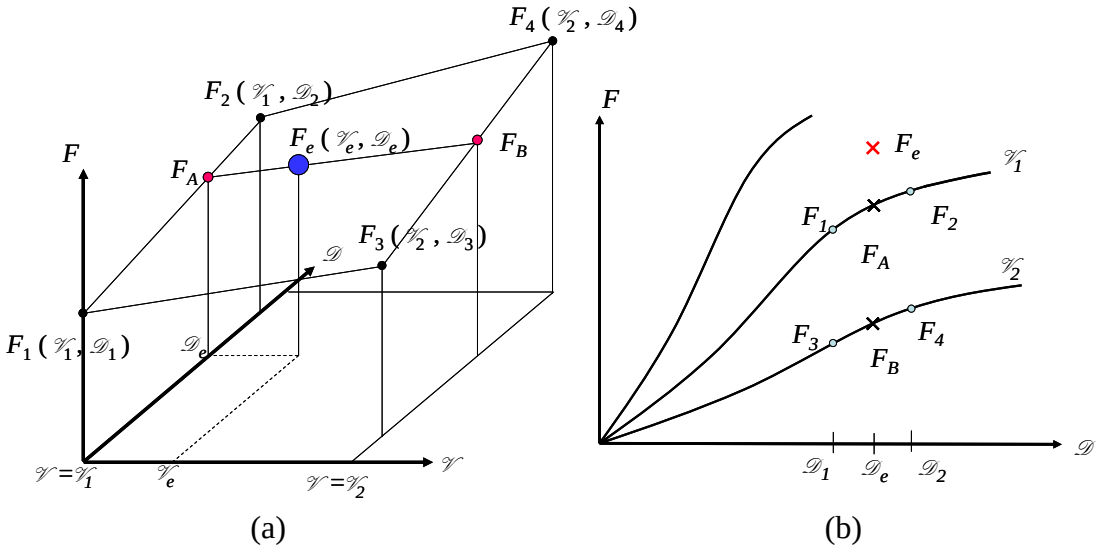


Figure 37 (a) Illustration of the surface used by the bilinear interpolation. The load is estimated at the data point, $F_e = F_e(\mathscr{V}_e, \mathscr{D}_e)$. (b) Data point lying outside of interpolation range (red-cross) must be evaluated by extrapolation scheme.

The procedure first interpolates along the $\mathscr{D}$ –axis on $\mathscr{V} = \mathscr{V}_1$ and $\mathscr{V} = \mathscr{V}_2$ estimating values $F_{A,B}\left(\mathscr{V}_{1,2}; \mathscr{D}_e\right)$. The formula for the estimation is given by

$$F_{A,B} = F_{1,3} + \frac{\left(F_{2,4} - F_{1,3}\right)}{\left(\mathscr{D}_{2,4} - \mathscr{D}_{1,3}\right)}\left(\mathscr{D}_e - \mathscr{D}_{1,3}\right) \quad \text{on} \quad \mathscr{V} = \mathscr{V}_{1,2}. \tag{21}$$

The second interpolation is carried along the $\mathscr{V}$ –axis at $\mathscr{V} = \mathscr{V}_e$ yielding the estimate of the load at the data point $F_e\left(\mathscr{D}_e, \mathscr{V}_e\right)$

$$F_e = F_A + \frac{\left(F_B - F_A\right)}{\left(\mathscr{V}_2 - \mathscr{V}_1\right)}\left(\mathscr{V}_e - \mathscr{V}_1\right). \tag{22}$$

In some circumstances, data may lie outside of a range, *e.g.*, on the red-cross shown in Figure 37(b), prohibiting the above interpolation from being used. In this case, extrapolation is employed for the estimate. The first procedure is the same as in the

previous discussion, evaluating $F_{A,B}$ using equation (21). The second step is the extrapolation, defined as

$$F_e = F_A - \frac{\left(F_B - F_A\right)}{\left(\mathscr{V}_2 - \mathscr{V}_1\right)}\left(\mathscr{V}_1 - \mathscr{V}_e\right). \tag{23}$$

3.3.5. Error Estimate

Error bounds associated with the load computations are estimated by employing the propagation of error analysis discussed in Kline & McClintock (1953) and Wheeler & Ganji (1996). The propagation of error w_R due to contributions from uncertainties in the measurement of displacement ($\Delta\mathscr{D}$) and the volume ($\Delta\mathscr{V}$) is defined as

$$w_R = \left[\left(\frac{\partial F}{\partial \mathscr{D}}\Delta\mathscr{D}\right)^2 + \left(\frac{\partial F}{\partial \mathscr{V}}\Delta\mathscr{V}\right)^2\right]^{1/2}, \tag{24}$$

where the partial derivatives are computed from the loading surface, $F = F\left(\mathscr{D}, \mathscr{V}\right)$. In this analysis, the variables are assumed to be independent and not correlated. The partial derivatives, $\partial F/\partial \mathscr{D}$ and $\left|\partial F/\partial \mathscr{V}\right|$, are computed from the loading surface of Figure 36 and are plotted in Figure 38(a) and (b), respectively. The magnitude of $\partial F/\partial \mathscr{V}$ is about 100 times that of $\partial F/\partial \mathscr{D}$, indicating that the major contribution of uncertainty derives from the errors associated the volume measurement.

Equation (24) requires quantifying the errors in the measurement of displacement, $\Delta\mathscr{D}$ and volume $\Delta\mathscr{V}$. For the present analysis, $\Delta\mathscr{D}$ is chosen as $\pm 10\ \mu m$ with a 90% confidence (10 μm corresponds to about 6 pulses sent to the stepper motor). The error in $\Delta\mathscr{V}$ is estimated by computing the volume of a droplet with known size, but deliberately introducing systematic errors by shifting images of the droplet. The error here simulates the human error involved in detecting edges of the pedestal, the process of which is required to determine the calibration constant for the volume computation. The estimates for $\Delta\mathscr{V}$ are 0.2 and 0.6 mm^3 (roughly 2 –10% of the volume range) for droplets on the 3

and 5 *mm* disks, respectively with a 90% confidence. The overall uncertainty w_R from equation (24) is plotted in Figure 38(c) for the same case presented so far.

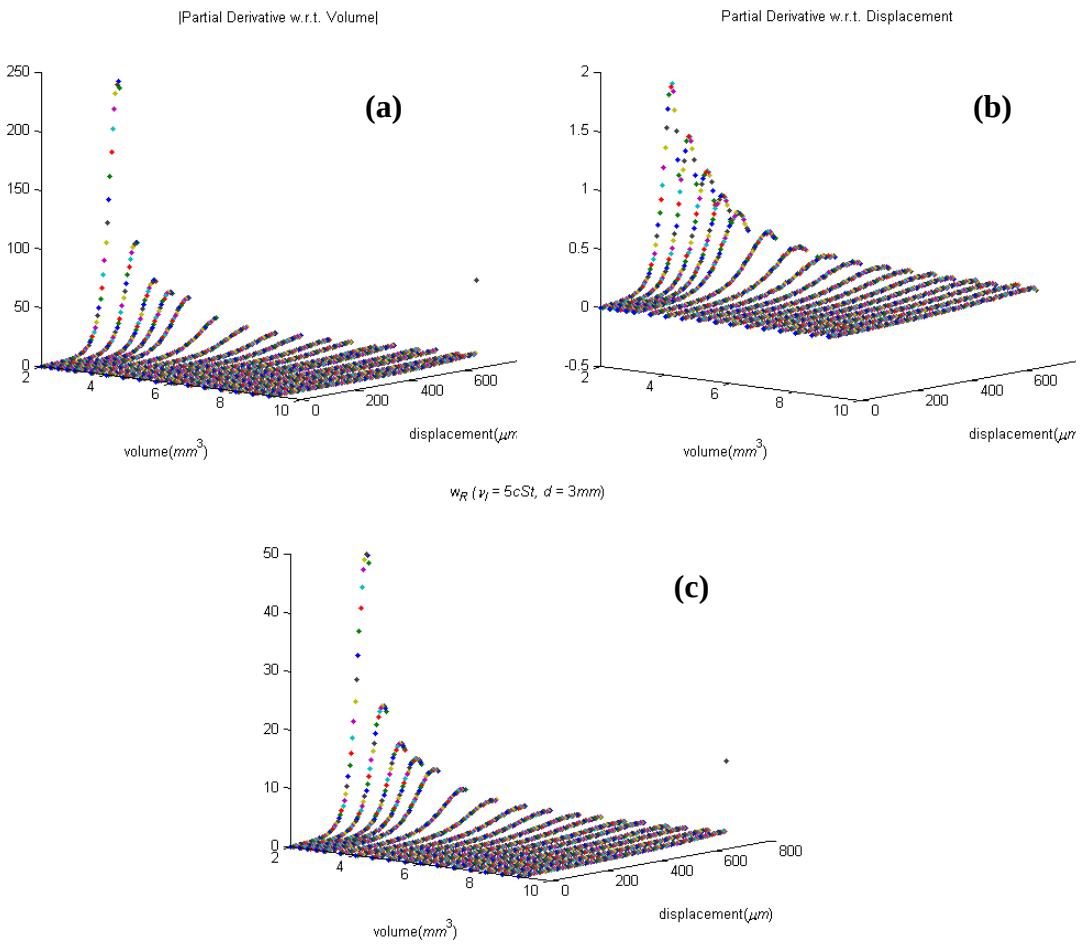


Figure 38. Surfaces of (a) $|\partial F/\partial \mathscr{V}|$; (b) $\partial F/\partial \mathscr{D}$ and; (c) w_R. The majority of the error is derived from volume-measurement, indicated by two-order-of-magnitude higher values of $|\partial F/\partial \mathscr{V}|$ than $\partial F/\partial \mathscr{D}$. The result in (c) is for 5 *cSt* oil on a 3 *mm* disk, and is based on $\Delta \mathscr{V} = 0.2$ *mm*^{3} and $\Delta \mathscr{D} = 10$ μm.

3.4. Experimental Results: Static-Failure

The experimental data of the failure displacement, under static conditions, is presented in this section. The results presented in Figure 39 and Figure 40 are for sessile silicone-oil droplets with ν_l = 5 and 10 *cSt* deposited on 3 *mm* disk, respectively under various temperature differences ΔT; Figure 41 is for the sessile droplets with ν_l =10 *cSt* oil on a larger disk (5 *mm*); Figure 42 is for the pendant droplets on a 3 *mm* disk.

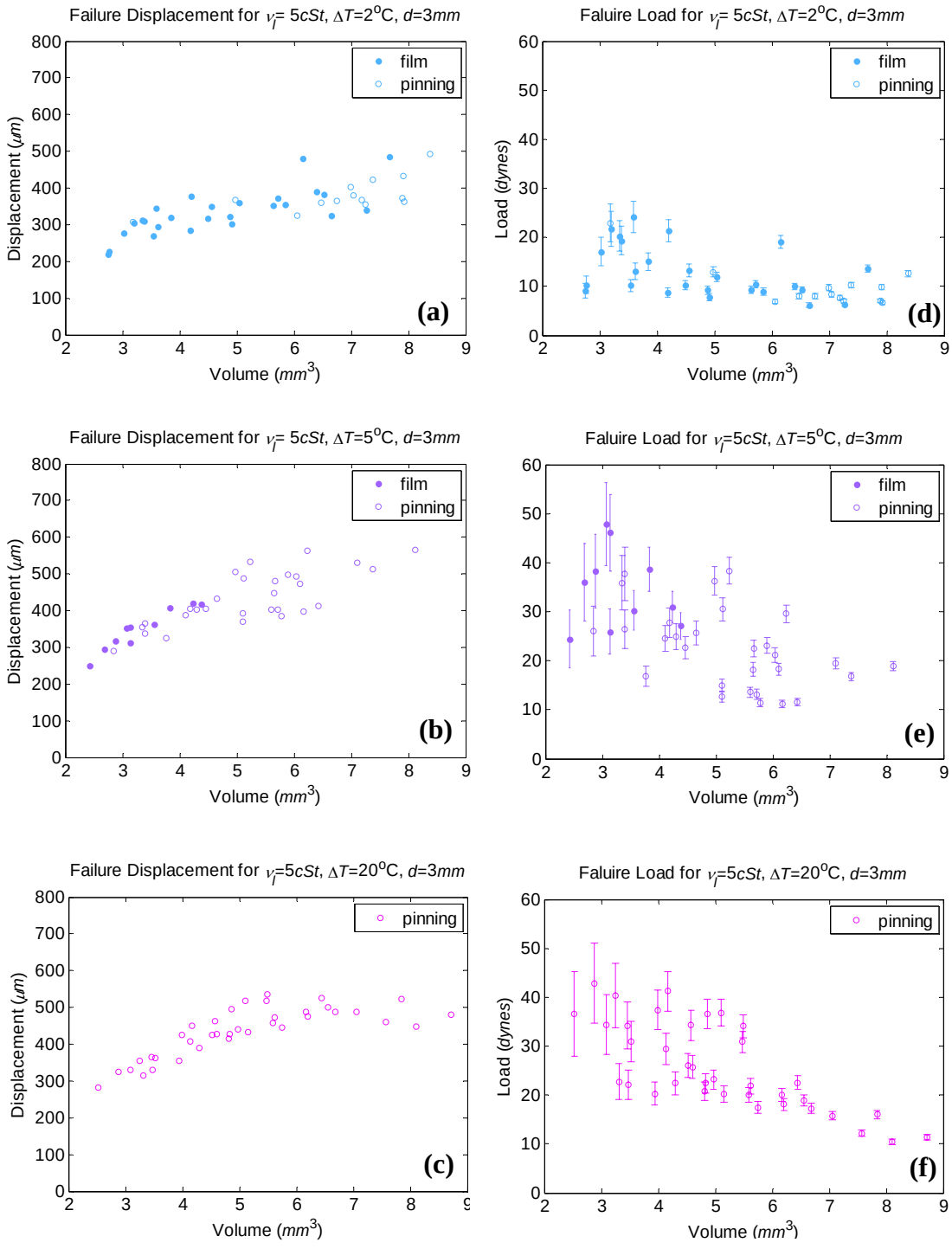


Figure 39. (a)-(c) Failure displacement of nonwetting, silicone oil droplets of ν_l = 5 *cSt* on a *d* = 3 *mm* disk. They correspond to the temperature differences at ΔT = 2, 5, and 20 °C, respectively. (d)-(f) Corresponding failure load. The results are for sessile droplets.

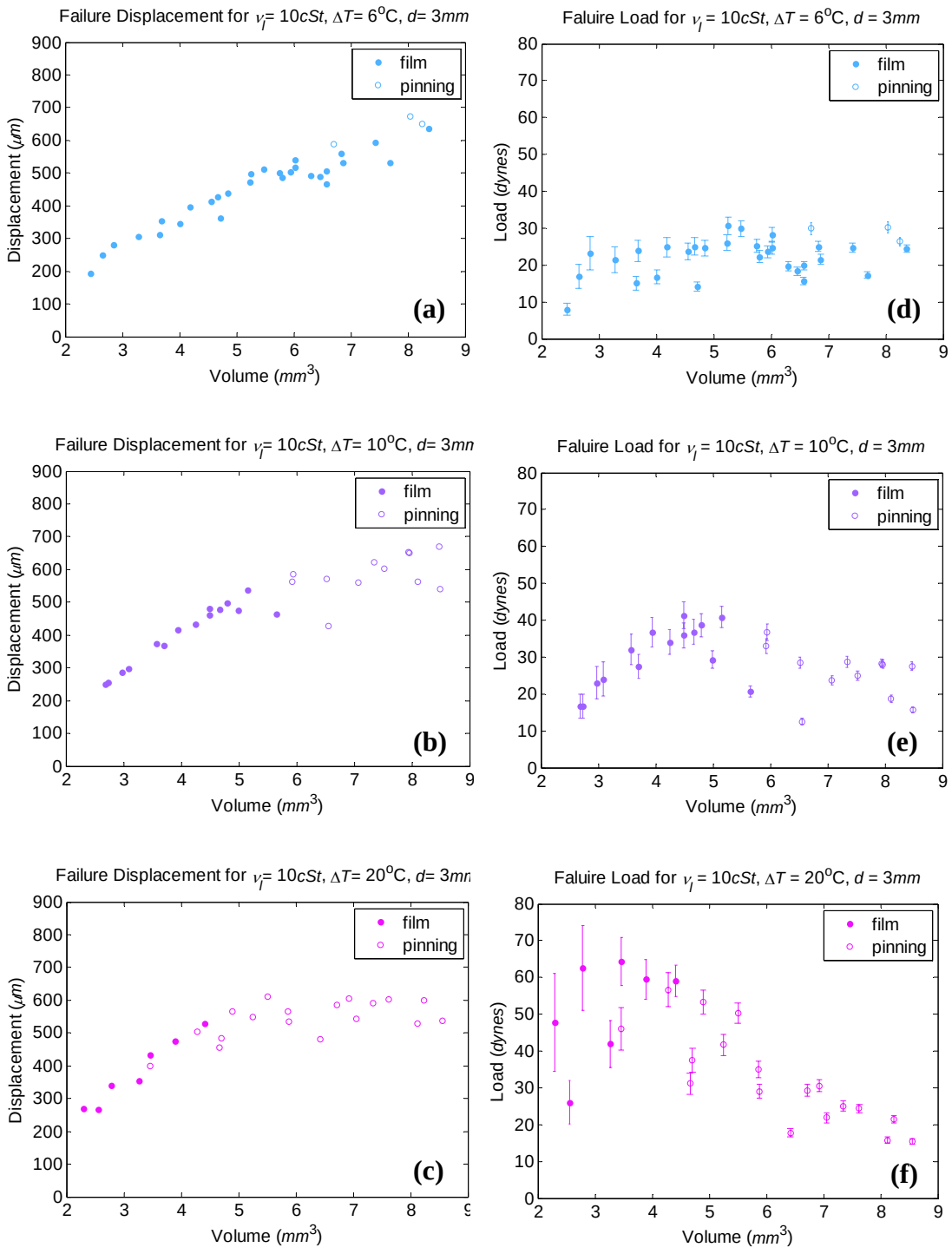


Figure 40. (a)-(c) Failure displacement of nonwetting, silicone oil droplets of ν_l = 10 *cSt* on a *d* = 3 *mm* disk. They correspond to the temperature differences at ΔT = 6, 10, and 20 °C, respectively. (d)-(f) Corresponding failure load. The results are for sessile droplets.

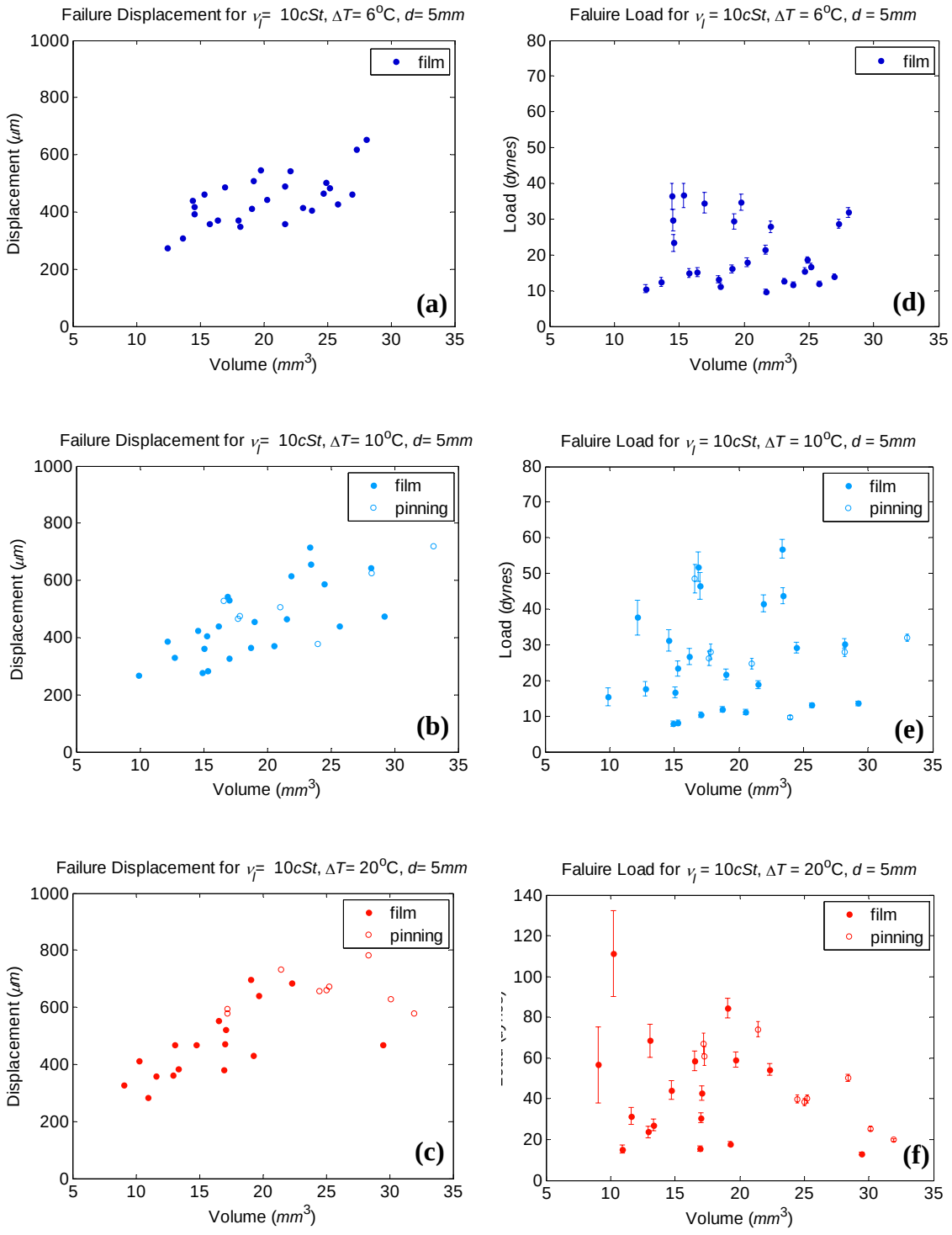


Figure 41. (a)-(c) Failure displacement of nonwetting, silicone oil droplets of ν_l = 10 *cSt* on a *d* = 5 *mm* disk. They correspond to the temperature differences at ΔT = 6, 10, and 20 °C, respectively. (d)-(f) Corresponding failure load. The results are for sessile droplets.

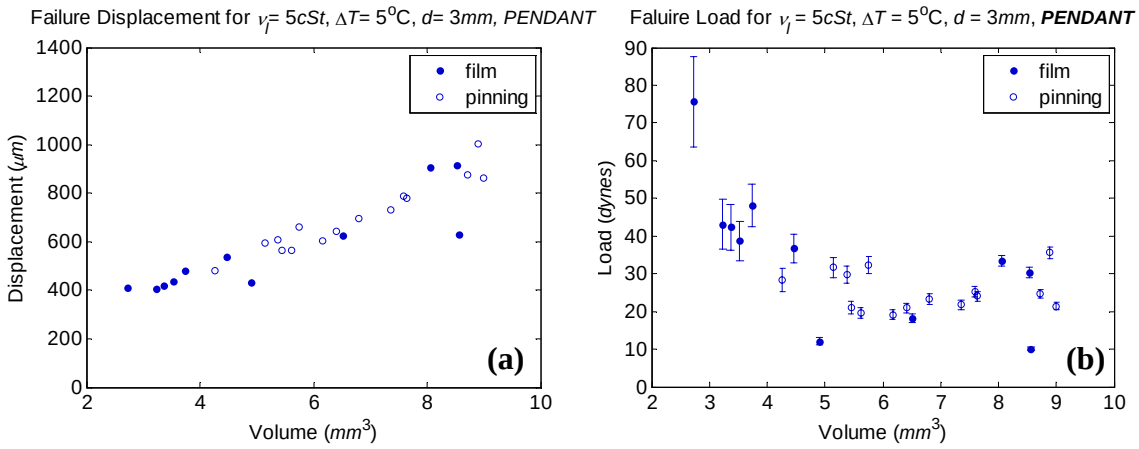


Figure 42. (a) Failure displacement of nonwetting, silicone oil droplets of ν_l = 5 *cSt* on a *d* = 3 *mm* disk. The temperature difference is at ΔT = 5 °C. (b) Corresponding failure load. The results are for *pendant* droplets.

In each experiment, the time interval between the relative displacements was adjusted manually depending on the system of interest. In early stages of the displacement, for example, the time interval can be kept short, since the applied load on a droplet is low and the system is not expected to fail (unless some dust particles are present on the glass surface). After ~100 μm displacement, the time interval is reduced to roughly the twice the viscous time scale of a system, defined as

$$t_\nu \sim \frac{R_0^2}{\nu_l}. \qquad (25)$$

Here, R_0 is the radius of the disk, and ν_l is the dynamic viscosity of the liquid. For the systems of our interest, t_ν = 0.45 and 0.225 *s* for 5 and 10 *cSt* oils on a 3 *mm* disk, respectively and t_ν = 0.625 *s* for 10 *cSt* oil on a 5 *mm* disk.

The data presented in Figure 39 to 41, especially the failure load, exhibit a large scatter. For example, two separate measurements of failure loads yield 20 and 38 *dynes* for a droplet with $\mathscr{V} \sim 4\ mm^3$ for the case of ν_l = 5 *cSt*, ΔT = 20 °C, *d* = 3 *mm* (Figure 39(f)). The error is roughly 100%. Although the uncertainty analysis expects a large error in the load, especially for smaller droplets, the scatter does not seem to be systematic.

Originally, air currents from the laboratory HVAC systems and dust particles on the glass were considered to be responsible for such scatter in the data. For example, occasional bursts of air from the laboratory's ventilation system have been noted. Such perturbations, if large enough, can trigger failures at relatively early stages of the displacement. Also, unfiltered air naturally contains a large number of dust particles that can settle on the glass surface even after it has been cleaned before each experimental run. These particles, if larger than the thickness of the film, can act as obstacles for a nonwetting system, bridging the gap between liquid and solid surfaces as the contact area increases with load applications.

In order to minimize these effects, a large plastic box was manufactured and placed on the vibration-isolation table, encasing all of the necessary instruments inside it. The box is equipped with a HEPA filter with a pore size of 0.2 μm. Just prior to the experiment, a vacuum cleaner is used to move the dusty air out of the box, while clean air is brought into the box though the HEPA filter. Although these modifications have been implemented, no improvements could be detected in the data.

The following arguments on failures of a nonwetting system are based on physical considerations, numerous simulations, and multitudes of experimental observations that the author has noted throughout the course of the research. Here, the author's intention is to qualitatively describe these characteristics, rather than to quantify them. The analysis described herein is aimed at guiding the design of a load-bearing system which uses a permanent nonwetting droplet.

Two failure mechanisms, namely film and pinning failures, are treated separately since different physics are considered to be involved. It will be argued that film failure is triggered by instability of the film- or the free-surface flow, whereas pinning failure is initiated by conditions at the pinning contact line.

3.5. Film Failure

The temperature difference ΔT imposed between a droplet and a plate in a nonwetting system is the driving mechanism of a thermocapillary-nonwetting system. Due to thermocapillarity, thermal-Marangoni convection is generated by application of ΔT on the droplet, dragging the surrounding air into the contact region between the droplet and solid surfaces, and lubricating the interface. As higher ΔT is imposed, the free-surface is set into more vigorous motion, creating a thicker lubricating film with a higher average velocity. Monti, *et al.* (1998) have shown the thickening of the film in their experiments, and interferometric observations from the present study also confirm changes in the film thickness with variations in ΔT.

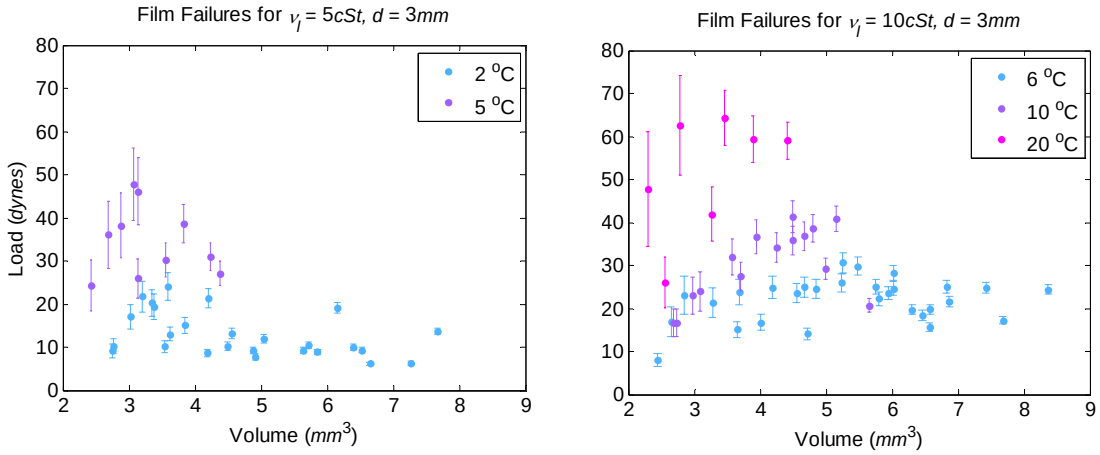


Figure 43. Film failure loadings for (a) 5 *cSt* and; (b) 10 *cSt* silicone droplets at various ΔT. The diameter of the disk is 3 *mm* for both cases. There is a tendency for the failure load to increase with the temperature, indicating the stability of the film at higher ΔT.

Experimental results of film failure show that a larger load can be carried by a system at larger values of ΔT. This trend is clearly seen in the film-failure data for 5 and 10 *cSt* oils on a 3 *mm* disk, presented in Figure 43(a) and (b), respectively. These results suggest that stability of the lubricating film also increases with ΔT. Disturbances that lead to film failure in a system with low ΔT do not trigger the same failure in a system with high ΔT.

The thermal-Marangoni velocity scale ($U_s \sim \gamma \Delta T / \mu_l$) is useful for estimating the free-surface speed of a droplet. As stated (and observed in experiments), the free-surface speed is faster when higher ΔT is imposed on a system for a given liquid viscosity. Therefore, it can be deduced that the lubricating film becomes more stable with faster speed on the surface of a nonwetting droplet. This argument is also confirmed by comparing failure loads between liquids of two viscosities at almost the same temperature difference, namely the systems with ν_l = 5 *cSt* at ΔT = 5 °C and ν_l = 10 *cSt* at ΔT = 6 °C, as shown in Figure 44. Assuming that the temperature coefficient of surface tension is the same ($\gamma = 6.9 \times 10^{-5}$ *kg*/*K*/s^2) between the two liquids, the free-surface speed is expected to be faster on the 5 *cSt* oil droplet (U_s ~ 7.5 *cm*/*s*) than 10 *cSt* one (U_s ~ 4.4 *cm*/*s*). The significantly higher load carried by the 5 *cSt* oil droplet (at slightly lower ΔT than 10 *cSt* oil) suggests the increased stability due to increased speed of the free-surface.

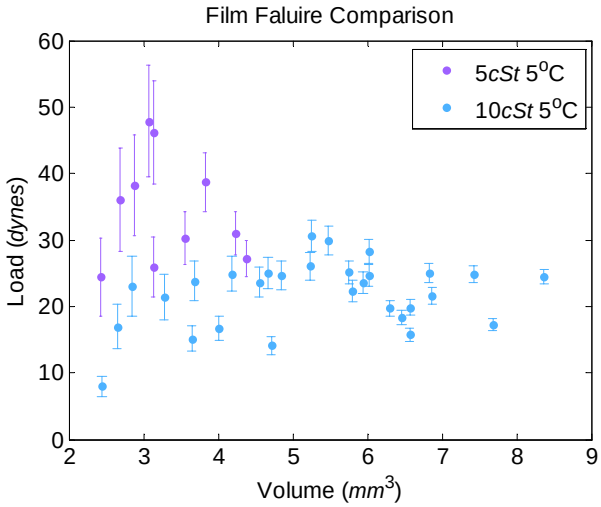


Figure 44. Comparison of the film-failure loading between 5 and 10 *cSt* liquids at ΔT = 5 and 6 °C. Higher load carried by 5 *cSt* oil at lower ΔT values indicate more stable film flow due to faster speed induced on the free surface.

Another indication of the increased stability of the film due to an elevated ΔT can be inferred from the reduced instances of film failure. The experimental result shows that film failure takes place over a wide range of the droplet volume when ΔT is small. As ΔT is increased, film failure is observed only in smaller (and stiffer) droplets, and pinning

failure becomes prevalent in large (and soft) droplets. When sufficiently high ΔT is imposed, *e.g.*, ΔT = 20 °C for the case of less viscous 5 *cSt* oil, all of the reported failure is due to pinning.

3.5.1. Shear Rate as a Film-Failure Criterion

As discussed in the previous section, the characteristic speed of the free surface may be a relevant parameter for predicting film failure. In addition, due to the shearing motion within the contact region and the large shear-rate associated with it, the film thickness is also considered a relevant parameter of failure. The next section will discuss scaling arguments employed to estimate the shear rate from the available experimental data and output from Surface Evolver.

The shear rate of the lubricating film is estimated from surface-velocity U_θ divided by the average film thickness δ

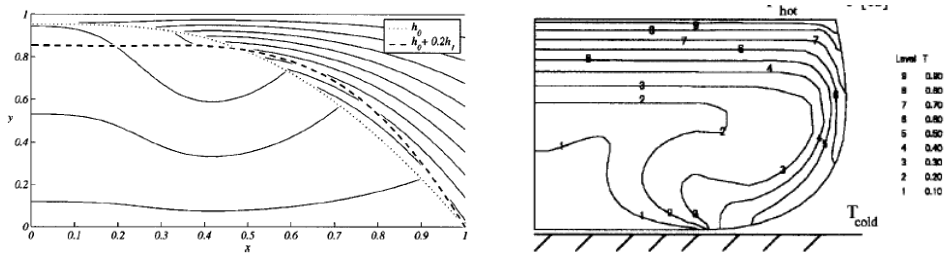
$$\text{shear rate} = \frac{U_\theta}{\delta} \tag{26}$$

The estimate for the free-surface velocity U_θ developed in this section is slightly different from the conventional thermal-Marangoni velocity scale discussed so far, since it takes the volume of the droplet into an account.

In order to develop the estimate for U_θ, the tangential-stress balance is applied along the liquid-gas interface, as is done for the thermal-Marangoni velocity scale; the only difference being that it is applied specifically at the outside of the contact region. In this region, the gradient of the shear stress is considered to balance with the shear stress in the liquid phase

$$\nabla_s \sigma \sim \tau_l \,. \tag{27}$$

As seen from the computed isotherms from Sumner, *et al.* (2003) and Monti & Savino (1996) in Figure 45(a) and (b), the magnitude of the temperature gradient is larger in the axial direction than in the radial direction on a nonwetting droplet.



(a) (b)

Figure 45. Isotherms computed from numerical analysis. The temperature gradient is predominantly directed along the axial direction of the droplet. (a) and (b) are the computations extracted from Sumner, *et al.*, (2003) and Monti, *et al.*, (1996).

Using this fact, the gradient of the surface tension is scaled by

$$\nabla_s \sigma \sim \frac{\gamma \Delta T}{H}, \tag{28}$$

where γ is temperature coefficient of surface-tension force, ΔT is the temperature difference, H is the height of a "squeezed" droplet. The shear stress within the liquid is scaled by

$$\tau_l \sim \mu_l \frac{U_\theta}{R_0}, \tag{29}$$

with μ_l as the viscosity of the liquid, U_θ as the velocity scale, and R_0 as the radius of the disk. From the balance between equations (28) and (29), the velocity estimate is obtained,

$$U_\theta \sim \frac{\gamma \Delta T}{\mu_l} \frac{R_0}{H}. \tag{30}$$

Equation (30) states that the surface velocity increases with the squeezing imparted on the droplet due to an increased temperature gradient in the axial direction. In fact, the increase in the vigor of internal convection has been observed experimentally, as higher squeezing is introduced on the droplet.

The average film thickness δ is derived from the balance between the lubricating film and the capillary pressures within the contact region. Following the discussion from Dell'Aversana & Neitzel (2004), the pressure of the lubricating film P_{lub} can be scaled by

$$P_{\text{lub}} \sim \frac{\mu_g U_\theta}{\delta^2} R_c, \tag{31}$$

where μ_g is the viscosity of the lubricating film, and R_c is the radius of the contact area. This lubricating pressure is responsible for sustaining the capillary pressure of the droplet, which increases with the relative displacement and corresponding curvature of the free surface. The pressure jump across the interface of the deformed, static droplet is given by

$$\Delta P = \sigma\left(\frac{1}{R_a} + \frac{1}{R_c}\right), \tag{32}$$

where R_a and R_c are principal radii of curvature at the edge of the contact region. Based on Surface Evolver results, the values of the radii of curvatures are of same order of magnitude as shown in the diagrams presented in Figure 46. To simplify the present discussion, we assume $R_a \sim R_c$.

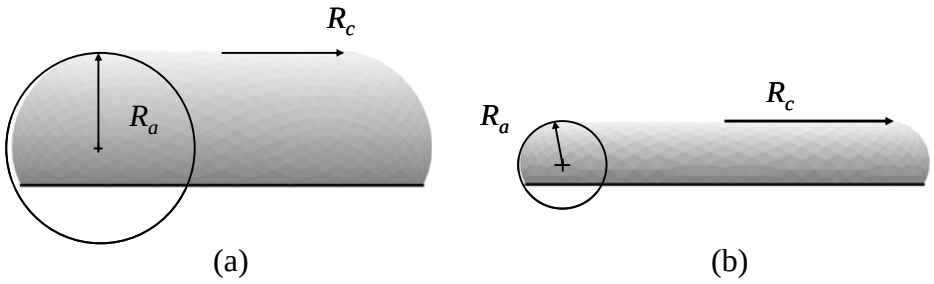


Figure 46. Side views of droplet shapes and estimates of radii of curvatures. These outputs from Surface Evolver show the shapes of squeezed droplets at film failures. (a) and (b) correspond to $\mathscr{V}$= 6.75 and 3.36 mm^3, respectively.

The balance between equations (31) and (32) yields the average film thickness

$$\delta \sim \left(\frac{\mu_g}{\mu_l}\frac{\gamma\Delta T}{\sigma}\frac{R_0}{H}\right)^{1/2} R_c. \tag{33}$$

Equation (33) relates the film thickness to various parameters of a nonwetting system. For example, the film thickens with gas viscosity μ_g due to an increased lubricating pressure as stated in equation (31). A larger ΔT and less viscous liquid also lead to a thicker film due to an increase in the induced free-surface speed. Furthermore, film

thickness is expected to decrease when the surface tension of a droplet is higher since the lubricating film is less effective in deforming the droplet. After rearrangement, the estimate for the shear rate is given by

$$\frac{U_\theta}{\delta} \sim \left(\frac{\gamma \Delta T \sigma R_0}{\mu_l \mu_g H R_c^2} \right)^{1/2} . \qquad (34)$$

The two variables in equation (34), namely the contact radius R_c and the droplet height H, were not obtained experimentally. For the estimate used in the present analysis, Surface Evolver has been employed to evaluate these variables.

The subroutine "slice" from the downloaded Surface Evolver package was implemented to evaluate the contact radius R_c. The algorithm can compute the circumference of a circle, made by intersecting a virtual plane placed 10 μm below top of the droplet and parallel to a nonwetting plane, as a function of displacement. The result from the computation is shown in Figure 47 for droplets with the fluid properties of 5 *cSt* silicone oil on the 3 *mm* disk. The interpolation scheme developed for the load computation has been imported for the determination of the contact radii at the point of failure.

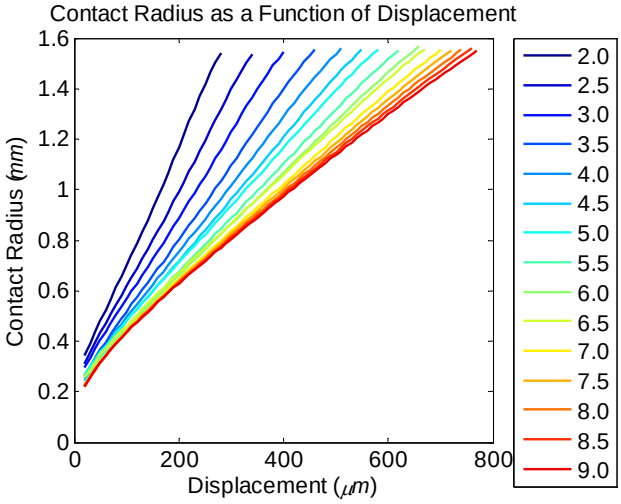


Figure 47. Contact radius as a function of displacement computed from Surface Evolver. The radius is evaluated at 10 μm below the nonwetting plane (or the top of the flattened droplet). The legends are the sizes of the volume in mm^3.

The height of a squeezed droplet, H, appearing in equation (34) is obtained by subtracting the failure displacement $\mathscr{D}$ from the undisturbed droplet height H_0 computed from Surface Evolver,

$$H = H_0 - \mathscr{D} \,. \tag{35}$$

Figure 48 plots H_0 as a function of the volume of various droplets, such as sessile (S) and pendant (P) droplets on the 3 *mm* disk support. No significant difference was observed between the initial heights of 5 and 10 *cSt* droplets, because the surface tensions of these liquids are nearly identical (σ = 19.7 and 20.1 *dynes/cm*).

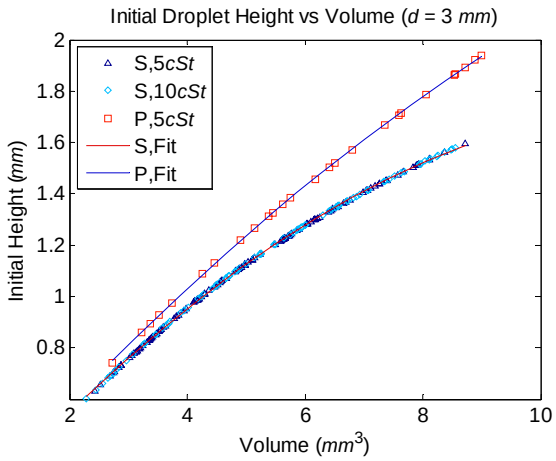


Figure 48. Initial heights of droplet on *d* = 3 *mm*. "S" and "P" are used to indicate sessile and pendant droplets, respectively, in the legend provided in (a).

Quadratic fits of H_0 for various systems are:

(1) ν_l = 5 and 10 *cSt*, *d* = 3 *mm*, (S) Sessile droplet

$$H_0 = -0.01044\mathscr{V}^2 + 0.2672\mathscr{V} + 0.05138 \tag{36}$$

R-squared = 0.99.

(2) ν_l = 5 *cSt*, *d* = 3 *mm*, (P) Pendant droplet

$$H_0 = -0.06317\mathscr{V}^2 + 0.263\mathscr{V} + 0.07848 \tag{37}$$

R-squared = 0.99.

In equations (36) and (37), the units for H_0 and $\mathscr{V}$ are *mm* and mm^3, respectively.

The shear rates of different systems are presented in Figure 49. The legend in the graph indicates sessile (S) and pendant (P) droplets, along with the viscosity and the temperature differences. The plot shows a similarity between the systems for the following cases:

1. S, ν_l = 5 *cSt* at ΔT = 2 °C and S, ν_l = 10 *cSt* at ΔT = 6 °C

2. S & P, ν_l = 5 *cSt* at ΔT = 5 °C, and S, ν_l = 10 *cSt* at ΔT = 10 °C.

The similarity must arise due to the similar characteristic speeds induced on the free surface of a droplet.

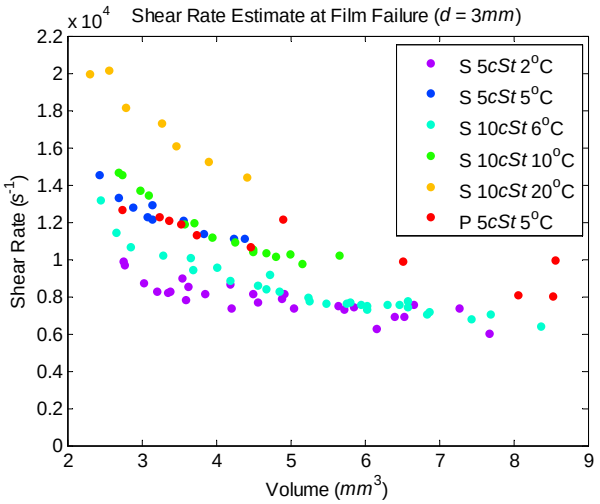


Figure 49. Shear rate corresponding to film and pinning failures for various similar systems with *d* = 3 *mm*. S and P are used to denote sessile and pendant droplet systems, respectively.

As can be inferred from the estimate from the expression of shear rate (equation (34)), the volume, and thus the height of a droplet, has a primary influence on the shear rate for a given viscosity and ΔT. That is to say, the shear rate should decrease with an increase in the droplet volume since its (undeformed) height is bigger, as indicated by the $H^{-1/2}$ dependency in equation (34). Also associated with the bigger droplet is the retarded surface speed (equation (30)) and the thinner average film thickness (equation(31)), both of which may destabilize the flow of the lubricating film.

The hydrodynamic stability of shear flows is a subject that has been studied extensively (Drazin & Reid (2004)), and no simple explanation appears to describe the stability of the lubricating film flow that exists in the permanent nonwetting system. Further theoretical and numerical analyses of the hydrodynamic stability will be useful in gaining a better understanding of the stability of the permanent nonwetting system, but are beyond the scope of the present thesis.

3.5.2. Onset of Film Instability

Once a droplet touches a solid surface, the wetting propagates across the contact regions in a matter of few milliseconds. A high-speed sequence of the event has been documented by Dell'Aversana & Neitzel (2004), showing the initiation of the wetting process at a location on the periphery of the contact region, where the film thickness is smallest. Due to the short time scale associated with the wetting event, a normal frame-rate camera is not suited for recording the process.

Experimental observations have revealed the slow growth-process of a non-axisymmetric disturbance on the free-surface of the droplet as some threshold compression is introduced on a system, leading to instability of the nonwetting system just prior to the wetting event. The sequence of the process, captured by a regular frame-rate camera (at 30 fps), is presented in Figure 50. This process follows from a stable system configuration, where the droplet is highly deformed with an uneven film thickness around the contact region. The slight variation of the film thickness can be seen as the changes in the fringe pattern around the periphery of the dimpled interface, as can be seen in the Figure 50(a) at the onset of instability ($t = 0\ s$). From a simple inspection, there are 4 cycles in the fringe pattern (one cycle is black-white-black) around the periphery of the dimple, counting from the top-right to the bottom-left corners. This cycle corresponds to the height variation of ~ 1.3 μm. Between Figure 50(a) and (b), the region of the dark-fringe at top-right corner enlarges, propagating in the azimuthal-direction along the edge of the circular interference pattern. The disturbance grows further along the azimuthal direction from Figure 50(b) to (c), while the film thickness on the bottom-left corner of the dimple stays the same.

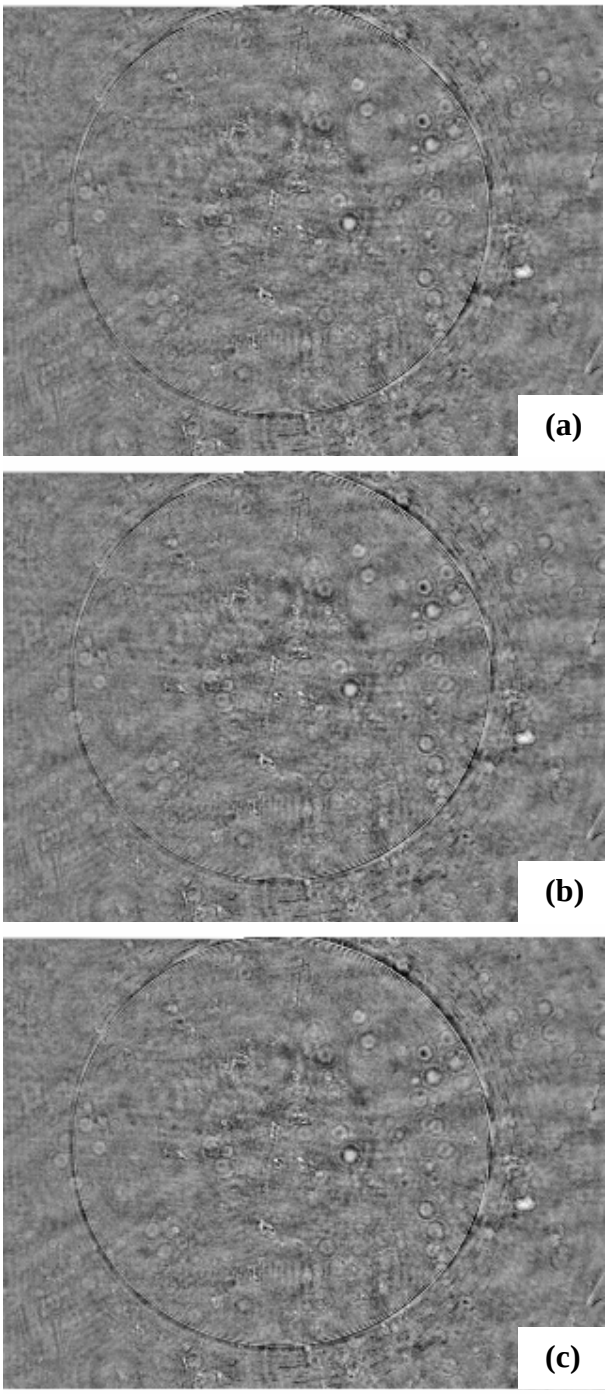
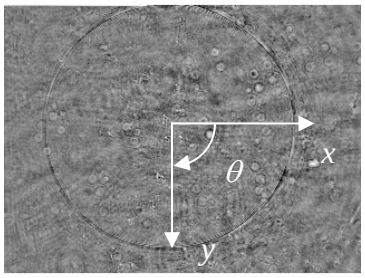
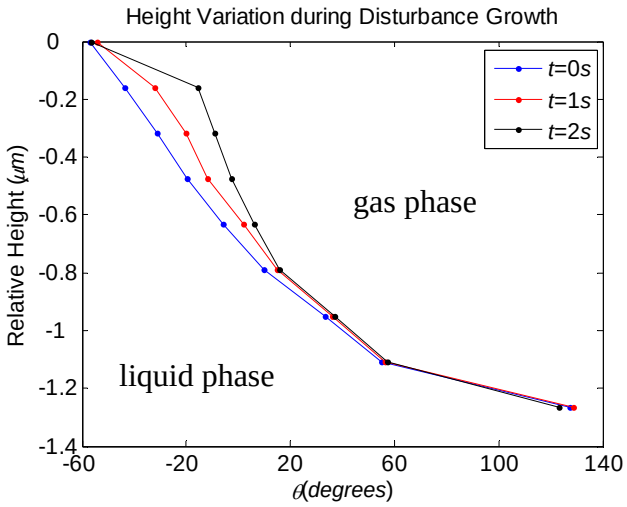


Figure 50. (a)-(c) Growth of disturbance visualized from fringe patterns. (a)-(b) Disturbance starts to grow at top right corner of an uneven film, reducing the film thickness locally. (b)-(c) Propagation of disturbance into azimuthal direction. After the image in (c) wetting takes place. The wetting event cannot be resolved by the regular frame camera used for this recording. Time interval between each frame is 1 *s*.

In order to illustrate the argument above, a fringe-counting technique has been employed, plotting the relative locations of the liquid-gas interface from the image sequence presented in Figure 50. In this technique, pixel coordinates of black and white fringes are tagged along the periphery of the dimpled interface, starting from a reference height (= 0 μm) at the top right corner ($\theta \approx -60^{o}$) to the lower-left corner of the dimpled interface ($\theta \approx 120^{o}$) (refer to Figure 51(a) for coordinate system used for the analysis). Since changes in the fringe color (from white-to-black) correspond to ¼ of the wavelength of the laser (λ = 632.8 *nm*), the relative changes in the height of the interface can be evaluated. The result is presented in Figure 51(b), showing the azimuthal variations of the height of the liquid-gas interface (along the periphery of the dimple) at various times. The plot clearly shows the propagation of the disturbance, indicated by the displacement of the liquid-gas interface in the vicinity of the source of the disturbance, from t = 0 to 2 *s*.



(a)



(b)

Figure 51. (a) Coordinate system used for the analysis of the disturbance growth. (b) Temporal changes in the interface positions as a function of time. The wave propagates in azimuthal direction, along the periphery of the dimpled interface.

It is noted here that the sign of the interstitial shape cannot be determined from these images. As a result, the slope of the liquid-gas interface may be positive, thus its height increases in the azimuthal direction. It requires a highly resolved fringe pattern from the center to the edge of the dimple on the free surface, or other techniques such as

angle- and phase-shifting, in order to determine the absolute sign of the interface. However, the description above will be equally valid for characterizing the growth rate and the direction of the disturbance propagation. The fringe-counting technique clearly captures the growth process by quantitatively assigning the relative height variation around the contact region as a function of time.

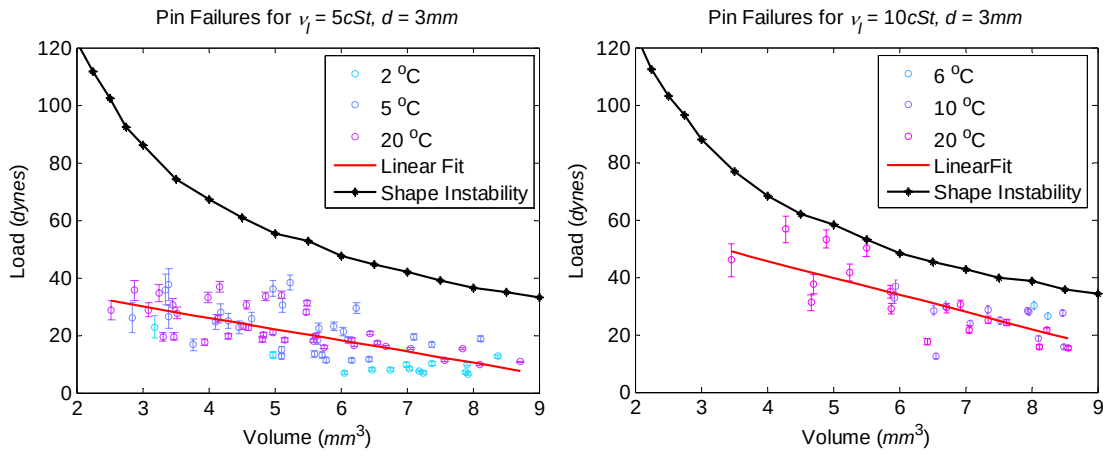
3.5.3. Other Remarks on Film Failure

As discussed in the previous sections, the nonwetting system is capable of supporting a higher load with increasing ΔT. Therefore, it is desired that the imposed temperature be high when designing load-bearing systems using thermocapillary nonwetting droplets. The temperature differences in the present work have been kept below 20 °C, while maintaining the mean temperature at room temperature (25 °C). Using this setup, it has been noted that temperature differences larger than 20 °C result in the condensation of water vapor (contained air) on the surface of the glass, which may affect the loading characteristics of a nonwetting droplet. The effect of water vapor on the loading characteristics has not been explored in the present thesis.

In addition, minor evaporation has been observed from 5 *cSt* silicone oil at $\Delta T = 20$ °C ($T_H = 35$ °C). Interferometric observations show a condensate film developing on the glass with the thickness of $O(100\ nm)$ in the vicinity of contact region during the course of an experiment. Although such evaporative volume-loss is miniscule, the system would require the liquid to be replenished more often than would be the case with a less volatile droplet, such as 10 *cSt* silicone oil. (In fact, the less viscous the silicone oil, the more volatile it is). As noted for the water-vapor condensation, the effect of the condensation (from the droplet) on the loading characteristics is not well understood. It is suspected, however, that the effect is negligibly small due to the very thin nature of the condensate films.

3.6. Pinning Failure

As the film flow becomes more stable with increased vigor of the surface motion due to an increase in ΔT, a nonwetting droplet can be squeezed further against a glass plate, carrying a higher load. Eventually, a droplet can be squeezed until its pinning contact-line fails. This is defined as pinning failure in the present study.



(a) (b)

Figure 52. Pinning-failure load for (a) 5 and; (b) 10 *cSt* silicone-oil droplets at various ΔT. The diameter of the disk is 3 *mm* for both cases. Experimental load data is compared to the load at the onset of shape instability obtained from Surface Evolver.

The failure loads corresponding to pinning failure are presented in Figure 52(a) and (b) for sessile droplets of 5 and 10 *cSt* silicone oils, respectively, on the 3 *mm* pedestal. Straight lines are used to fit through the data. The first fit

$$F_{5cSt} = -3.923\mathscr{V} + 41.8, \qquad (38)$$

has been obtained for the results of 5 *cSt* oil, where the units are given in *dynes* and mm^3 for the load F and the volume $\mathscr{V}$, respectively. Due to the scattered nature of the data, the R-squared value for the fit remained low at 0.4762. The second fit, obtained for the 10 *cSt* failure data, is

$$F_{10cSt} = -5.924\mathscr{V} + 69.46, \qquad (39)$$

with an R-squared value of 0.5725. These failure data are compared with the load at the onset of shape instability obtained from the Surface Evolver analysis, indicated as "Shape

Instability" in the legend. Generally, the pinning-failure load always stays below the load at the onset of shape instability obtained from Surface Evolver. As mentioned earlier, this is likely due to the imperfect alignment between the surfaces of the pedestal and the glass, uneven film thickness in the contact region resulting in uneven pressure distribution, and the imperfect, pinning boundary-conditions in an actual experimental system.

The experimental data and Surface Evolver computations exhibit a trend, with the pinning-failure load decreasing with the volume of a droplet. Such a trend can be seen clearly in the case of $\nu_l = 10\ cSt$ and $\Delta T = 20$ °C, as shown in Figure 52(b). In general, the failure load from the experiment does not exceed that associated with the onset of shape instability from computations. Several factors must contribute to this trend, one including the pressure at the edge of the pedestal, to which the droplet's contact line is pinned. From the point of view of hydrostatics, the pressure at the pinning edge is proportional to the height, and thus, the volume of a droplet. Therefore the hydrostatic pressure at the disk edge is larger for the bigger droplets, "pushing" the liquid off to the side, requiring contact angles to balance the force. Another factor may be due to the stiffness of the liquid, which was mentioned earlier along with the shape instability (Section 3.3.3) and its analogy to the buckling process. As shown in Figure 32(b), a shallower and stiffer droplet can sustain a higher load than a larger one before succumbing to shape instability, which results in a net force at the contact line due to asymmetry of the droplet shape, pressing the droplet laterally to one side. On top of that, a smaller droplet must overcome a larger change in the pinning contact angle than the bigger droplets before it makes a certain angle with the pedestal and the contact line gets de-pinned.

As opposed to film failure, pinning failure is less sensitive to changes in ΔT. This can be seen in the intermingled results for different ΔT presented in Figure 52. Surface Evolver has been employed for computing the pinning angles at failure for the 5 *cSt* case and the results are presented in Figure 53. A linear function has been employed to fit the data, showing the relationship for the failure pinning angle θ_p (degrees)

$$\theta_p = 3.705\mathscr{V} + 89.06, \qquad (40)$$

with volume $\mathscr{V}$ in the unit of mm^3. The fit has R-squared value of 0.1282. When compared with the average pinning contact-angle of 176° at the onset of shape instability, the experimental values always fall well below it due to the real-world factors as indicated earlier (*i.e.*, the imperfect alignment, uneven film thickness, and boundary conditions).

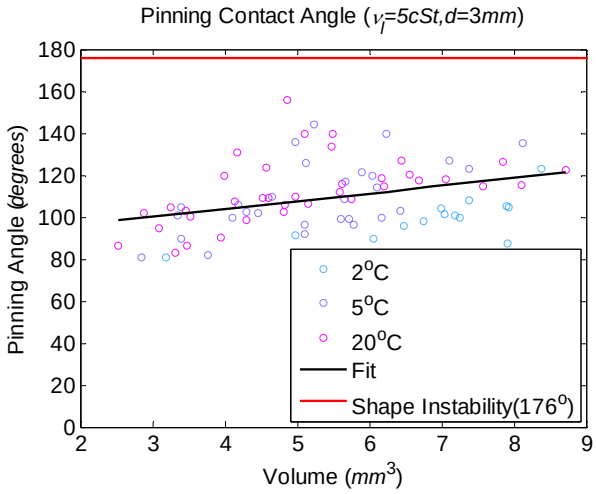


Figure 53. Pinning contact angles computed from Surface Evolver at failure displacement. The contact angle is small when the temperature difference is also small. The results are compared to the values at the onset of shape instability obtained from Surface Evolver.

An exception seems to be the relatively smaller load obtained for the case of ν_l = 5 *cSt* at ΔT = 2 °C, as compared with that obtained for the same liquid at a higher ΔT (= 5 and 20 °C). The lower load implies that less deformation is induced in the droplet, resulting in a smaller contact angle at the pinning contact line. Higher pinning angles are generally obtained for the systems at ΔT = 5 and 20 °C than for the system at ΔT = 2 °C. The high (low) values in pinning angles with an increase (decrease) in ΔT may be due to variations of the pinning angle and the mobility of the contact line due to the changes in the strength of thermocapillary convection. For example, the numerical studies from Benintendi & Smith (1999) and Smith (1995) show that the **contact angle** of a droplet **on a horizontal plate** decreases with an increased heat input from below, pumping more liquids towards the apex of the droplet as the strength of thermocapillary

convection is strengthened. Using this analogy, the **pinning angle** of a nonwetting droplet may decrease due to the similar pumping effect associated with an increase in the heat input from the pedestal. As a result of the reduced pinning angle, the warmer droplet (at higher ΔT) may be squeezed further into the glass, compared to a less warm droplet with a larger pinning angle.

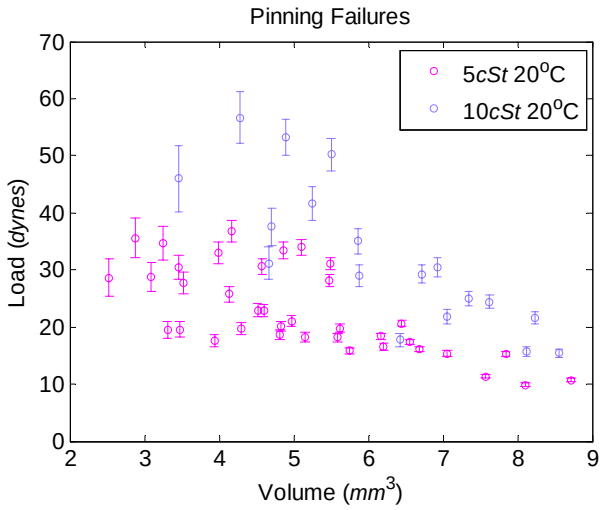


Figure 54. Comparison of pinning-failure loadings between two systems at ΔT = 20 °C. Given the tendency, where higher load is sustained by 10 *cSt* silicone oils, a dynamically similar system seems impossible between 5 *cSt* at ΔT = 20 °C and 10 *cSt* at ΔT = 40 °C.

In addition, pinning-failure load is higher in a more viscous liquid. The comparison of the failure load between 5 and 10 *cSt* oil systems, driven at the same temperature difference (ΔT = 20 °C), is presented in Figure 54. The failure load of the more-viscous oil lies above that of the less-viscous oil. Such behavior may be associated with the greater work required to overcome a viscous resistance in order to move the liquid sideways. An order-of-magnitude estimate for the incremental work required to move a droplet by an infinitesimal distance δx to a side is given by

$$\delta W \sim \mu_l \frac{U_d}{H} R_0^2 \delta x \qquad (41)$$

where U_d is an instantaneous, bulk speed of the droplet in translation, H is the height of the droplet, and R_0 is the radius of the disk. The result suggests that the required work increases with the viscosity of liquid and is inversely proportional to the height of a

droplet. The formulation in (41) may also explain the higher failure-load sustained by the smaller droplets, as indicated by H^{-1} dependency.

As with film failure, pinning failure data are also scattered. It is likely that the scattered nature of failure is associated with the variations of boundary conditions around the edge of a disk. The dependency of pinning failure on the boundary condition is confirmed through a personal communication with Dell'Aversana; the pinning characteristic improves by using disk with a sharper edge. Mathematically speaking, the radius of curvature becomes very small as the edge of the disk is sharpened, approaching the shape of a perfect wedge. A finite displacement of the contact line at the sharpened edge of the disk must accompany a large change in the contact angle, making it difficult for a droplet to move (as opposed to on a rounded edge). In the present studies, the variation of the boundary conditions between each experiment is unavoidable. For example, it may arise due to applications of an anti-wetting agent used to prevent a droplet from spilling at early stages of loading; an uneven application of the coating can lead to nonuniform distribution of surface energy around the perimeter of the disk and, of course, different effectiveness between experimental runs. In addition, differences in the boundary condition may arise due to dust deposited by a cotton swab, which has been used to clean the disk surface, resulting in variations of the surface roughness around the disk. A relevant analysis by de Gennes (1985) discusses the effects of chemical contamination and local roughness on dynamics of the contact line.

3.7. Use of a Larger Disk

A set of experiments has been carried out for droplets deposited on a larger disk (d = 5 *mm*) using 10 *cSt* silicone oil. Although larger loads could be carried by the droplet on a larger disk in several instances, the data are scattered more than the data for droplets on a 3 *mm* disk, making it harder to describe the failure characteristics. Such large scatter in the data could be attributed to the droplet's susceptibility to specific disturbances present in the experimental apparatus due to the increased free-surface area.

Various types of noise are transmitted from the environment to the vibration-isolation table used for the experiment. In fact, noticeable vibration could be detected on

the free-surface of a droplet on the larger disk, whereas it was not noticed on a droplet deposited on the smaller one. The vibration is detected by interferometry. The temporal variation of the pixel intensity at the edge of the dimpled interface is plotted in Figure 55. The maximum change in the pixel intensity is roughly 12 out of 256 gray-scale units, corresponding to the amplitude of ~ 8 *nm* on the free surface. By visual inspection, the frequency of the free-surface is of $O(10\ Hz)$

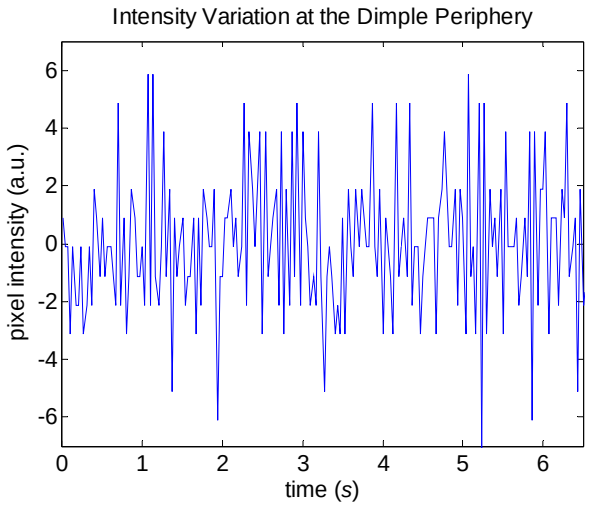


Figure 55. Temporal variation of pixel intensity at the periphery of the dimple on a droplet. The data is taken from a 10 *cSt* droplet on a 5 *mm* disk.

Although various attempts were made, vibration could not be eliminated for the droplets on the 5 *mm* disk. Such vibration is considered to be a byproduct of reduced capillary-effect in the system having a larger disk base and free-surface area, and the droplet's characteristic frequency near that of the environmental noise. Because the characteristic frequency of a pinned droplet decreases with the increase in the free-surface area (and the decrease in capillary pressure) of the droplet, the low-frequency excitation at $f = O(10\ Hz)$ is more likely to resonate with the droplets on the 5 *mm* disk.

An experiment was carried out to determine the (1^{st} mode) characteristic frequency of isothermal, pinned droplets, for the case of $\nu_l = 1\ cSt$. It is expected that the dynamic response of the isothermal system is minimally affected by the presence of thermocapillary convection and squeezing introduced on the droplet. In order to measure the characteristic frequency, the droplets were oscillated near resonance, which is determined by observing high-amplitude response on the free surface of a droplet excited

by external forcing. The decaying motion of the liquid-gas interface was tracked by high speed camera after the cessation of the forcing, and the data points were fitted with a linearly decaying function,

$$H(t) = H_0 + Ae^{-bt}\cos(\omega t + \phi). \qquad (42)$$

In equation (42), $H(t)$ is the height of the droplet recorded by the camera, H_0 is the DC off-set of the oscillation, A is the amplitude, b is the damping rate, ω is the circular frequency ($\omega = 2\pi f$), and ϕ is the phase angle. The result of the characteristic frequency ω is nondimensionalized by capillary time-scale ($t_{cap} = \sqrt{\rho_l R_0^3/\sigma}$), is plotted against the volume parameter ($\mathcal{V}/R_0^3$) in Figure 56. As seen in this figure, the characteristic frequency decreases with the increase in the surface area of the droplet, which results either from an increase in the droplet size (for a given disk diameter) or by using larger disks. For example, the dimensional frequency falls within the range of f = 50 ~ 100 *Hz* for droplets on d = 3 *mm*, whereas it falls within f = 30 ~ 45 *Hz* for the ones on d = 5 *mm*. Considering the potential application of the permanent nonwetting system within microgravity environments, such as encountered in the International Space Station with the presence of *g*-jitters in the forcing frequency-range of *O*(0.1-100 *Hz*), the use of smaller droplets and smaller disks prevent the resonance.

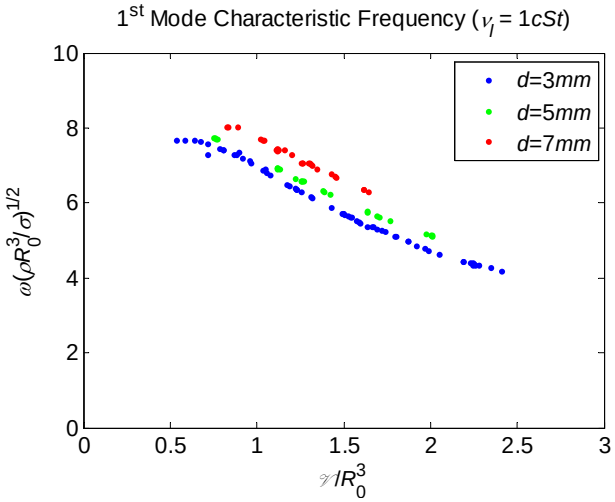


Figure 56. 1st mode characteristic frequency of isothermal, pinned droplet on a disk of different diameters. The frequency decreases with the increase in the surface area, and thus the capillary pressure, which results due to an increase in the volume size.

3.8. Pendant V.S. Sessile Droplets

The shapes of the droplets hanging from the disk are deformed due to gravitational pull. The difference between the shapes of sessile and pendant droplets becomes more evident in larger droplets than in the smaller ones due to the increasing influence from the body force as compared with the capillary effect. As a result of the initial shape difference, a pendant droplet can be squeezed for a larger distance than a sessile droplet if the same volume of liquid is used. The result is evident from the comparison of the failure-displacement data between the pendant and sessile systems as shown in Figure 57(a). On the other hand, the corresponding values of the film- and the pinning-failure load remain within the same range, as shown in Figure 57(b) and (c), since the end result of capillary pressure is similar between these cases.

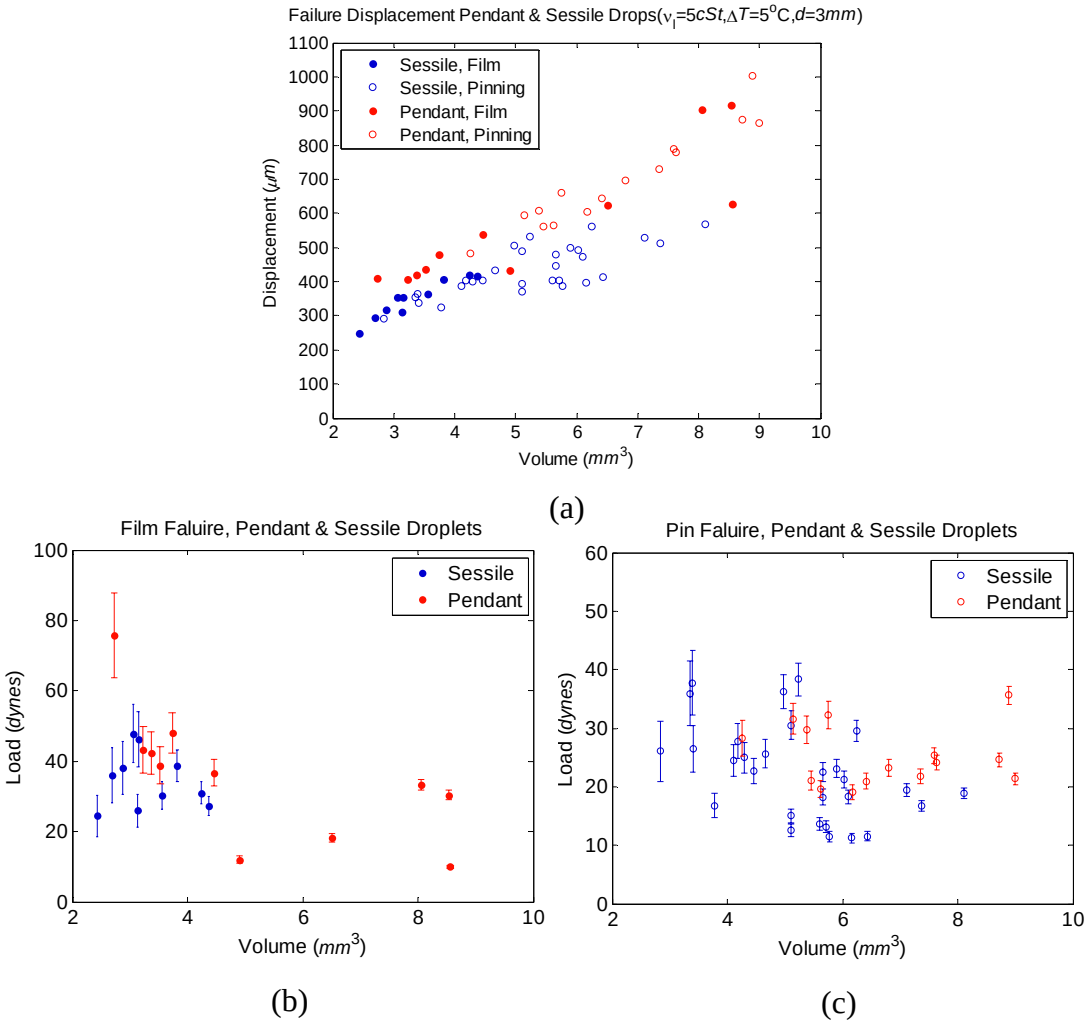


Figure 57. Comparison of (a) failure displacement; (b) film-failure loading and; (c) pin-failure loading between pendant and sessile droplets. The case is for ν_l = 5*cSt*, *d* = 3*mm*, ΔT = 5 °C.

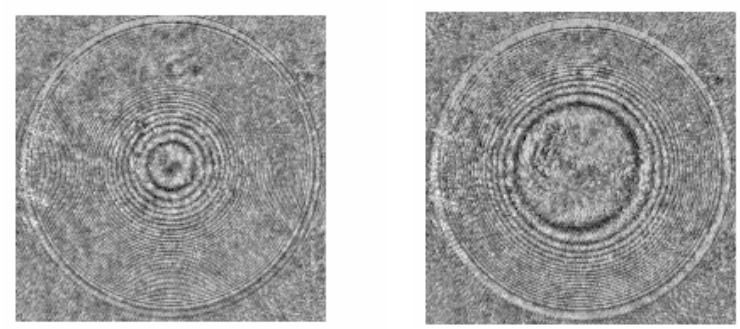
One noticeable difference can be seen as film failures occurring in a larger droplet in the pendant-droplet system. This may be associated with the buoyancy of the liquid affecting the strength of thermocapillary convection in a sessile droplet. In the sessile system, buoyancy-driven convection opposes the thermocapillary convection at the center of a droplet, tending to reduce the surface speed within the contact region, i.e., reducing the vigor with which lubricating gas is dragged into this region. As a result, a sessile droplet may be less able to sustain a load than a pendant one, which is stably stratified by temperature, being heated from above. Because buoyancy, as measured by a local Rayleigh number, increases with the cube of the droplet height, it is likely that the effect

will become more important for a larger sessile droplet. Further analysis is warranted to draw any conclusion about the film stability affected by this buoyancy effects.

3.9. Shape Transition of the Interface

3.9.1. Displacement and Load

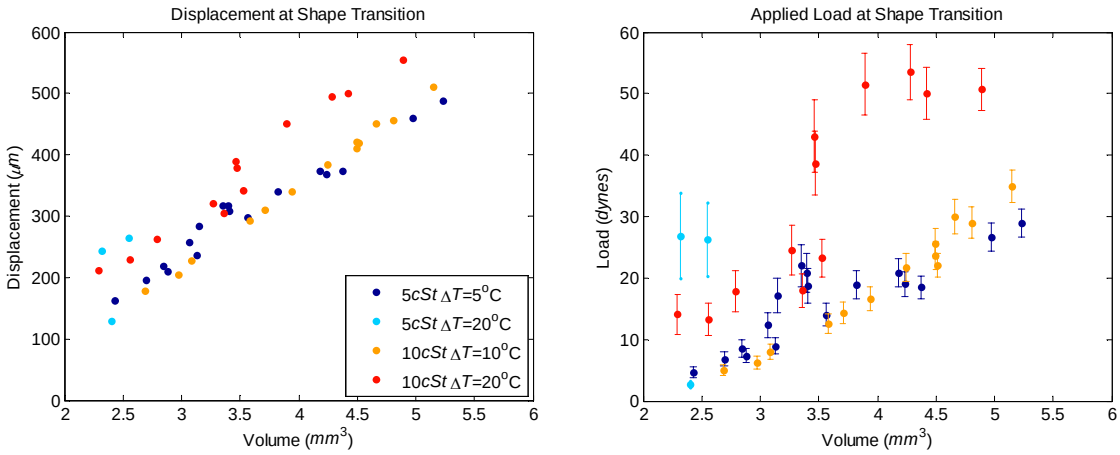
In some instances, the shape of the free-surface has been observed to undergo a sudden change that is not followed by film or pinning failure. From a stability point of view, the growth of the disturbance observed in these situations is bounded or even zero. Such "exchange" of the interfacial structure from one state to the next implies that it is accompanied by a transition of one stable flow field to another stable one. The images, before and after the transition process, are contained in Figure 58(a) and (b), respectively for a shallow droplet. Before the transition process is initiated, the shape of the interface shows the conventional dimpled structure as seen in Figure 58(a). As the process begins, the transition continues autonomously without any application of squeezing to the final stage shown in Figure 58(b), with a flattened region at the center.



(a) (b)

Figure 58. Fringe patterns (a) before and; (b) after the shape transition obtained from a smaller droplet. The transition process takes about 1 *s* to complete.

The relative squeezing and the corresponding load at the onset of the shape transition are presented in Figure 59(a) and (b), respectively, for various configurations of the nonwetting systems. As can be seen from these results, both of the quantities at the onset of instability increase with the droplet size.



(a) (b)

Figure 59. (a) Displacement and; (b) load of shape transition of various nonwetting systems. The legend indicates the viscosity and the temperature difference of the systems in the present analysis.

The Marangoni number may be evaluated at the onset of shape transition, based on the assumption that the transition process is triggered by thermocapillary instability. In this system, the Marangoni number is defined by

$$Ma = \frac{\gamma \Delta T H}{\mu_l \alpha_l}, \qquad (43)$$

where, H is the height of the squeezed droplet and α_l is the thermal diffusivity of the liquid. The result is plotted in Figure 60 as a function of dimensionless volume parameter, defined as $\mathscr{V}/R_0^3$, where R_0 (= 1.5 *mm*) is the radius of the pedestal. The onset of shape transition overlaps around Ma ~ 400 in the two systems with ν_l = 5 *cSt* at ΔT = 5 °C and ν_l = 10 *cSt* at ΔT = 10 °C. A higher value of Marangoni number (~ 600) is obtained in the system at higher ΔT (= 20 °C).

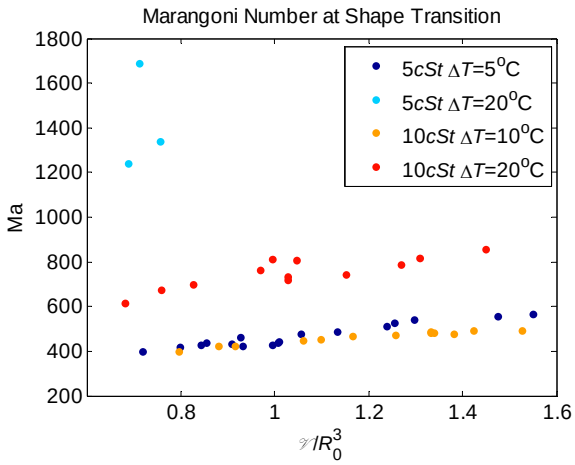


Figure 60. Marangoni number at the onset of shape transition, plotted against a dimensionless volume parameter ($\forall/R_0^3$).

3.9.2. Image Analysis

A transition process has been recorded using a high-speed camera at 125 fps. The image sequence is used to retrieve the details of the transition process, showing the changes in the interstitial shape structure within the region of interest. The entire field of the interference pattern, at the beginning of the transition process, is presented in Figure 61. The spatial frequency of the interference is very high near the edge of the dimpled interface due to a high deformation created by the lubricating film during an application of relatively high compressive load. The analysis presented in this section is restricted to the center of the dimpled surface, which is highlighted in Figure 61, since high-frequency fringe-patterns outside of this region cannot be resolved, and therefore, no useful information can be obtained there.

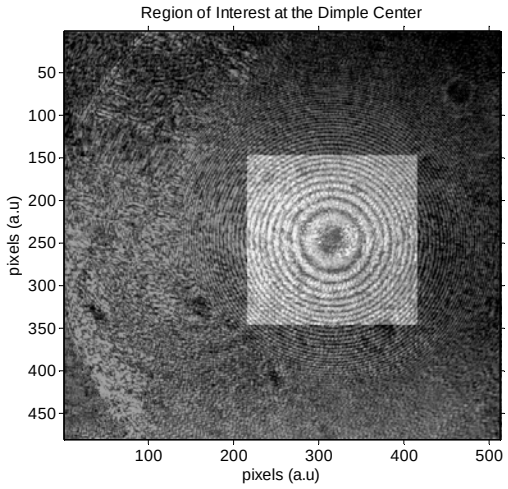


Figure 61. Fringe pattern at the onset of shape-transition process. The interfacial structure is reconstructed in the highlighted region. The fringe patterns outside this region are not resolved due to a high curvature of the free-surface of the droplet.

The interferograms presented in Figure 62(a)-(c) are obtained from the three instances of time during the shape transition process. The patterns are different at each instant of time, showing the dynamic nature of the process. By exploiting the axisymmetric nature of the evolution process, one could generate its spatio-temporal representation, which is sufficient for expressing the entire field of the interface within the region of the interest. The spatio-temporal representation, presented in Figure 62(d), is constructed by plotting the intensity patterns at the center of the droplet, marked by white-dots in Figure 62 (a)-(c), against the time axis.

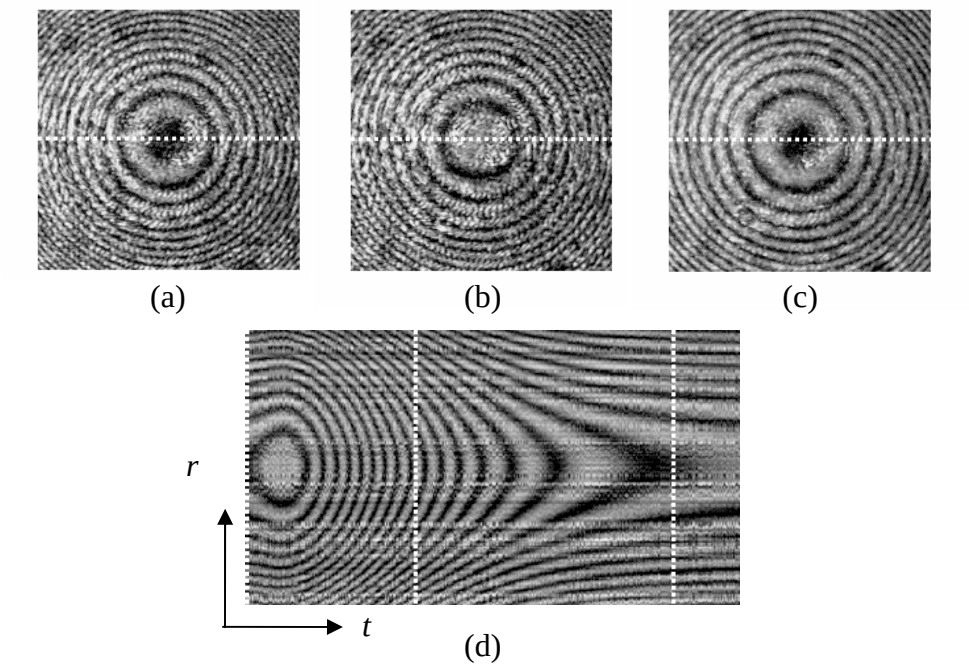


Figure 62. Fringe patterns from three instances of time, corresponding to (a) t = 0; (b) t = 1; (c) t = 2.5 s. (d) Spatio-temporal representation of the fringe pattern at the center of the droplet. The dotted lines in (a)-(c) are also drawn in (d). r and t are the radial and time axes, respectively.

The algorithm from Chapter 4, which was developed for studying the dynamics of the liquid-gas interface during a forced oscillation, has been employed for retrieving the shape of the interface from the spatio-temporal interferogram. The result presented in Figure 63 shows the shapes of the liquid-gas interface, and **not** the absolute film thickness measured between the free surface and the glass; this information cannot be retrieved from the present technique. The concave nature of the surface (along the coordinate labeled "Pixels") corresponds to the shape of the dimpled interface, at the center of the nonwetting droplet, at each instant of time. Accompanied by the process is the overall displacement of the liquid-gas interface by ~ 5 μm towards the glass surface, which is located somewhere above the retrieved surface. As can be interpreted from these results, the process involves the thinning of the lubricating film at the central region of the dimpled interface. As stated before, the process is autonomous; once initiated, the interface evolves to the new configuration without any additional squeezing applied to the droplet.

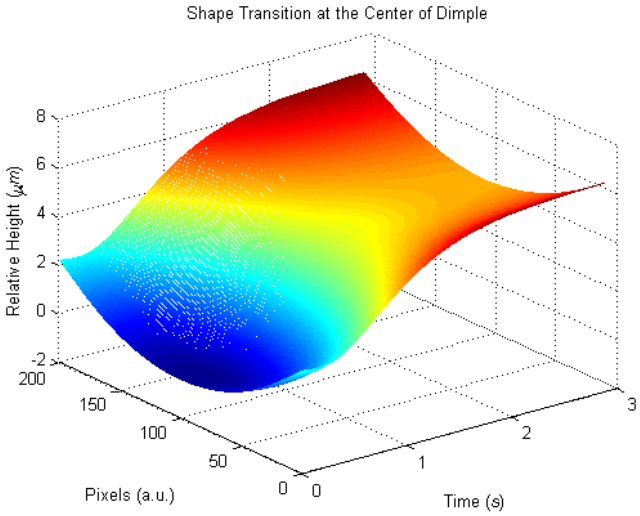


Figure 63. Shape of the interface reconstructed from the spatio-temporal interferogram in Figure 62(e). The free-surface is displaced by ~ 5 μm towards the glass surface, placed somewhere above this image, as the time elapses. The entire process takes about 3 seconds.

3.9.3. Discussions Based on Normal-Mode Analysis

A normal-mode analysis from hydrodynamic-stability theory can be used to gain insight to the shape-transition process. Using the conventions from the theory, the disturbance velocity-vector $\underset{\sim}{u}'$ may be expressed as

$$\underset{\sim}{u}' = \hat{\underset{\sim}{u}}(z)\exp\left[st + i(kr + m\theta)\right], \qquad (44)$$

where $\hat{\underset{\sim}{u}}$ and s are the amplitude and the growth rate of the disturbance, respectively, and k and m are wave-numbers in the radial and azimuthal directions, respectively. By observing the transition process, as seen in Figure 62(d), the growth rate of the perturbation seems to be damped out over the time interval of the recording and shows no oscillatory behavior ($s \approx 0$). The process, therefore, is accompanied by a quasi-steady transition between two steady states. In addition, the azimuthal wave number is m = 0 since the process is axisymmetric in nature. On the other hand, the shape transition is accompanied by changes in radial wavenumber. The transition process tends to widen the central region of the dimpled interface (at the apex of the droplet), leading to a

reduced wave-number in the radial direction, *i.e.*, $k_2 < k_1$. This result is more readily seen in Figure 58 for the case of shallow droplet.

The relationship $k_2 < k_1$ (widening of the dimple) can be interpreted graphically by applying the Fourier Transform to the interferograms taken before (Figure 64(a)) and after (Figure 64(c)) the shape transition. The transformed images show a narrower bandwidth after the shape transition (Figure 64(d)) than before (Figure 64(b)). Because the fringe's spatial frequency (or the wave number) is proportional to the curvature of the liquid-gas interface, a narrower bandwidth in the frequency domain is equivalent to a flatter surface in the spatial domain.

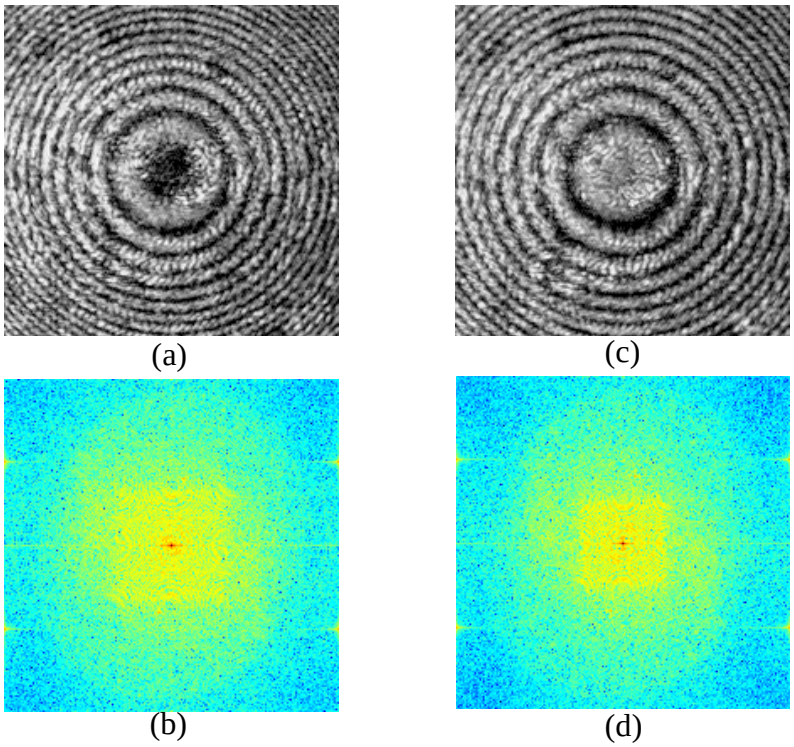
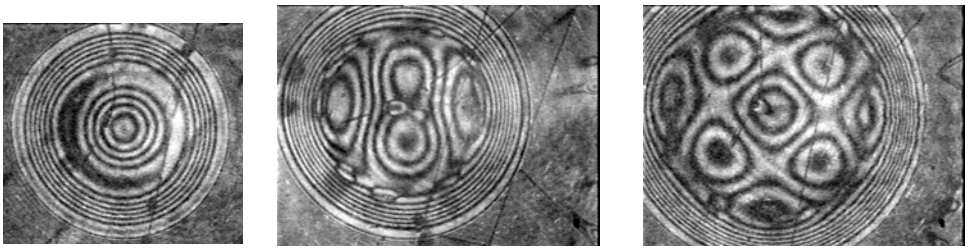


Figure 64. (a) Raw interferogram at *t* = 0 *s* and; (b) its power spectrum showing the components of frequency. (c), (d) Same analysis at *t* = 2.88 *s*. The power is concentrated in the lower spectrum in (d) than (b), indicating a flatter interfacial shape after the shape transition.

3.9.4. Square-Pattern Formation

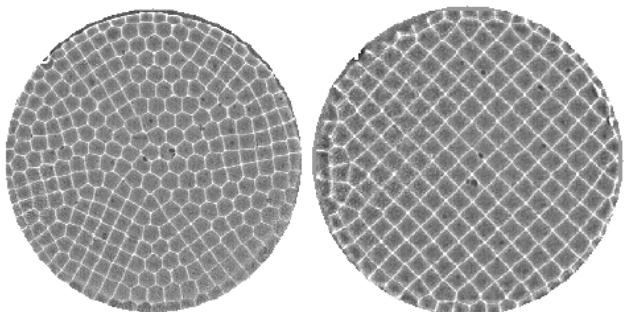
The mechanism of the transition process, discussed in the previous sections, may be similar to the one associated with Bérnard-Marangoni instability (Drazin & Reid (2004)). This type of (thermocapillary) instability can be driven by heating a shallow layer of liquid from below, yielding various flow patterns as different temperature gradients are imposed across the liquid layer. In fact, various flow patterns were observed in the nonwetting system, for a very flat droplet (very small volume) by imposing a relatively high temperature gradient across the droplet ($\Delta T > 50$ °C). The images presented in Figure 65 show some of the different patterns that arise in this scenario with a progressive squeezing from (a) to (c) on the same droplet.



(a) (b) (c)

Figure 65. (a)-(c) Various interface shapes exhibited by a shallow nonwetting droplet by imposing a high temperature gradient. The relative displacement increases from (a)-(c). The interface shown in (b) is unsteady.

The last of the image (Figure 65(c)) shows a square-cell pattern. A similar pattern may also be seen in a traditional Bérnard-Marangoni system with a large aspect ratio (defined as the twice the radius to the depth of the liquid) by exceeding some threshold criterion. For example, a system discussed in the review article by Schatz & Neitzel (2001) shows a loss of stability of hexagonal flow-pattern and the transition to a new, square cell-pattern, as seen as the sequence from (a) to (b) shown in Figure 66, which occurs at around $Ma \sim 688$, according their report.



(a) (b)

Figure 66. Transition in the square-cell patterns in Bérnard-Marangoni convection. (a) and (b) corresponds to Ma ~ 410 and ~ 688, respectively. Source: Schatz & Neitzel (2001).

An estimate of the Marangoni number at the onset of the square-cell pattern shown in Figure 65(c) has been attempted, to compare with the results reported in Schatz & Neitzel (2001). Because the droplet was very shallow, the height of the droplet is assumed to be in the neighborhood of $H \sim 0.5\ mm$. The imposed temperature difference was noted to be slightly higher than $\Delta T \sim 50$ °C (we use this value for the present analysis in the absence of reported ΔT). Using the fluid properties of 5 *cSt* silicone-oil, the Marangoni number defined in equation (43) is roughly 4200. This estimate, however, is an order of magnitude higher than that reported in Schatz & Neitzel ($Ma \sim 688$). The discrepancy in the value would be due to several factors. First, the difference in the aspect ratio is considered; the aspect ratio is roughly $3mm/0.5mm = 6$, assuming the radial extent of the fluid layer is nearly identical to the radius of the disk due to the flattened nature of the very shallow droplet considered here. Systems with small-aspect-ratio containers are discussed in various articles, such as Koschmieder & Prahl (1990) and Pasquetti, *et al.* (2002), but their flow patterns are different from ones observed in the present thermocapillary nonwetting system, observing the onset of pattern formation to occur for $Ma = O(10\text{-}100)$. This would lead us to suspect, as the second factor of the discrepancy, that the boundary conditions play the role. For an instance, the presence of rigid-wall in the conventional system studied by various authors would be different from the case of thermocapillary nonwetting system, where the boundary condition would be closer to a stress-free wall at the edge of the free-surface. Another possible explanation

for the discrepancy would be the thickness ratio between the air and the liquid layer. The linear stability analysis by Golovin, *et al.* (1995) predicts that longer wavelengths (such as seen in thermocapillary nonwetting droplet) become unstable (critical $Ma \sim 50$) and the experimental study from Mizev (2004) show a decrease in the critical Marangoni number as the thickness of the film becomes small. Although the thickness of the gas certainly plays a critical role in the instability mechanism, no relevant studies has been carried out using gas thickness with an order of few μm due to difficulties associated with maintaining uniformity of the contact line at the side wall (Schatz & Neitzel (2001)).

3.9.5. Discussion

The present section has focused on the analyses of the shape transition of a nonwetting droplet. The process is triggered once some threshold conditions of a nonwetting system are surpassed. In terms of displacement and the load, their thresholds increase with the volume of the droplet. In addition, Marangoni numbers at the onset of transition are evaluated, under assumption that the instability is triggered by thermocapillarity. The data show similar Marangoni numbers at the onset of transition process between the two systems, namely $\nu_l = 5\ cSt$ at $\Delta T = 5$ °C and $\nu_l = 10\ cSt$ at $\Delta T = 10$ °C.

The series of interferograms was analyzed with the reconstructed surface clearly showing the displacement of the free surface towards the glass surface. By employing normal-mode analysis, the autonomous process has been characterized by a transition of one stable, steady-state system to another. Associated with the process are changes in the wave numbers in radial and axial directions, both of which decreased after the transition process analyzed in this section.

Because the thermocapillary nonwetting system is driven by thermal-Marangoni convection, the transition process is believed to be triggered by mechanisms similar to Bérnard-Marangoni instability studied by various authors. In fact, observations of various flow fields confirm such hypothesis. The Marangoni number was estimated for the case of square pattern observed in thermocapillary nonwetting system, and compared to the conventional systems. The estimate is orders of magnitude higher than the

conventional system, possibly due to differences in system configurations and boundary conditions.

3.10. Instability Caused by Anti-Wetting Coatings

An anti-wetting coating is applied to the disk support in order to pin the contact line of a nonwetting droplet more effectively. Without any coating, pinning failure can occur at early stages of loading. On the other hand, not all coatings guarantee satisfactory operation of a nonwetting system. As it turns out, some anti-wetting agents can modify the interfacial properties of the nonwetting droplet, thereby reducing the load-carrying capabilities of thermocapillary permanent nonwetting systems.

Two types of anti-wetting coatings have been used in the present study. The first is Scotchgard from 3M, which has been used throughout the experiments with 5 and 10 *cSt* oils on the 3 *mm* disk support. Because our supply of this specific anti-wetting agent was exhausted during the course of research, experiments were continued using a new Scotchgard product. The new Scotchgard, however, has produced inconsistent and erratic film failures, with frequent observations of a "wobbling" interface prior to failure. The problem stems from the new chemical formula contained in the new Scotchgard. 3M has stopped manufacturing the old formula due to environmental concerns, and the old Scotchgard, which has been used for the early experiments, has been removed completely from the market. In order to find a suitable replacement for the original Scotchgard product, several anti-wetting agents from various companies have been tested with mixed success. The main reason appears to be their miscible nature with the silicone oils. Many of the newly tested samples mix readily with silicone oil, modifying interfacial properties of the oil, whereas the old Scotchgard is immiscible with silicone oil (at least to the naked eye). Furthermore, some of the tested samples fail to induce permanent nonwetting at all, even though they do not appear to mix (again, to the naked eye) with the silicone oil. Their inability to induce nonwetting is believed to be derived from foreign chemical species released to silicone oil, modifying the surface tension and thus interfering with thermocapillary convection. One plausible explanation for this is the solutocapillary effect, which results from the accumulation of the surfactant at the apex of

the droplet, opposing thermocapillary convection. If the solutocapillary effect is too strong, wetting may occur as soon as a droplet makes an apparent contact with the glass surface. Some visual evidences will be described in section 3.10.1 below.

3.10.1. Inferred Evidence of Solutocapillary Effect

One product, which has yielded consistent results, is Rainoff MFB from Eastern Chemical & Color Co. New sets of data were obtained using the new anti-wetting agent for 5 and 10 *cSt* oil on the 3 *mm* disk, in order to compare the results with the ones obtained with former Scotchgard. The first result shown in Figure 67 is the comparison of the data between the two coatings for ν_l = 5 *cSt* oil at ΔT = 20 °C and on d = 3 *mm*. Film failure, which could not be triggered with the old Scotchgard, could now be triggered for this specific working environment. The instances of film failures are labeled as "Film, Sudden" or "Film, Soluto" in the legend, where the prior one indicates a sudden occurrence of wetting and the latter one is accompanied by the observation of a wobbly interface.

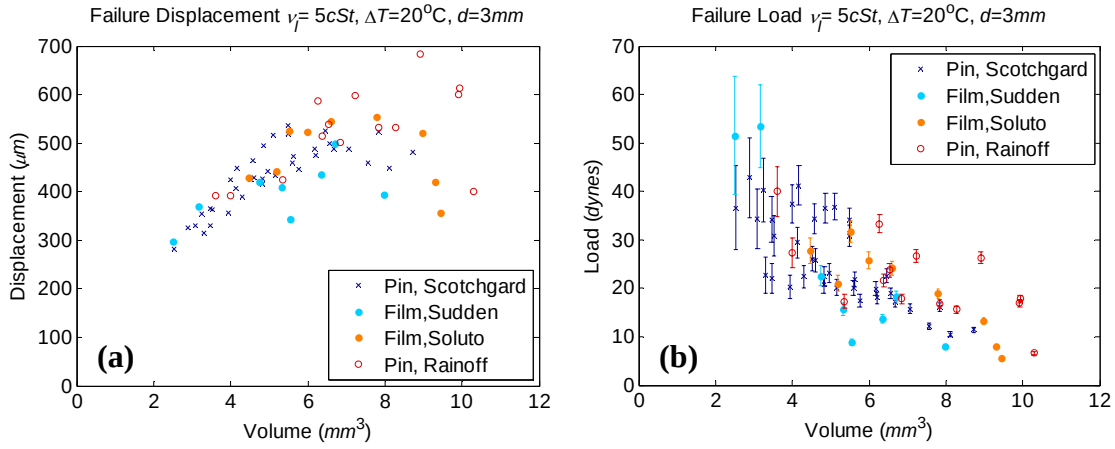


Figure 67. Comparisons of failure (a) displacement and; (b) loading between two coatings. The result is for a system with ν_l = 5 *cSt*, ΔT = 20 °C, d = 3 *mm*. The new data include film failures, which did not occur with Scotchgard.

The increased instances of film failures, and the failure displacement (and load) falling short of the pinning failures indicate that the new anti-wetting agent does affect the load-carrying capability of the permanent nonwetting system. In fact, the interface of

the droplet was observed to wobble with the Rainoff, leading to a growth of instability just prior to film failure. These results and the observations may point toward the modification of the interfacial properties of silicone oils due to the presence of foreign chemicals released by the coating. The mechanism of solutocapillarity, which opposes thermocapillary convection and thus effectively reduces the free-surface speed, may play a role in inducing film failure here. The argument can explain the instances of film failure when the Rainoff was used, whereas the Scotchgard only produced pinning failure. In addition, the new sets of results also suggest that Rainoff is as effective as old Scotchgard in anti-wetting properties, indicated by similar values of relative displacement and corresponding failure-loading. It is suspected that the amount of chemical species released on the droplet is so slight, that the interstitial properties are minimally affected and pinning failure could take place.

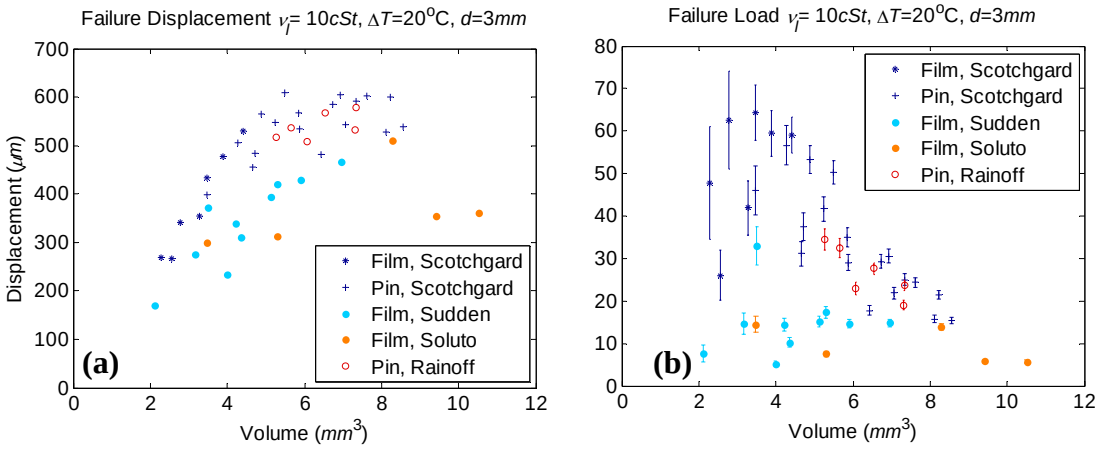


Figure 68. Comparisons of failure (a) displacement and; (b) loading between two coatings. The result is for a system with ν_l = 10 *cSt*, ΔT = 20 °C, d = 3 *mm*.

The same experiment was repeated for the system with higher viscosity with ν_l = 10 *cSt* oil at ΔT = 20 °C on d = 3*mm*, and the results are presented in Figure 68. Again, film failures are triggered at relatively lower values of the displacement with Rainoff than the old Scotchgard. The corresponding failure load lies at roughly 10 *dynes* throughout the range of the volume tested, which is well below half the values obtained using Scotchgard.

3.10.2. Visualization of Solutocapillary Effect

It has been noted that the interface of the droplet becomes distorted at the center of the dimpled interface while running experiments with the Rainoff as the anti-wetting agent. Although the free surface under the influence of the solutocapillary effect may exhibit a quasi-steady motion, the system remains stable at earlier stages of displacement. As the droplet is compressed further, however, the interface becomes unstable and wetting results. As discussed earlier, the data points corresponding to such observations are indicated as “Film, Soluto” in the legend in Figure 67 and Figure 68.

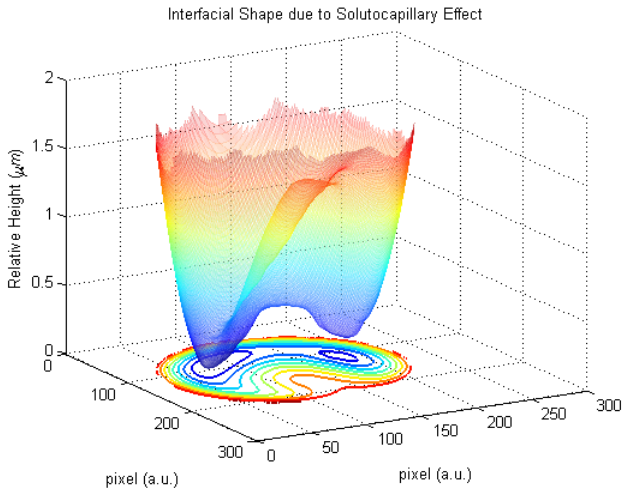
Two interferograms were captured, showing the solutocapillary effect. The distortion can be clearly seen clearly on the apex of the droplet in the first image presented in Figure 69(a). The (central portion of the original) image in Figure 69(b) has been analyzed using the similar technique from Chapter 4, recovering the details of the nonuniform structure in this region with two troughs and a protrusion (Figure 69(c)). The distortion on the liquid-gas interface implies nonuniform pressure distribution at the center of the dimpled interface, where thermocapillary convection is directed from the rim of the dimpled interface. The protrusion, shown as a bent fringe pattern, extends into the gas phase present above the reconstructed surface structure in Figure 69(c).



(a)



(b)



(c)

Figure 69. (a) Raw interferogram showing solutocapillary effect on the free surface of a nonwetting droplet. (b) Center region affected by the solutocapillary flow. (c) The shape of the interface obtained from (b).

The second image in Figure 70(a) was captured after some additional squeezing was applied to the same droplet shown in Figure 69. The trough has disappeared from the surface, while the protrusion is further extended into the gas phase as can be seen from the reconstructed surface in Figure 70(c). Further squeezing from this point resulted in instability of the system, where the region of the protrusion grew until a wetting took place.

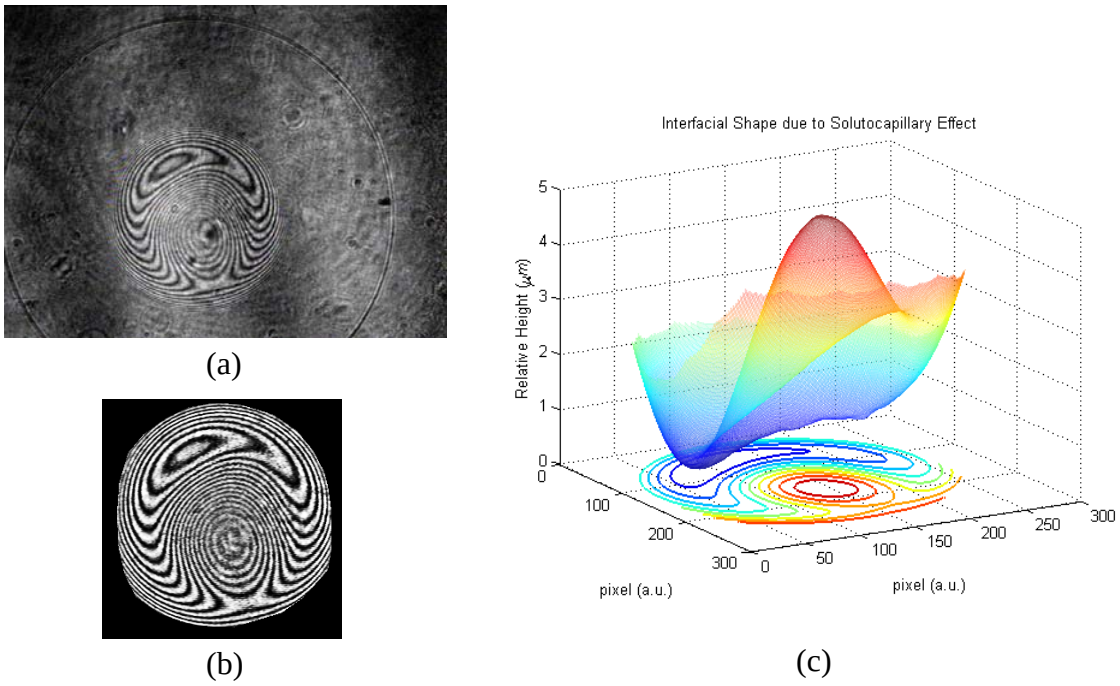


Figure 70. (a)-(c) Same as Figure 69 after an additional squeezing was applied to the same droplet.

These nonuniform free-surface structures visualized in this section would indicate the presence of some disturbance that seems to oppose the thermocapillary convection, distorting flow fields and pressure distributions on the free surface. In addition, the experimental results from the previous sections have shown the increased instances of film failure and the reduction in the film-failure load. All of this evidence supports the notion of a reduced free-surface speed and an unstable system, which is most likely due to the solutocapillary effect.

3.10.3. Hypothesis on Solutocapillarity Effect

A qualitative description of these behaviors may provide an insight to the present discussion of the solutocapillary effect. In a permanent nonwetting system, the motion of the liquid-gas interface is directed towards the center of the contact region due to thermocapillary convection. If any surfactant or foreign chemical is present on the free-surface, the molecules also follow the thermocapillary convection and accumulate at the droplet apex.

The distribution of the surfactant can be assumed axisymmetric initially, with its concentration gradient opposing that of the temperature. The situation is sketched in Figure 71(a). As higher squeezing is introduced from this point, the strength of the thermocapillary convection increases, confining the surfactant into a smaller region, creating a larger concentration-gradient on the free surface. At some point, the surface-tension gradient generated by two competing factors may lead to instability, as seen in the conceptual sketch of Figure 71(b), leading to a nonuniform distribution of the surface-tension forces.

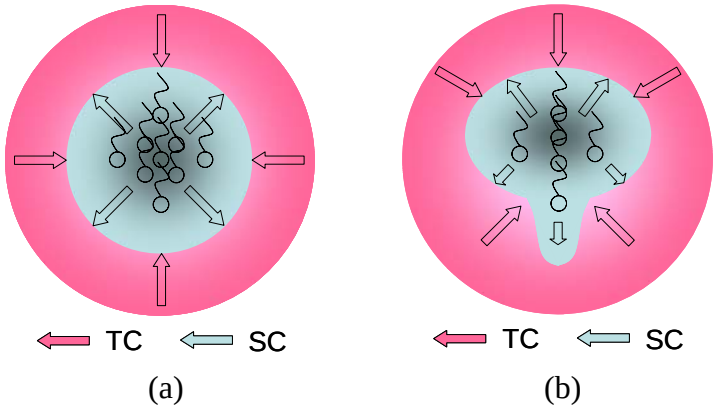


Figure 71. (a) Surface-tension gradients generated by thermocapillary (TC) and solutocapillary (SC) effects on top-center of a nonwetting droplet. (b) Non-uniformity of the concentration gradient introduces pressure variations on the free surface. Chemical species are indicated by ball-squiggle shape, and the magnitude of the gradient-vectors is indicated by the length of the arrows.

3.10.4. Discussion

The present section has attempted to describe and characterize the different mechanism of film failure brought out by the use of a new anti-wetting agent. The new sets of results show an increase in the instances of film failures and the reduced values in the failure load, both of which may indicate the modified interstitial-properties and the resultant solutocapillary effect. The argument is backed by observation of the quasi-steady nature of the irregularly shaped interfaces, the shapes of which have been reconstructed from their interferograms. The reconstructed surfaces show the details of

the nonuniform structure at the apex of the droplet, where chemical species are assumed to accumulate. Finally, a hypothesis for such instability has been presented. This instability is assumed to be triggered by the competition between soluto- and thermo-capillary effects.

3.11. Experimental Results: Dynamic Failure

The foregoing discussion has been concerned with the failure of nonwetting systems in quasi-static fashion, *i.e.*, the droplets were squeezed very slowly with a time increment below the viscous time scales defined for each system. In this section, system failures will be investigated under a dynamic environment. The study is motivated by the system's potential applications in dynamic environments.

The modified experimental apparatus used for the study is presented in Figure 72. The new apparatus allows a droplet to be shaken by a mid-range speaker (1: RadioShack, Cat # 40-1282C) placed underneath the disk support. In order to constrain the forcing to one axis, a linear ball-bearing system (2: Thomson Industries, Model TWN 4) is placed. A vibrometer (3: Polytech, Model OFV 303) and its controller (Polytech, Model OFV 3001) have been implemented to measure the displacement of the amplitude of the vibrating disk. Because the vibrometer shines the laser beam on the vibrating object and reflects it back to the sensor in order to evaluate the amplitude of the oscillation, the surface of interest must be reflecting. To do so, a reflective mirror (4) is mounted on a surface attached to the disk support.

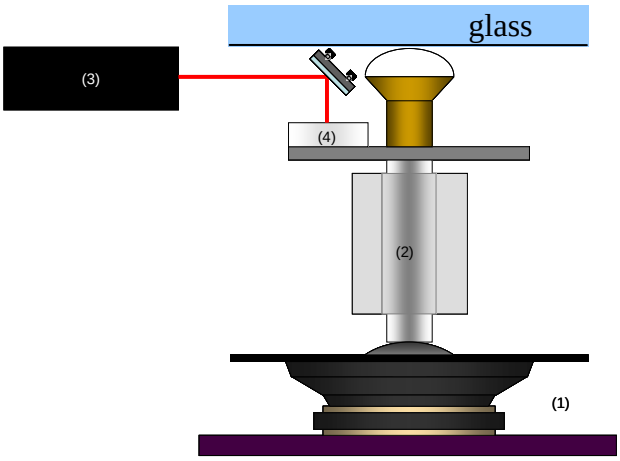


Figure 72. Experimental apparatus used for the measurement of failure under dynamic environment. The rest of the system remains the same as the one used for the static-failure experiment.

3.11.1. Experimental Procedure

Most of the experimental procedures used in this section are similar to those used in the static-failure measurement. Here, the droplet is vibrated by the speaker once the temperature difference is imposed between the respective surfaces. The droplet must be oscillated before the detection of the initial contact with the glass surface, because the initial positions of the speaker's membrane vary between experiments. Once set into vibration, the membrane oscillates about its mean position, allowing the initial positions of the droplet to be deduced. The initial amplitude of the oscillation is kept small ($\sim 15 \mu m$) before the droplet is squeezed. Once the tip of the droplet is detected from interferometry during the upstroke phase of the forcing, the vibrating droplet is squeezed 225 μm against the glass surface. From this point, the amplitude of the forcing is slowly increased ($\sim 10\ \mu m$ every 10 s) until failure is triggered.

The equivalent displacement $\mathscr{D}_{eq}$ at the point of failure is evaluated from the following formula

$$\mathscr{D}_{eq} = 225 - 7.5 + A_f \qquad (45)$$

where 225 (μm) is the initial displacement introduced on the system, 7.5 (μm) is the mean of the initial forcing-amplitude, and A_f is the amplitude of the forcing at the system failure.

The computation of the load is not carried out in this case; Surface Evolver can't be used to model the load in a dynamic environment reliably. Only the relative displacement at failure will be reported here.

Rainoff from Eastern Chemical has been used as the anti-wetting agent throughout the experiment.

3.11.2. Results and Discussions

An experiment is carried out for ν_l = 10 *cSt* at ΔT = 20 °C on a 3 *mm* disk support with the input forcing frequency f = 60 *Hz*. A comparison of the failure displacement of the static and dynamics systems is presented in Figure 73.

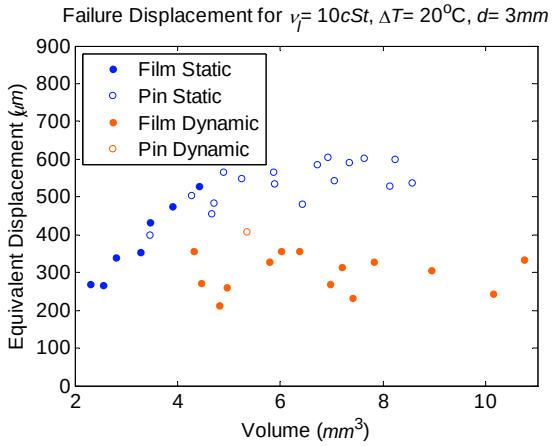


Figure 73. Comparison of the failure displacement of static and dynamic systems for ν_l = 10 *cSt*, ΔT = 20 °C, *d* = 3*mm*. The forcing frequency is at 60 *Hz*.

The failure-displacement results are considerably smaller under the dynamic environment than the ones from the static-failure experiment. In addition, all but one data point exhibit film failure. For the range of volume between 4–8 mm^3, the failure displacement lies around 300 μm in the forced system, whereas it varies ~ 500–600 μm in the static system. It is likely that instances of film failure increase in the dynamic system

due to a large-amplitude response of the liquid surface, squeezing the gas from the region, thereby reducing its ability to prevent contact between solid and liquid.

These results exhibit a failure due to one type of dynamic response, corresponding to the first mode (prolate-oblate oscillation) of the free surface. Due to the complexity of the dynamic response, however, the failure displacement is expected to depend on the modes excited by the pedestal oscillation. It is anticipated that failure will occur at even lower squeezing than for the cases presented in this section if the deformed free surface penetrates locally into the lubricating-film region at its thinnest point. Such behavior could be observed, for example, for a dynamic response of the type shown in Figure 74.

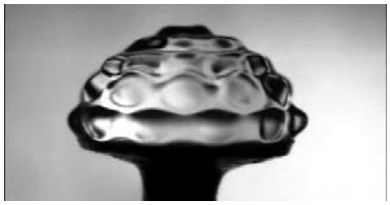


Figure 74. High-mode excitation of isothermal, pinned droplet, showing an azimuthal component of the free-surface response.

3.12. Concluding Remarks on Nonwetting Failure

The present research attempted to quantify nonwetting system failures under static and dynamic environments. All of the results exhibit a large scatter in the data, possibly due to a finite transmission of environmental noise. The presence of the noise was more evident in the nonwetting system with a large (5 *mm*) disk diameter, which may be due to the proximity of the droplet's characteristic frequency to the excitation frequency from the environmental ($O(10\ Hz)$). In such a system, an erratically vibrating surface was noted from the interference pattern with the amplitude of oscillation ~ 8 *nm*.

Qualitative descriptions are provided to characterize film- and pinning-failures for various system configurations, including the pendant system. It is argued that film failure is initiated by instability of the flow fields within the lubricating film. The experimental results confirm that the stability of the film increases with the speed of the free surface, indicated by the reduced instance of film failure and the higher load carried by a nonwetting droplet, as the temperature difference is increased. Scaling arguments are

presented in order to estimate the shear rate, a possible criterion of instability associated with the shear-flow present within the contact region. In addition, the onset of the film instability is documented as a series of interferograms. Analysis of these images shows the propagation of a disturbance on the free surface, in the azimuthal direction prior to film failure, which is followed by wetting. Pinning failure, on the other hand, is less sensitive to the temperature difference. A subtle increase in the failure load is noted between ΔT = 2 and 20 C^{o} for 5 *cSt* oil, which is explained by reduced pinning angles associated with the pumping mechanism of thermocapillary convection. Also, a higher load carried by more viscous liquid is attributed to the amount of work required to displace a droplet, which is proportional to the viscosity and inversely proportional to the droplet height. It is also argued that boundary conditions at the disk support play a critical role in pinning failure.

In addition, nonwetting droplets have been observed to undergo a shape transition. The transition is characterized by an autonomous change in the shape of a liquid-gas interface. Since the nature of the transition resembles thermocapillary instability, Marangoni numbers are evaluated at the initiation of the shape transition. In addition, the recorded sequence of the transition process is analyzed, recovering the details of the interfacial shapes. The growth rate of the disturbance seems to be close to zero or is dissipated during the process, and the wave numbers in the new stable system are longer in the axial and radial directions on the free surface of a droplet.

The solutocapillary effect has been argued to modify the interstitial properties in a nonwetting system when a different anti-wetting coating is implemented. Although the new agent seems to yield a consistent output, the presence of a solutocapillary effect, which opposes thermocapillary convection and thus reduces the effectiveness of the lubricating film, lowers the overall load-carrying capability of the nonwetting system. Two interference patterns, under the presence of what seems to be the solutocapillary effect, are analyzed. The reconstructed surfaces have revealed the details of the nonuniform interfacial structure and the growth of the protruded section on the free surface.

Finally, failures have been analyzed under dynamic environments. The values of failure displacement are lower in the dynamic environment than in the static one. It has been argued that the amplitude response of the free-surface penetrates into the lubricating film, squeezing the air out of the contact region and resulting in film failure.

These descriptions are intended to provide detailed, qualitative arguments of nonwetting-system failure. The author hopes that combinations of the knowledge gathered from these analyses will aide an engineer to design a load-bearing, vibration damper, or other engineering applications by exploiting thermocapillary nonwetting system.

4. Profiling Oscillating Surfaces

(This chapter is adapted from the published result of van den Doel, *et al.* (2004))

The liquid and solid surfaces, in the interest of permanent nonwetting, are separated by a lubricating film of air with a thickness of a few microns. This lubricated region has been termed as the contact region throughout the thesis. If any external excitations are imposed on the droplet, its surface is displaced from an equilibrium position, squeezing the film of air and reducing the film thickness. If the amplitude of the displacement is large enough, wetting can take place. When the application in a microgravity environment, such as abroad the International Space Station in earth orbit, is considered, the performance of a nonwetting system can be affected due to a structural vibration called the "*g*-jitter". It is therefore important to understand the dynamic responses of a nonwetting droplet subjected to external excitations.

Interferometry is a nondestructive technique commonly used for profiling surfaces of an object offering resolution down to the order of the wavelength of the incident light. Interference patterns arise due to the wave nature of the light, appearing as destructive (black) and constructive (white) patterns due to the optical path difference traversed between the reference and the reflected beams. These patterns can be used to gain insights to the profiles of an object, in this case the liquid-gas interface. In the past, interferometry measurements have been performed on static, permanent-nonwetting systems, providing qualitative and quantitative understanding of the physics of lubricating film. For example, the angle-shifting technique was employed by Dell'Aversana, *et al.* (1997) to measure the absolute film thickness, and revealed the dimple formation on the liquid-gas interface.

Difficulties arise, however, for extracting information about dynamically moving liquid-gas interfaces. For example, the angle-shifting method used by Dell'Aversana, *et al.* (1997) would require that the beam angle be shifted very quickly between image sequences, a challenging task given the time scale of the dynamic event. Although there are other interferometry techniques, such as spatial-shifting and temporal phase-shifting methods (Takeda, *et al.* (1982),Huntley & Saldner (1997)), for extracting information of dynamically moving surfaces, they require intricate experimental setups that are different

from ours. Therefore these methods were not pursued here. Instead, an optimization technique is employed in the present analysis, enabling the reconstruction of an oscillating surface from a series of interferograms.

The new experimental apparatus requires only minor adjustments to the already-existing apparatus used for the failure experiment (Figure 23). The changes are:

i) speaker placed under the copper for exciting droplet

ii) A mechanically rotating paper, instead of the beam expander, to diffuse the laser beam and illuminate a large area.

iii) A high speed camera (Kodak Motion Corder Analyzer, SR Ultra) for recording dynamic interference patterns.

4.1. Experimental Methods and Analysis

Two experiments have been carried out to demonstrate the capability of the technique that allows a reconstruction of dynamically moving surfaces. The first experiment (which shall be described as "forced" from here on) is performed for a forced oscillation of a thermocapillary nonwetting droplet subjected to a continuous excitation with an input frequency ~ 17 *Hz*. In this case, the interferograms are recorded at the frame rate of 1000 *Hz*. The second experiment (described as "damped" from here on) employs a similar droplet excited at ~ 54 *Hz*, for which the forcing is terminated during the recording and the surface oscillation is allowed to decay freely. In this case, the frame rate of the high speed camera is set at 3000 *Hz*. These tests are carried out for silicone oil with ν_l = 10 *cSt* on a 3 *mm* disk for ΔT ~ 25 °C (T_H ~ 45 °C and T_C ~ 20 °C). A relative displacement, volumes of droplet, and amplitude of oscillation are not reported for these studies, given that the emphasis was on technique development.

4.1.1. Phase Estimation

The task of the minimization technique discussed in this section is to estimate underlying phase differences (to be called phase from here on) between the reference and reflected beams, recorded as an interference pattern. The optimal intensity I is assumed to follow the form

$$I \approx \cos\phi_0 , \tag{46}$$

where ϕ_0 is the underlying phase that arises due to the differences in the optical paths traversed by the reference and the reflected beams.

The algorithm attempts to minimize a cost function in order to estimate phase from an image. The cost function (for 2-D images analyzed in this thesis) can be defined as,

$$\Psi(r,t) = \sum_{(\eta,\varepsilon)\in\Omega} \left\{ \left[I(\eta,\varepsilon) - \cos\zeta_1 \right]^2 + \left[I(\eta,\varepsilon) - \cos\zeta_2 \right]^2 + \beta \left[\phi_0(\eta,\varepsilon) - \zeta_1 \right]^2 q(\eta,\varepsilon) \right\}, \tag{47}$$

where

$$\zeta_1(r,t,\eta,\varepsilon) = \phi_0(r,t) + \omega_r(r,t)(r-\eta) + \omega_t(r,t)(t-\varepsilon), \tag{48}$$

$$\zeta_2(r,t,\eta,\varepsilon) = \zeta_1 + \chi . \tag{49}$$

In the equations above, (r,t) and (η,ε) are pixel coordinates at the center and away from the center, respectively, within the sub-region Ω where the summation is applied. The minimization algorithm seeks three unknowns in equation (47), namely the phase ϕ_0 and its slopes ω_r and ω_t, by comparing the local intensity of the image I to the cosine of the model function for the phase. For example, the first term adds "energy" to the cost function if there is a large discrepancy between the recorded intensity and the cosine of the model function, which assumes the underlying phase to be first-order plane (equation (48)). Due to this assumption, the size of the sub-region Ω must be carefully chosen. For the present analysis, the size of the region is chosen as 11×11 pixels. The second term is the energy associated with the difference between the local intensity and the cosine of another plane, which is parallel to the plane ζ_1 and displaced by a small offset χ. The idea is that a phase with a small offset appears very similar to the one without the offset.

Without this term, the minimization process can easily be attracted to a wrong solution branch (Servin, *et al.* (2001)). The third term is the regularization term, imposing a smoothness on the estimate by weighing the phases that are already evaluated from its neighborhood (indicated by the field $q(\eta,\varepsilon)=1$). The regularization constant β provides the magnitude of the weight. For the present analysis, the values for the offset and the regularization constant are $\chi = 0.3\pi$ and $\beta = 0.1$, respectively.

MATLAB's Optimization Toolbox (fminunc) is used for the minimization scheme. The algorithm uses the steepest-descent method, which becomes more robust by supplying expressions for derivatives of the cost function with respect to the minimization variables, ϕ_0 , ω_r, and ω_t,

$$\nabla\Psi = \left[\frac{\partial\Psi}{\partial\phi_0}, \frac{\partial\Psi}{\partial\omega_r}, \frac{\partial\Psi}{\partial\omega_t}\right]. \tag{50}$$

4.1.2. Phase Scanning Strategy

In order to process the entire image, the minimization algorithm must be guided instead of proceeding in an arbitrary fashion. If it is not guided properly, the minimization process can easily be trapped into an erroneous solution branch, especially near saddle-points and maxima/minima of the phase. This is due to an ill-posed nature of the inverse problem associated with a cosine function used in the model equation (46) (Servin, *et al.* (2001)). One of the successful scanning strategies is to proceed along the contours of the fringe patterns as discussed in Servin, *et al.* (2001) and Servin & Quiroga (2001), and has been applied in Figure 69 for the analysis of interstitial shape under solutocapillary effect. By following fringe contours, the minimization avoids crossing over regions with an ambiguous phase or move across regions with drastic changes in a phase until all neighboring pixels have been successfully evaluated. This method requires an interferogram to be segmented so that the scanning follows each of the subdivided regions one at a time.

The different method employed here and discussed in van den Doel, *et al.* (2004) traces out contours of equal phase without the segmentation of interferograms. This is accomplished by evaluating all the phases in the 8-connected neighborhood around the

center of the pixel at (*r*,*t*) and sorting them in ascending order on either positive or negative registers defined about that point. The algorithm then proceeds to the next pixel in its neighborhood that contains the closest value of the phase from the previous step. The process assures that the minimization algorithm continues along pixels containing similar values of the phase values.

Once the minimization algorithm traces out the entire image the procedure must be repeated, making further refinements to the estimates and smoothing out regions with spurious errors that result from the first iteration. Details on the scanning strategies as well as a refinement procedure smooth out the phase after the initial minimization procedure are discussed in van den Doel, *et al.* (2004).

4.1.3. Image Processing

Before proceeding with the minimization, raw data must be preprocessed. This is because the minimization algorithm requires the intensity of the image to be modeled as $I \approx \cos\phi_0$, whereas typical raw images contain systematic noise, departing from this model. Had minimization been applied to a raw image, errors would have easily resulted during the minimization process. This section describes image-processing techniques used to get rid of the systematic noise inherent in our experimental system, so that the intensity in the image can be closely approximated by $I \approx \cos\phi_0$.

Raw images, as seen in Figure 75(a)-(c) and Figure 76(a)-(c), contain biases and noise, which cannot be completely eliminated regardless of the experimental apparatus used. A general expression for raw intensity profile is

$$I(x,y,t) = A_1(x,y,t) + A_2(x,y,t)\cos\left[\phi_0(x,y,t)\right] + N(x,y,t), \qquad (51)$$

where A_1 is a background illumination, A_2 is the amplitude modulation, and N is a random noise.

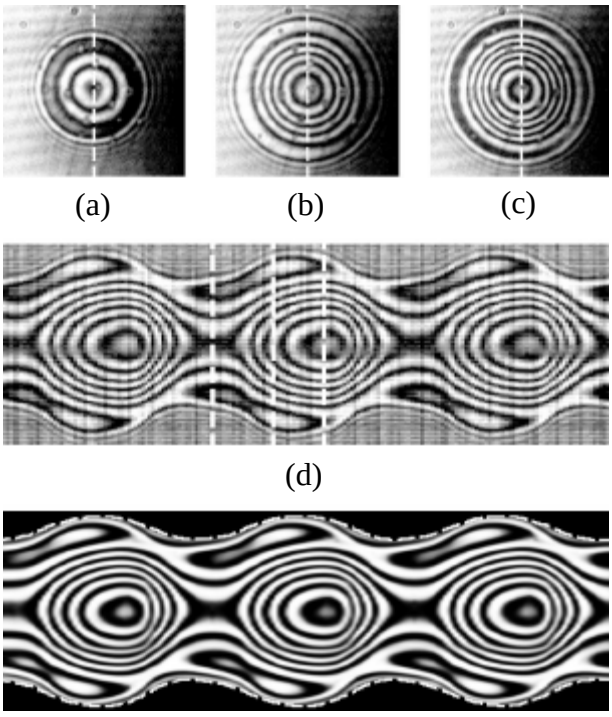


Figure 75. (a)-(c) Raw fringe patterns taken from the recorded sequence of the forced oscillations, excited at 17 *Hz*. (d) Spatio-temporal interferogram constructed from the recording. The dotted lines correspond to those shown in (a)-(c). (e) Interferogram after image processing. The dashed line is used to define the region containing the phase information. Source van den Doel, *et al*., (2005)

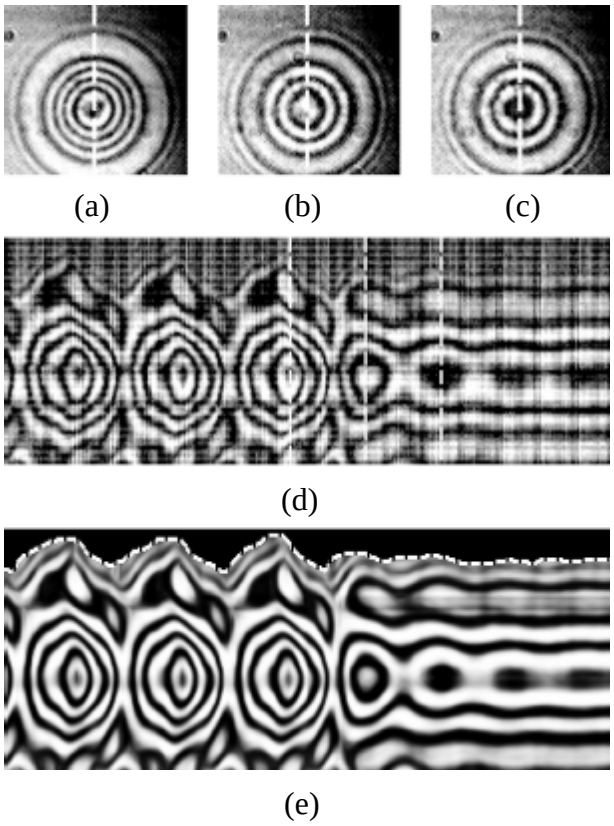


Figure 76. Same as Figure 75, except the sequence contains the damped oscillation towards the end of the recording. The input frequency is 54 *Hz*.

The term A_1 appears as biased shading, which can be seen as the variation of the intensity in the background of the raw images presented in Figure 75(a)-(c) and Figure 76(a)-(c). This type of shading can be removed by fitting a first-order plane to the borders placed around each image by least-squares and then subtracting it from the image. Another form of noise results from the high-speed camera's CCD array. Various modulations appear in the pixel intensity due to different amplifications at the readout channels. This artifact is smoothed out using an adaptive Gaussian filter, a directional filter that is applied along a plane, defined by the two smallest eigenvalues of the structure tensor of the original 3-D interferogram (van den Doel, *et al.* (2004)). This filter prevents the fringe pattern from being smeared out in all directions, as is the case with a conventional Gaussian filter.

After these steps, the intensity in the interferogram can be approximated by (van den Doel, *et al.* (2004))

$$I(x,y,t) = A_2(x,y,t)\cos\left[\phi_0(x,y,t)\right] + N(x,y,t). \qquad (52)$$

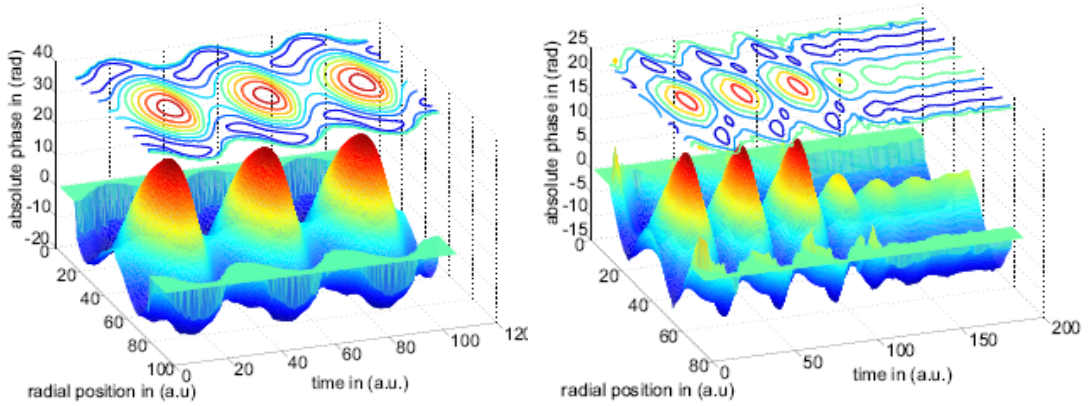
Accordingly, N needs to be removed and A_2 must be normalized. First, filtered images are generated by applying a large Gaussian filter, and these are subtracted from the original images, removing most of N. Second, the error-function clipping (van den Doel, *et al.*) is applied in order to normalize the image. Finally, a local variance filter (van den Doel, *et al.*) is used to define the "footprint" or the area containing the fringe data, separating the regions by 1(data) and 0 (no data). All of these image-processing steps are carried out using the DIPimage (Hendricks, *et al.* (1999)), freely available online.

The processed intensity maps are presented as spatio-temporal interferograms in Figure 75(e) and Figure 76(e). These are 2-D representations of the oscillations at the center of these droplets marked by the white dotted lines in (a)-(c) in these figures. Comparison of the unprocessed data (d) and the processed data (e), shows the latter to have a cleaner output, which is closely approximated by $I \approx \cos\phi_0$.

It is noted that the minimization algorithm discussed in the previous sections can generally be extended to a general 3-D interferograms. Instead, the minimization is applied to the spatio-temporal interferograms by exploiting the axisymmetry nature of the oscillation; no extra information is obtained by working with the 3-D image in the present case. In addition, a computational effort is reduced by a factor of 100 by eliminating one of the dimensions from the analysis (van den Doel, *et al.* (2004)).

4.2. Results

The results presented in Figure 77(a) and (b) show the shapes of the free surface, recovered from the spatio-temporal interferograms from Figure 75(e) and Figure 76(e) corresponding to the forced ($f \sim 17$ *Hz*) and damped ($f \sim 54$ *Hz*) oscillations, respectively.



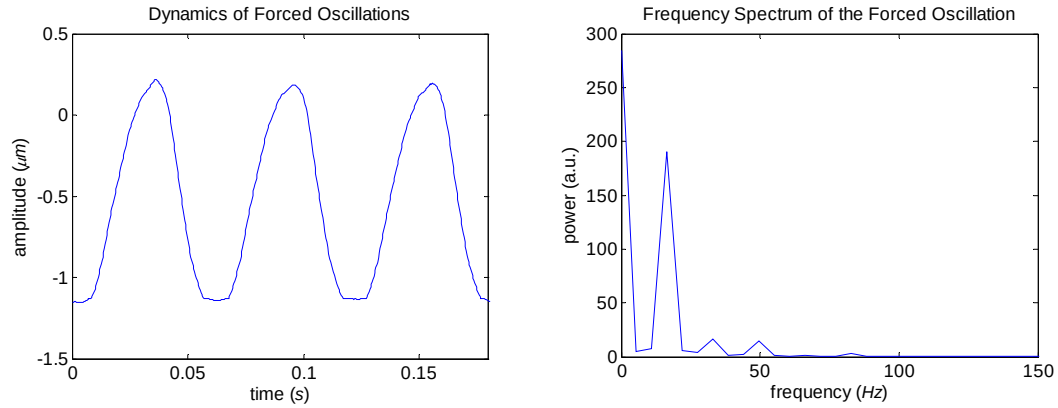
(a) (b)

Figure 77. Reconstructed shape of interface during the (a) forced and ;(b) damped oscillations. The forcing frequencies are about 17 and 54 *Hz*, respectively.

Using these recovered surfaces, the oscillations at the centers of the droplets are plotted. The results are presented in Figure 78(a) and Figure 79(a). In these results, the amplitude of the oscillation is evaluated from the retrieved phase ϕ_0 using the relation

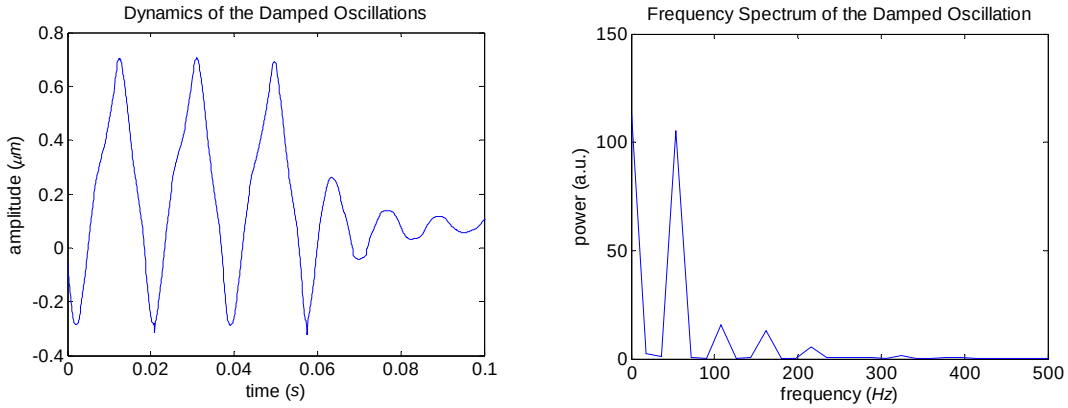
$$\text{amplitude} = \frac{\phi_0 \lambda}{4\pi}, \qquad (53)$$

where λ is the wavelength of the laser (632.8 *nm*). Because the minimization algorithm recovers "relative" and not the absolute phase information, the amplitude of the oscillation is also relative. This means that the actual position of the droplet surface with respect to the solid surface (film thickness) can't be determined from the present analysis.



(a) (b)

Figure 78. (a) Amplitude response of the surface at the center of the droplet from the forced oscillation. (b) Power spectrum of the Fourier-transformed signal of the oscillation shows the maximum peak around 17 *Hz* and small contributions from higher frequencies at 33 and 50 *Hz*.



(a) (b)

Figure 79. (a) Amplitude response of the surface at the center of the droplet from the damped oscillation. The forcing is terminated roughly around t = 0.06 *s*. (b) Power spectrum of the Fourier-transformed signal during the forced-portion of the oscillation shows the dominant peak around 54 *Hz* with contributions from higher frequencies at 108, 162, and 216 *Hz*.

These oscillations are not sinusoidal. For example, the forced oscillation in Figure 78(a) shows a slight asymmetry between the periods of up and down strokes. In addition, the oscillation has a plateau region during the lower phase of the oscillation. More complex dynamics is observed during the forced portion of the damped oscillation

($0 < t < 0.05\ s$ in Figure 79(a)). During this period, the shape of the oscillation departs far from a pure sinusoidal oscillation, resembling a triangular shape.

The discrete Fourier-Transform is applied to these data taken from the forced portions of these oscillations. This means that all of the data are analyzed from the forced oscillation (17 *Hz*), while a portion of the data in the time interval $0 < t < 0.05\ s$ is analyzed from the case of damped oscillation (54 *Hz*). Their power spectra are plotted in Figure 78(b) and Figure 79(b), showing components of frequencies present in these data. Both spectra show higher harmonics being excited, with integer-multiples of the input frequencies. For example, the modes at 33 and 50 *Hz* are excited in the case of forced oscillation, corresponding to 2 and 3 times the input frequency of ~ 17 *Hz*. For the damped oscillation scenario, modes at 108, 162, and 216 *Hz* are excited, corresponding to 2, 3, and 4 times the input frequency of ~ 54 *Hz*, with an additional, 4^{th} harmonic being excited by the forcing. The difference in the number of excited modes could be attributed to nonlinearity that may arise due to forcing frequency, the difference in the amplitude of the forcing, as well as the differences in the relative squeezing imposed on the system. A systematic investigation is required to determine the effects of these variables on the oscillatory behavior of the droplets under excitations.

In addition, the Fourier Transform is applied to the data in the time interval $t > 0.07\ s$ of the damped oscillation case, which corresponds to the decaying portion of the oscillation. The resulting power spectrum presented in Figure 80 shows a single peak around ~ 67 *Hz*, which is higher than the input frequency 54 *Hz*. Because the excitation is at the lowest mode excitation (axisymmetric, prolate-oblate oscillation), the single peak in the frequency spectrum indicates that the damped portion of the oscillation is decaying freely with the characteristic frequency of that particular system. Although its characteristic frequency 67 *Hz* was not directly excited by the shaker, it could have been excited by the higher harmonics (*e.g.*, 108 *Hz*) during the forced-portion of the oscillation ($0 < t < 0.05\ s$).

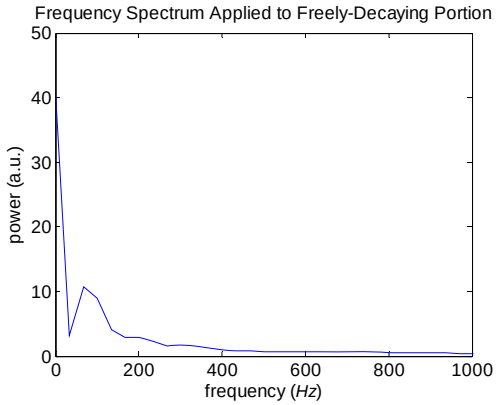


Figure 80. Power spectrum corresponding to the freely-decaying portion of the damped oscillation. The data is taken from ($t > 0.07$ *s*) of the original data presented in Figure 79(b). This graph shows a single peak around 67 Hz, which could correspond to the natural frequency of the system.

4.3. Discussions

Dynamic interferograms have been used to reconstruct the profiles of the oscillating surfaces using minimization techniques. The analysis requires original images to be preprocessed, removing the inherent, systematic noise prior to the minimization procedure. The minimization is carried out on the 2-D spatio-temporal interferograms, obtained by plotting the history of the fringe pattern at the center of the droplet. The algorithm traces out the contours of the isophase or equal height on the droplet surface, so that minimization process has less chance of getting trapped into wrong solution branches. The extracted surface profiles show complex dynamics of the free surface due to external forcing, excited at ~ 17 *Hz* and ~ 54 *Hz*. The spectral analysis of the oscillations shows that higher modes, with an integer multiples of the excitation frequencies, are excited.

It is noted that the frame rate of the high-speed camera must be sufficiently high in order to capture the dynamics of the interferograms. Therefore, the analysis is limited to low excitation frequencies. In addition, distinct fringe patterns must be resolved by the camera, limiting the analysis to a droplet with low-load application.

This chapter has focused on the development and proof of a technique for examining dynamic response of the nonwetting droplet under forcing. A complete study of the dynamic response within a frequency range of practical interest associated with applications of nonwetting droplets is beyond the scope of this thesis.

5. Droplet Levitation and Transport

The concept of droplet levitation and controlled manipulation of its positions on a solid surface has potential for Lab-On-a-Chip (LOC) applications. The benefits of handling a levitated droplet are multi-fold: *i*) a contamination-free environment for delivered sample; *ii*) versatility in generating various test configurations since a droplet can be positioned to any location on a test surface; *iii*) less complexity associated with a chip design since micro-channels and mechanical pumps are not required; and *iv*) faster delivery speed due to small friction and the non-contact nature of the droplet.

5.1. Experiments and Methodologies

Figure 81 below shows the experimental apparatus set up for the present research.

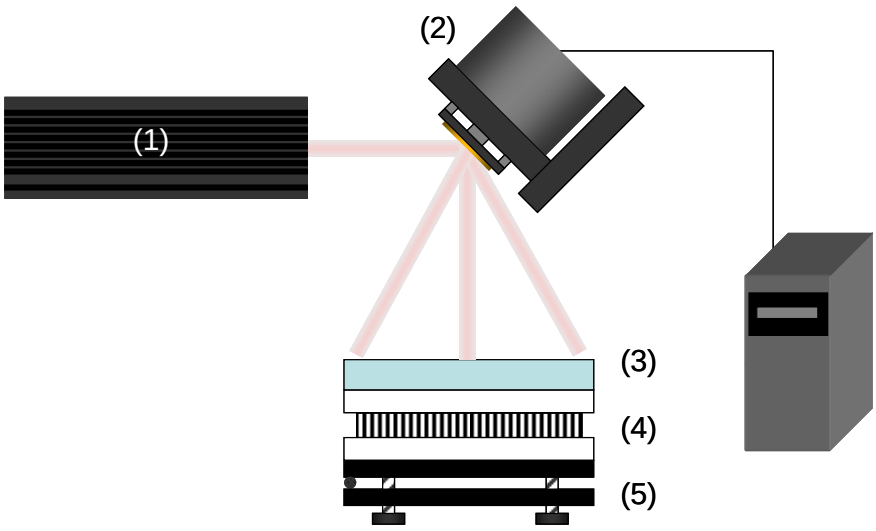


Figure 81. Schematic of an experimental apparatus used for droplet levitation and transport. A CO_2 laser is used for the heating of the silicone oil, and a steerable mirror is used to control the position of the laser beam on the glass surface.

The apparatus consists of the following devices:

1) A CO_2 laser (Synrad, Model No. F-48-1-115W) is used for transmission of energy in the infrared spectrum at a wavelength $\lambda = 10.6\,\mu m$. Silicone oil has good absorption around this wavelength, which helps to heat up the surface effectively and induce thermocapillary convection.

2) A steerable mirror (Optics in Motion, Model OIM101) is used to direct and guide the laser beam on the surface. The surface of the mirror, mounted on the device, is coated with gold in order to reflect the infrared laser beam effectively. The base of the steerable mirror accepts two voltage inputs to tilt the mirror about the *x*- and *y*-axis. LabVIEW is used to control these two voltage inputs simultaneously.
3) A glass (AFG Industries, Inc.) is used as the test platform, one side of which is coated with an indium-tin film and enables the surface to be grounded electrically.
4) A thermoelectric, Peltier module (Melcor Corporation, Model CP1.0-127-08L-1) cools the bottom side of the glass surface, and hence, the bottom of the levitated droplet.
5) A mirror mount (Newport, MM-2) levels the glass surface, since a slight inclination can cause a droplet to roll off under gravitational pull.
6) Silicone oils (Dow Corning, 200® Fluids) of 5 and 10 *cSt* kinematic viscosities have been used predominantly throughout the experiments since they are less volatile than lower viscosity oils.

Before levitating a droplet, the location of the heat source is marked using a heat-sensitive material, which changes color with temperature. Droplets are deposited at the marked position from the tip of a needle with ID = 0.152 *mm* and OD = 0.305 *mm* (Small Parts, Inc. Part # NE-301PL-C). The size of the droplets deposited in this manner is consistent in all the experiments, about 1.6 *mm* in diameter. This size is roughly an order of magnitude larger than what might be employed in an LOC application, but permits the levitation and translation demonstration to be performed. Further reductions in the droplet size cannot be accomplished using the deposition technique employed here. A systematic generation of smaller droplets (on demand) requires more sophisticated techniques, such as implementing piezoelectric materials to generate pressure-pulse trains at the tip of the capillary tube, as shown by Basaran (2002) and Chen & Basaran (2002). The present investigation, therefore, has not examined a droplet smaller than $O(1\ mm)$.

5.2. Demonstrations

5.2.1. Droplet Levitation and Controlled Delivery

Proof of the concept of droplet levitation and its delivery scheme are presented in this section. They provide the foundation for the use of levitated droplets in various engineering applications, such as LOC, discussed up to this point.

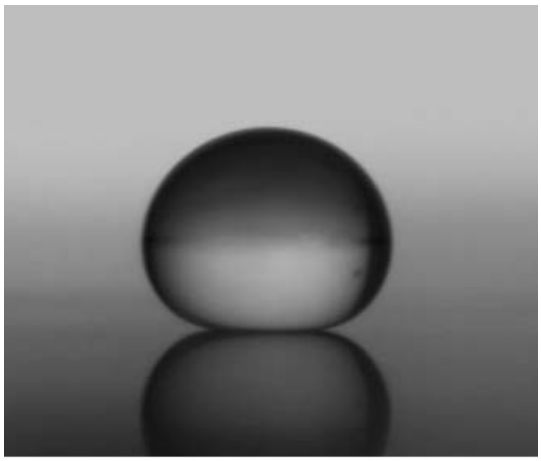
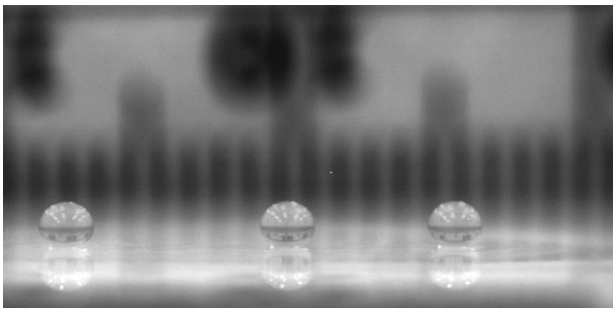


Figure 82. Droplet levitated above a glass surface. The viscosity is 5 *cSt* and the diameter of the droplet is about 1.6 *mm*.

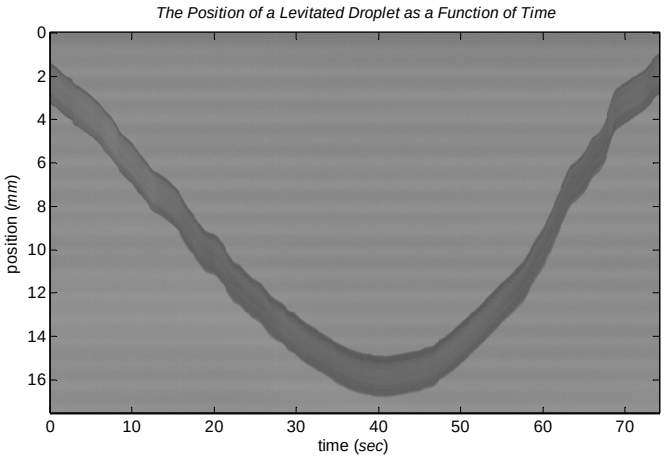
As shown in Figure 82, it is possible to levitate a droplet above a solid surface by using the mechanism of permanent nonwetting; the surface-tension gradient between the top and the bottom of the droplet, which is generated by heating from the laser and cooling from the thermoelectric module, drives the lubricating film. In this specific demonstration, the droplet of 5 *cSt* oil could be levitated for more than one hour. Several factors are suspected to cause such a stationary droplet to wet the surface. One factor is a dust particle that is swept into the contact region, thereby bridging the gap between the solid and liquid. Another factor is increased capillary pressure due to evaporation; the contact area, over which the lubricating film act, reduces as the shape of the droplet becomes more spherical due to the evaporation process.

By moving the laser beam off to the side of the droplet, the symmetry in thermocapillary convection is broken. As a result, more air is moved from the cooler end of the droplet's surface, resulting in a net propulsive force on the droplet towards the heat

source. Figure 83(a) shows an overlaid image of a translating droplet from three points in time (t = 0, 18.5, 37 *s* from left to right). A ruler with a millimeter scale behind the droplet provides the length scale within the image. The other plot in Figure 83(b) is the spatio-temporal representation, showing the 1-D path traversed by the droplet over the period of roughly 75 *s*. The droplet follows the motion of the laser beam, which moves in a sinusoidal fashion (with a frequency f = 0.01 *Hz*). A wobbly motion is observed during the translation, which may be due to transient air currents from the laboratory's HVAC system, or the droplet encountering a very thin film of oil remaining from previous experiments.



(a)



(b)

Figure 83. (a) Image showing a droplet from three instances in time. The positions of the droplet, from left to right, correspond to time at t = 0, 18.5, and 37 *s*. (b) shows the history of the droplet position, measured from the left edge of the image, as a function of time.

A simple analysis can be used to estimate the velocity and the acceleration of the droplet in Figure 83. A voltage input to the steerable mirror can be represented as

$$V = V_0 \sin(2\pi ft), \tag{54}$$

where V is the voltage, V_0 is the amplitude, f is the frequency of the voltage signal. Therefore, the position (X_d), the velocity (U_d), and the acceleration (a) of the droplet can be expressed, respectively, as

$$X_d = X_0 \sin(2\pi ft) \tag{55}$$

$$U_d = 2\pi fX_0 \cos(2\pi ft) \tag{56}$$

$$a = -4\pi^2 f^2 X_0 \sin(2\pi ft), \tag{57}$$

where, X_0 is the amplitude of the droplet's sinusoidal motion and f is the frequency input to the mirror. Using f = 0.01 *Hz* and the estimate $X_0 \sim 7$ *mm* obtained from the millimeter-scale in Figure 83(b), the maximum magnitudes of velocity and acceleration are $U_d \sim 0.44$ *mm/s* and $a \sim 0.028$ *mm/s*^{2} , respectively.

In addition to the 1-D translation demonstrated above, 2-D translations have been tested. In general, the laser beam can be traced out on a surface arbitrarily by controlling the voltage input to the mirror's *x* and *y*-tilting axes independently. For example, in order to trace out the shape of an ellipse on the surface, the input of the voltage functions to the mirror should have the form

$$V_{x,y} = V_{0x,y} \sin\left(f_{x,y}t + \phi_{x,y} \right), \tag{58}$$

where ϕ is the phase of the signal. Here, the subscripts, *x* and *y*, denote the mirror's tilt axis.

Using equation (58), two patterns are tested. The first test attempted to trace out a circular pattern, which is accomplished by setting $V_{0x} = V_{0y}$, $f_x = f_y$, $\phi_x = 0$, and $\phi_y = \pi/2$. Figure 84 shows the image sequence where a 5 *cSt* silicone oil droplet is

tracing out a circular path. Condensation from the heated droplet can be seen on the cooled surface, which helps to visualize the path taken by the droplet.

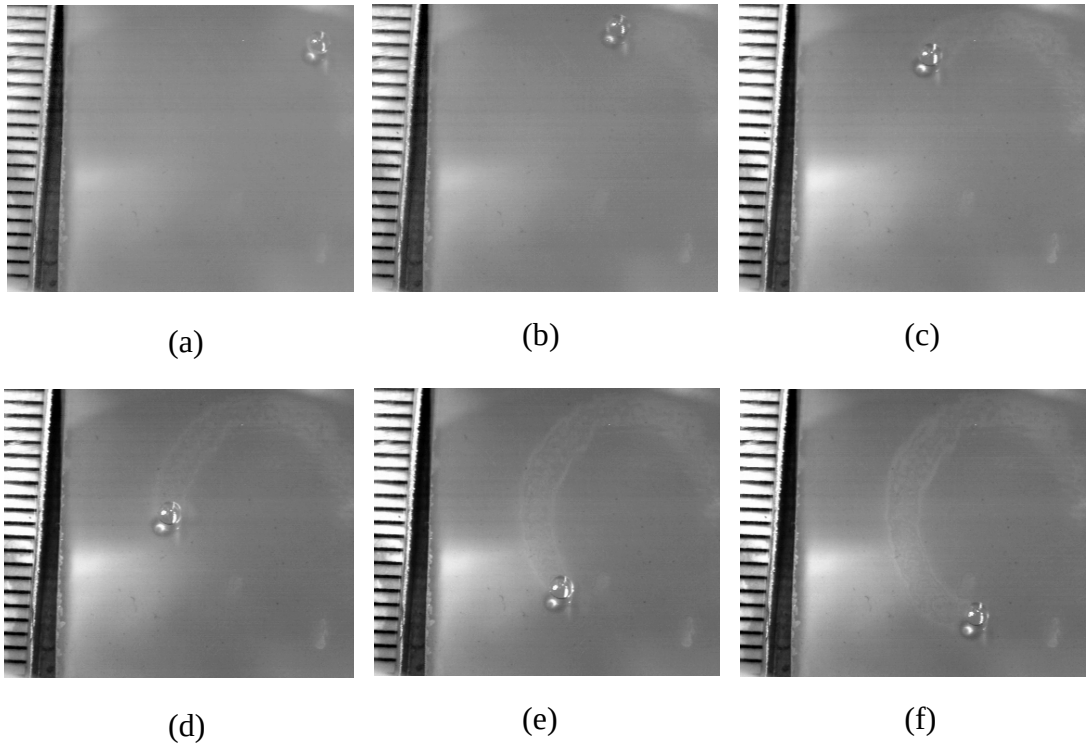


Figure 84. Image sequences (a)-(f) showing a levitated 5 *cSt* silicone droplet moving in a circular path. Condensation is observed on the cooled glass surface, which comes from the warmer levitated droplets.

The second pattern is the shape of the infinity symbol (∞), rotated by 90°, which is obtained by setting one of the frequencies to be twice that of the other, *e.g.*, $f_x = 2 f_y$. The image sequence in Figure 85 shows a 10 *cSt* silicone oil droplet tracing out the pattern. Again, condensation from the warmer droplet can be seen on the glass, helping to visualize the path traced out by the droplet.

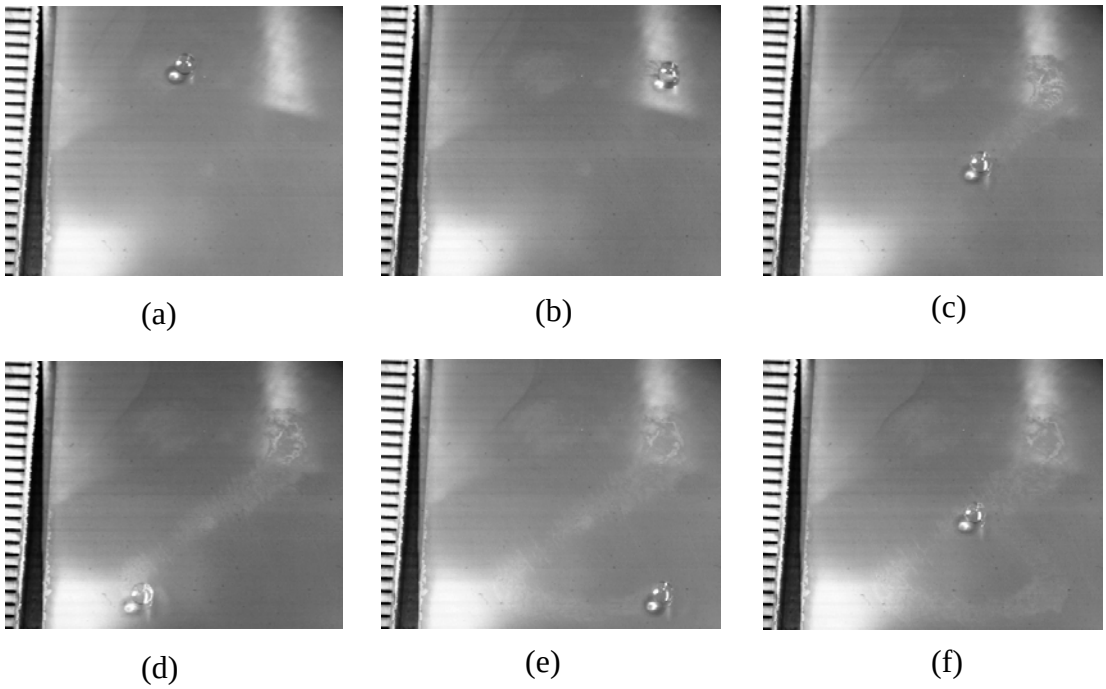


Figure 85. Image sequences (a)-(f) showing a levitated 10 *cSt* silicone droplet moving in a (∞) path, rotated by 90°. Again, condensation from the warmer droplet is observed on the cooler glass surface, helping to visualize the path.

These demonstrations show the versatility of the paths that can be traversed by a levitated droplet. The droplet can be placed to anywhere on a test surface depending on the demands of the laboratory test. In addition, the test surface does not require the use of channels, pipes, and chemical patterns for guiding droplets and liquids, eliminating any prefabrication of these features. Furthermore, the absence of mechanical pumps allows for easy system maintenance since they can be clogged by dust particles.

It is noted that the speeds of the droplets remained below 1 *mm/s* for these demonstrations. Several attempts have been made to move the droplet faster. For example, the energy flux from the laser was increased manually (through a knob-adjustment) or by reducing the beam size with a focusing lens while the beam was moved at a faster speed. Also, the intensity profile has been "artificially enlarged" by generating the wave form of a type

$$V_x = V_0 \cos(ft)$$
$$V_y = V_0 \cos\left(ft + \frac{\pi}{2}\right) + \xi t \,. \qquad (59)$$

By fixing V_0 at some value and setting f to a very high frequency in equation (59), the beam can be set to trace a circular pattern very quickly around the edge of a droplet. Through adjusting the speed parameter ξ, an attempt was made to move the droplet faster than previously. These attempts, however, have not been investigated systematically, and controlled translation at a speed faster than $O(0.1\ mm/s)$ has not been accomplished to-date.

One possible explanation for these translational speeds remaining low is due to radiative heating of the glass surface, resulting in a smaller, overall temperature-gradient across the droplet: Glass can be absorbing in the 10.6 μm wavelength of the infrared laser employed. Due to this effect, the overall temperature-gradient between the heated region on the droplet's free surface and the warmed-up glass surface would be small, resulting in reduced temperature asymmetry, and thus smaller propulsive force. In order to minimize such effects, the bottom surface could be replaced with a material with higher infrared transparency, or ways to enhance heat-transfer of absorbed energy from the region of the droplet could be explored. The use of diamond, which is an effective infrared transmitter with a high thermal conductivity, would be well suited.

5.2.2. Notes on the Translational Speeds

Although the successful demonstrations yielded the translational speeds of $O(0.1\ mm/s)$, multiple observations confirm that a *mm*-scale droplet can achieve speeds of $O(1\ mm/s)$ and higher. Once the incident energy exceeds some threshold value, a levitated droplet can be set into a quick, uncontrollable, and autonomous oscillation about the heat source.

This oscillation can be explained by constraints imposed by the present apparatus and with a help of the sketch in Figure 86. As seen in the sketch, the diameter of the laser beam (~ 3 *mm*) is larger than that of the droplet (~ 1.6 *mm*). As a result, the energy

distribution from the laser leads to the establishment of a temperature gradient spanning across the diameter of the droplet. As the temperature gradient become large, a proportionally large propulsive force is generated due to the vigorous nature of the induced thermocapillary motion and the mass-flux of the air. The droplet placed on the "left" of the beam as in Figure 86 is therefore accelerated very rapidly towards the center of the beam. If the momentum of the droplet is large enough, the droplet can overshoot the center of the beam, while thermocapillary convection is shifted on the "right" side of the beam. The resultant propulsive force opposes the momentum of the droplet, decelerating it and finally changing the direction of the droplet's motion to push it back to the center of the heat source.

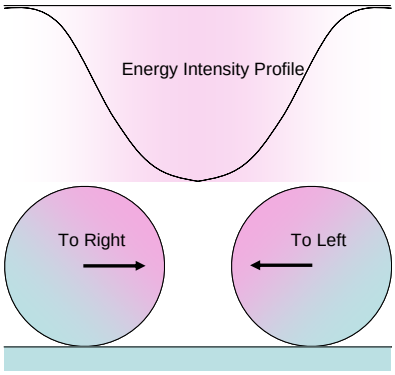


Figure 86. Sketch of a levitated droplet oscillating about the heat source. The intensity profile of the laser beam is approximately Gaussian. The diameter of the beam is ~3 *mm* where as the droplet is ~1.6 *mm*.

This process repeats, unless the system configuration is changed, leading to either a decay or a growth of the oscillation. The amplitude of the oscillation can be reduced by reducing the energy input to the droplet. This is the primary method used in the experiment to reduce the amplitude of oscillation, since this type of oscillation is not desired for levitation. In addition, evaporation can also lead to a decay of the oscillation, since the mass and thus, the inertia of the droplet is reduced through the process. On the other hand, the amplitude of the oscillation can grow very rapidly with a slight increase in the energy flux, throwing the droplet off from the heat source. When the droplet is displaced from the energy source, it wets the surface eventually as the strength of

thermocapillary convection is reduced by achieving thermal equilibrium with the surface below.

5.3. Analysis of Levitated-Droplet Oscillations

Several instances of the oscillatory motion have been recorded from the experiments. These recordings have been used to determine the velocity and accelerations of the droplet and show that they can exceed the average speeds and accelerations attained from controlled-delivery experiments. The acceleration attained during the oscillatory motion has agreed well with that of the estimate calculated from the order-of-magnitude analysis discussed in Chapter 1. The image analysis from this section supports the idea of delivering a levitated droplet a speed above 1 *mm/s*.

The following analyses are done by tracking the positions of the droplet in the recording. Two separate recordings have been captured; one corresponding to a continuous oscillation of a droplet and another to a situation where a droplet is "thrown off" from the heat source after its intensity is increased. As mentioned earlier, the droplet can be set into an oscillatory motion as some threshold value in the incident energy flux is surpassed. Further increase in the energy from this condition results in a droplet being thrown away from the heat source.

5.3.1. Continuous Oscillation of a Droplet

The first analysis shown in Figure 87 is for a droplet oscillating continuously about the heat source. The image in Figure 87(a) shows the first of the image sequence from the recording, which defines the coordinate system employed for the analysis. The positions of the droplet are decomposed into *x*- and *y*-components, and the data are fitted by a spline function. The frame rate of the recording (5 *Hz*) is sufficiently high that the overall characteristic of the droplet motion is not lost between the image sequence. As seen from the data of the droplet's position, the oscillation is not purely sinusoidal; this may be due to a slight misalignment in the level of the glass surface, an intensity profile

deviating from Gaussian distribution, and the presence of air currents, among other possible problems.

The velocity and acceleration are calculated from the spline-fitted functions of the raw data. The droplet attains a maximum velocity and acceleration of about 5 *mm/s* and 20 mm/s^2, respectively. As a matter of fact, the value of acceleration matches with an estimate evaluated from a control volume analysis in Chapter 1, with $O(10\ mm/s^2)$.

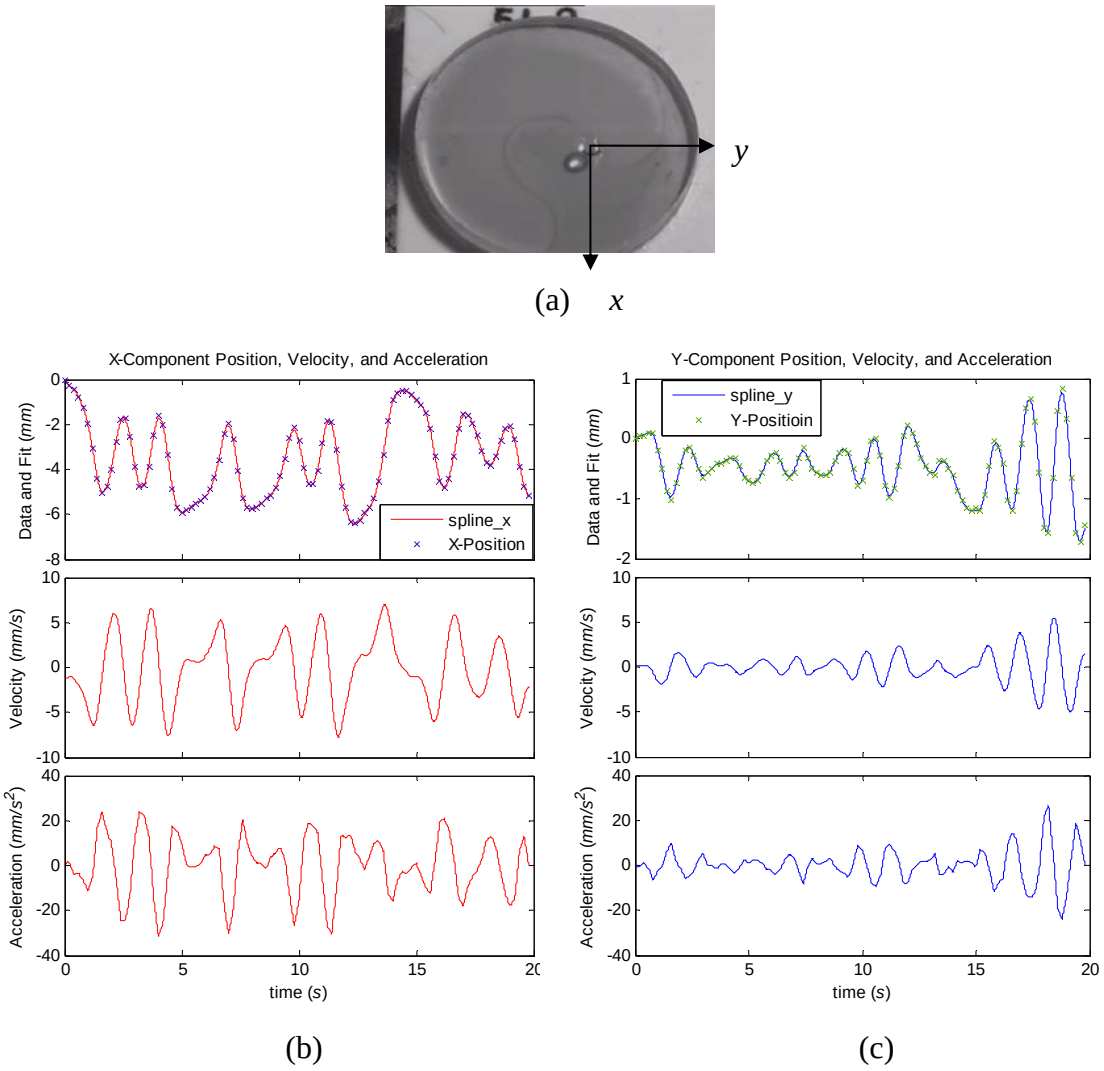


Figure 87. Image analysis of the droplet's oscillatory behavior. (a) The original image from the recording used to define the coordinate system. Data corresponding to the droplet's; (b) x-component of the position, velocity and acceleration and; (c) y-component of the position, velocity and acceleration. The spline function is used to fit the raw position data for velocity and acceleration computations.

5.3.2. Droplet Moving Away from the Heat Source

Another recording is taken from an instance in which a droplet moves away from the heat source as it receives excess energy. Figure 88 shows the results from the image analysis with the same procedure as described in the previous section. Figure 88(a) and (b) show the coordinate system defined in the analysis and the tracked positions of the droplet, respectively. The interval between the dots in Figure 88(b) is 1/30 *s*; a wide gap between the dots means that the droplet is moving quickly. Starting at $(x,y) = (0,0)$ at $t = 0$ *s*, the position vector of the droplet is decomposed into *x*- and *y*-components and they are plotted in the top graph of Figure 88(c). These raw data points are fitted with arbitrary functions, which are then used to compute the velocity and acceleration of the droplet. These results are presented in the second and third graphs of Figure 88(c).

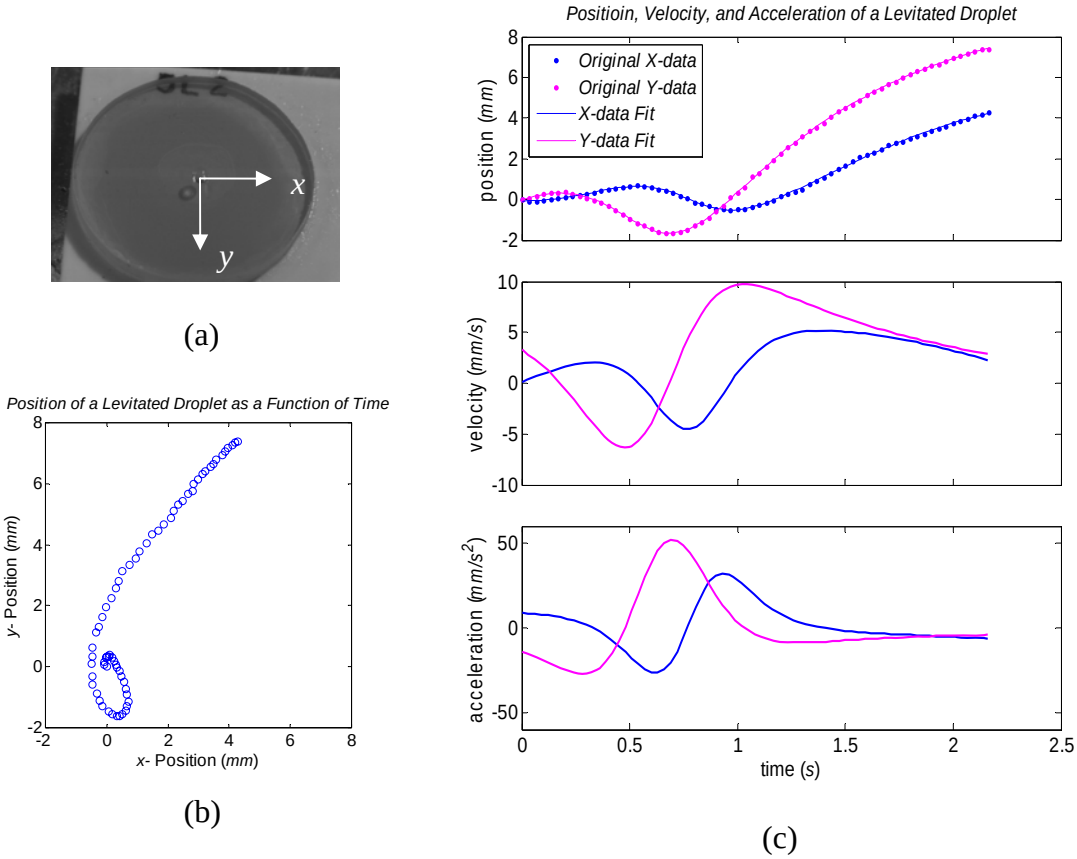


Figure 88. Plots showing position, velocity, and acceleration of a droplet heated above some threshold value. As a result of overheating, the droplet is accelerated and escapes from the heat source. (a) shows the coordinate system used for the image analysis. (b) plots the positions of droplet as a function of time, starting at (*x*,*y*) = (0,0). (c) shows the *x*- and *y*-components of the position, velocity, and acceleration of the droplet as a function of time. The position data are fitted and they are used to compute the velocity and acceleration.

As can be interpreted from the trajectory in Figure 88(c), the droplet changes the direction of its motion around $t \sim 0.25\ s$, and moves towards the heat source located somewhere near (0,0). After passing through the regions of high energy intensity, the droplet turns back around again at $t \sim 0.75\ s$ due to the reversal of thermocapillary convection. As the droplet moves back towards the regions of high energy flux, the intensity of the laser is increased manually, resulting in the droplet attaining a velocity $\sim 10\ mm/s$ at $t \sim 1.0\ s$. This is about twice the momentum attained in the previous cycle at $t \sim 0.5\ s$. Eventually, the droplet having such a large momentum is driven away from the heat source due to an insufficient force to push the droplet back towards the center of the energy profile again.

These analyses show that the droplet can achieve a velocity of ~10 *mm/s*, which is two orders of magnitude larger than the velocity achieved during the controlled delivery experiment presented earlier. It is likely that the delivery of a droplet can be manipulated at this speed by incorporating feedback of its positions to the steerable mirror. Further physical understandings are necessitated in order to accomplish such translational speed.

5.3.3. Simple Model of Droplet Oscillation

An analysis is carried out to model the autonomous oscillations of a levitated droplet around the heat source. The simple model derived in this section is useful for understanding the effects of relevant physical parameters on the oscillatory behaviors without resorting to full CFD computations.

In this 1-D model, the intensity profile from the laser output is assumed to be 1-D Gaussian, given by

$$I(x) = \frac{I_0}{S_x / L} \exp\left(\frac{-x^2}{2S_x^2}\right), \qquad (60)$$

where x is a distance measured from the center of the beam profile, $I(x)$ is the intensity distribution (per unit length), I_0 is the amplitude of the intensity at the center of the beam, L is the radius of the beam, and S_x is the standard deviation that characterizes the width of the Gaussian distribution. The integral over the region from $x = -\infty$ to $+\infty$ is, by definition, the total flux from the laser.

A droplet placed in this energy field is heated, inducing a temperature variation on the free surface and hence the surface-tension gradient due to thermocapillarity. It is assumed here that the variation of surface tension follows that of the temperature distribution on the droplet, which should be proportional to the incident energy flux from the laser beam. The surface-tension gradient thus varies in accordance with the gradient of the intensity field, and it depends on the location of the droplet within the energy field. Such variation can be argued from the first and second derivatives of the intensity profile

$$\frac{dI}{dx} = -\frac{I_0 L}{S_x^3} x \exp\left(\frac{-x^2}{2S_x^2}\right) \tag{61}$$

and

$$\frac{d^2 I}{dx^2} = \frac{I_0 L}{S_x^3} \exp\left(\frac{-x^2}{2S_x^2}\right)\left(\frac{x^2}{S_x^2} - 1\right). \tag{62}$$

Due to the symmetry of intensity profile, the gradient of the surface tension is effectively zero when the droplet is placed at the center of the beam (x = 0). The gradient approaches a maximum ($d^2 I / dx^2 = 0$) as the position of the droplet approaches S_x and decreases again towards the edge of the profile as $x \to L$.

The present model assumes that the droplet has a perfect thermal response. This is characterized by thermal equilibrium instantaneously attained by the droplet at each location within the energy field, *i.e.*, $T(x) \propto I(x)$. Following the expression of the laser intensity, the temperature on the droplet as a function of its position can be expressed as

$$T(x) = \frac{\Delta T_0}{S_x / L} \exp\left(\frac{-x^2}{2S_x^2}\right), \tag{63}$$

where ΔT_0 is an arbitrary temperature difference between the droplet and the cold plate at the center of the beam.

The surface-tension gradient generates thermocapillary convection, which moves the surrounding gas around the droplet and generates a net mass flux from the trailing edge of the droplet, resulting in propulsion. Due to thermocapillarity, the gradient of surface-tension is proportional to the gradient of the temperature distribution

$$\nabla_s \sigma = \gamma \nabla_s T \sim \gamma \frac{dT}{dx}, \tag{64}$$

where ∇_s is the surface gradient, γ is the temperature coefficient of the surface tension. In order to estimate the speeds on the free surface and that of the jetted air driven by the free-surface motion, the tangential stress balance is applied at the liquid-gas interface, *i.e.*,

$$\nabla_s \sigma \sim \frac{\mu_l U_s}{R_d}. \tag{65}$$

In equation (65) μ_l U_s, and R_d are the viscosity, the free surface velocity, and the radius of the liquid droplet, respectively. Using equations (63)–(65), the expression for the free-surface speed is obtained as a function of position x within the energy field having a Gaussian distribution (equation (60))

$$U_s(x) \sim \frac{\gamma \Delta T_0}{\mu_l} \frac{R_d L}{S_x^3} x \exp\left(-\frac{x^2}{2S_x^2}\right). \tag{66}$$

The net flow of gas emitted from the trailing end of the droplet is assumed to be of the same order of magnitude as the surface velocity, therefore equation (66) is used for the estimate. Furthermore, the velocity profile of the gas is assumed to be uniform having a projected area the same as that of the droplet. The momentum flux generated from the gas is then equal to the force applied on the droplet, taking the same form as equation (4):

$$F = \rho_g U_s^2 \pi R_d^2 \tag{4}$$

A small but finite drag force is present on a droplet that is moving in the air. The droplet with a 1.6 *mm* diameter moving at the velocity of 10 *mm*/*s* in the air has a Reynolds number ~ 1, which is a viscously dominated regime. By applying the Stokes Law, the drag force F_{drag} for is given by

$$F_{\text{drag}} = 6\pi \mu_g R_d U_d \tag{67}$$

where μ_g is the viscosity of the surrounding medium, and U_d and R_d are the velocity and the radius of the droplet, respectively (Batchelor (1967)). The law, however, does not directly apply to a levitated droplet; its drag force must be smaller than the one on a solid sphere, assumed by equation (67), due to the presence of free-surface motion driven by thermocapillary convection. An analogy can be found as the reduced drag on a droplet settling in another fluid medium due to the presence of Hill's vortex (Hill (1984), Garner & Haycock (1959)). Assuming that the drag force to be viscously dominated, the following expression is used

$$F_{\text{drag}} = C_1 \mu_g R_d U_d \,, \tag{68}$$

where the magnitude can be adjusted by varying the coefficient C_1. The upper bound on the drag force should be $C_1 = 6\pi$ as the case for the Stokes law of a solid sphere. The value is expected to be smaller than 6π in the case of a levitated droplet with the presence of thermocapillary convection.

The equation of motion is obtained from Newton's 2nd Law,

$$\rho_l \frac{4}{3}\pi R_d^3 \frac{dU_d}{dt} = -C_1 \mu_g R_d U_d - \text{sgn}\left(x\right)\left(\rho_g U_s^2 \pi R_d^2\right) \tag{69}$$

where U_d is the velocity of the droplet and U_s is the speed of the jetted air defined in equation (66). The signum function (sgn) in equation (69) is defined as

$$\text{sgn}\left(x\right) = \begin{cases} -1 & x < 0 \\ 0 & x = 0 \\ 1 & x > 0 \end{cases}, \tag{70}$$

which is necessary for the "forcing" term (last term in equation (69)) to push the droplet in the positive (negative) x-direction when it is positioned at $x < 0$ ($x > 0$), in an accordance with the directions of the net propulsive force. After a rearrangement, the governing equation for the motion of the droplet can be expressed as

$$x'' + \frac{3C_1 \mu_g}{4\pi \rho_l R_d^2} x' = -\text{sgn}\left(x\right) \frac{3\rho_g}{4\rho_l R_d} U_s^2\left(x\right), \tag{71}$$

which is a 2nd order, nonlinear ordinary differential equation. In equation (71), μ_g is the viscosity of gas, ρ_l and ρ_g are the densities of the droplet and gas, respectively, R_d is the radius of the droplet, U_s is the speed of jetted gas, and the superscripts denote the time derivatives.

The ratio of the drag and the propulsive forces

$$\frac{Drag}{Forcing} = \frac{C_1 \nu_g}{\pi R_d U_s^2}, \tag{72}$$

shows an important characteristic of the dynamics involved. Using the relationship in equation (66), which states that the free surface speed is proportional to the size of a droplet, *i.e.*, $U_s \propto R_d$, the ratio in equation (72) can be shown to be inversely proportional to the cube of the droplet radius,

$$\frac{Drag}{Forcing} \propto R_d^{-3}. \qquad (73)$$

The drag force becomes more dominant over the forcing as the size of the droplet radius become smaller. Therefore, the oscillatory behavior as discussed in the previous sections is not expected from a tiny (e.g., *nL*-scale) droplet to be employed in the LOC applications.

Yet unknown in the problem are the characteristics of the beam intensity profile and the induced temperature on the free surface of a droplet. In order to fully characterize these properties, the beam-intensity profiler and infrared thermo-camera are required, but are not available for the present research. Instead, reasonable estimates are employed by using following physical arguments. First, the beam diameter is estimated from the size of a molten region on an acrylic sheet, created by the heating from the CO_2 laser. The diameter of the molten region is roughly 3 *mm*, therefore it is argued here that the intensity profile has the radius L = 1.5 *mm*. In addition, the standard deviation, which characterizes the waist of the beam, is assumed to be $S_x = 1\,mm$. Furthermore, the temperature difference (ΔT_0) is assigned an arbitrary value of 30 °C, which is about the same magnitude as used in the permanent nonwetting experiments and sufficiently lower than the boiling point (134 °C for 5 *cSt* oil).

The initial conditions prescribed for the system are $(x, x') = (1\,mm, 0\,mm/s)$. MATLAB's ODE solver (ode15s) is used to solve the governing equation for the dynamics of an oscillating droplet. Properties of 5 *cSt* silicone oil and air (at room temperature) have been used throughout the following discussions.

Figure 89 shows the result in the time interval $t = [0, 30]$ *s*, with the drag constant $C_1 = 6\,\pi$, corresponding to the solid sphere case. The oscillation exhibits the

characteristics of an underdamped system, where the energy of the oscillation is gradually dissipated over the many cycles of the oscillation.

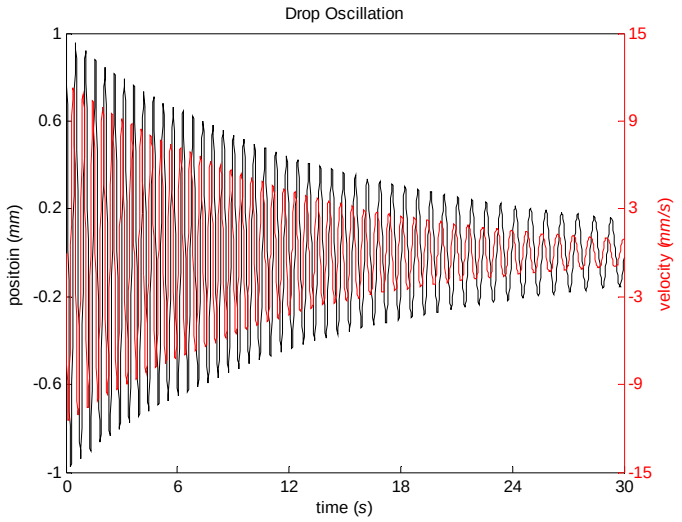


Figure 89. Result of the droplet dynamics around the heat spot. The Stokes drag is used for the present analysis. The system shows characteristics of an underdamped oscillation.

The next simulation is carried out using $C_1 = 4\pi$, instead of 6π. The droplet now has a smaller drag force, which argues for a levitated droplet with thermocapillary convection within. With the same initial conditions as the previous case, the dynamics presented in Figure 90 show less effective damping as indicated by a larger velocity (and the kinetic energy) of the droplet at the end of the integration time $t = 30\ s$.

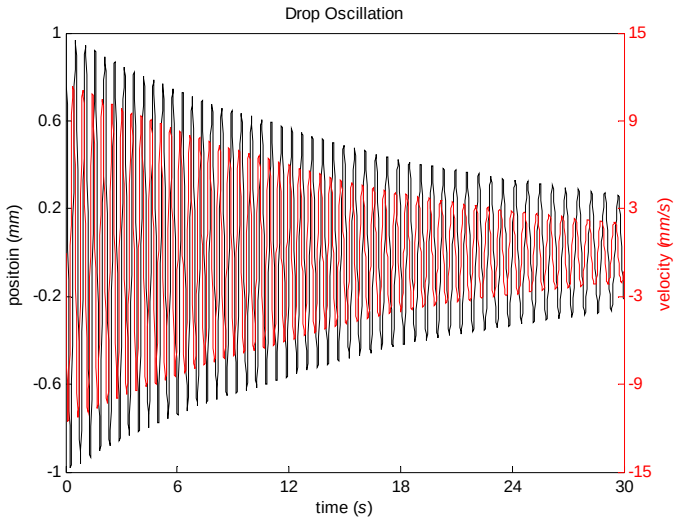


Figure 90. Result of the droplet dynamics around the heat spot. The drag coefficient is adjusted to $C_1 = 4\pi$. The system exhibits less effective damping than the one with the Stokes drag, indicated by higher velocity at the end of integration period, $t = 30$ s.

According to the present model, the amplitude of the oscillation decays over time, contrary to the experimental observations. The oscillation is observed to persist over an extended time, and the amplitude of the oscillation does not seem to decay (see Figure 87). The reason for this discrepancy seems to stem from perfect thermal-response of the droplet, where the temperature gradient on its free surface is presumed to follow precisely the intensity gradient of the laser beam. However, due to the complex nature of the heat transfer on the free surface of droplet, it should take a finite time for the temperature to respond to the energy flux.

The sketch in Figure 91 is used to describe possible mechanisms behind the continuous oscillation of the droplet. In the sketch, two droplets with perfect and imperfect thermal responses are released from the same location at (1) after they have reached a steady state. As the droplets accelerate and approach the center of the energy profile at position (2), the force vector (indicated by the arrows) on the **perfect** droplet becomes zero due to the zero temperature gradient there. On the other hand, the imperfect droplet has a finite force vector pointing in the positive *x*-direction, because the temperature has not yet adjusted to the new energy flux at this location. This delay in thermal response may arise due to radiative and convective heat-transfer inside and

outside of the droplet that have not been modeled in the present analysis. At location (3), the force vector on the perfect droplet points towards the center of the beam profile, whereas it is still pointing away from the center for the imperfect droplet. If the right conditions are met, the imperfect droplet would be pushed slightly further into the opposite side of the energy field, adding energy to the droplet and compensating for the energy loss due to the viscous drag.

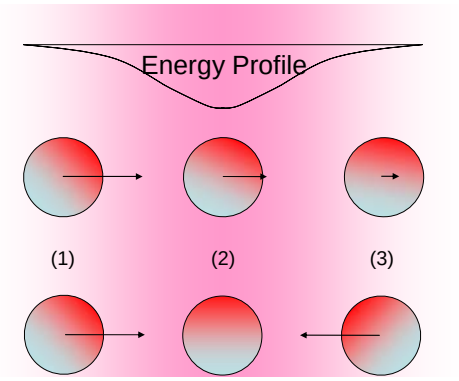


Figure 91. Drawing showing droplets with perfect (bottom) and imperfect (top) thermal responses. The arrows indicate the forcing vectors as a function of three positions. The forcing on the perfect drop switches the sign as it passes $x = 0$, whereas a delay is expected for a realistic droplet.

The delay in the thermal response is expected to influence the dynamics more prominently as the translational speed of the droplet increases. By receiving a high energy flux from the laser, the magnitude of the force becomes large as well, resulting in a large momentum of the droplet. If the time scale of the translation becomes sufficiently greater than that of the temperature response, thermocapillary convection may not have an adequate time to shift. As a result, the droplet may overshoot from the center of the beam while carrying a high momentum pointed away from the heat source. This argument may explain the observation in Figure 88, where the droplet escapes from the energy source after receiving a high energy flux during its return to the center of the heat source.

In order to incorporate the time-delay effect, the temperature on the droplet is "lagged" by an appropriate distance behind the current position. This is done by transforming the coordinate system of the temperature on the droplet

$$\hat{x} = x - U_d(x) C_2 t_\theta , \qquad (74)$$

where $\hat{x}$ and x are the transformed and current positions of the droplet, respectively, U_d is the velocity of the droplet at x, C_2 is a constant with a value of $O(1)$, and t_θ is the time constant characterizing the thermal response. The coordinate transformation of equation (74) is sketched in Figure 92. Here, t_θ is assumed to be of the same order of magnitude as the convective time scale, $t_\theta \sim R_d / U_s = R_d \mu_l / \gamma \Delta T_0$ = 1.8 *ms* for a 5 *cSt* oil droplet with R_d = 0.8 *mm* at ΔT_0 = 30 °C. The product of C_2 and t_θ determines the sluggishness of the thermal response.

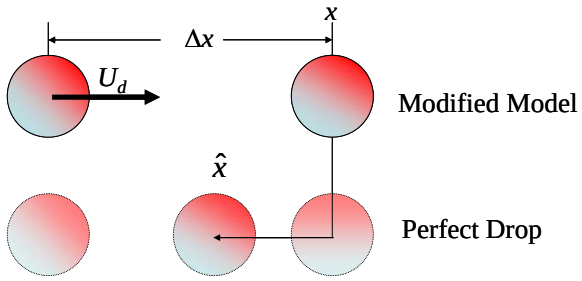


Figure 92. Transformation of droplet position used for the modified model. The modification mimics the latent thermal response of an actual droplet.

The result in Figure 93 shows an output from the modified model for the time interval $t = [0, 30] s$, with the characteristic time scale t_θ =1.8 *ms* with C_2 = 1.0. All the other parameters and initial conditions remain the same with the Stokes law for the estimate of the drag force. The oscillation does not decay in this model; the amplitude increases in the interval $0 \le t \le 20\, s$ and stays the same afterwards. It is noted that for a system with relatively quick thermal response with $C_2 < 0.5$, the oscillation is damped out and the resulting dynamics become similar to that of the perfect droplet.

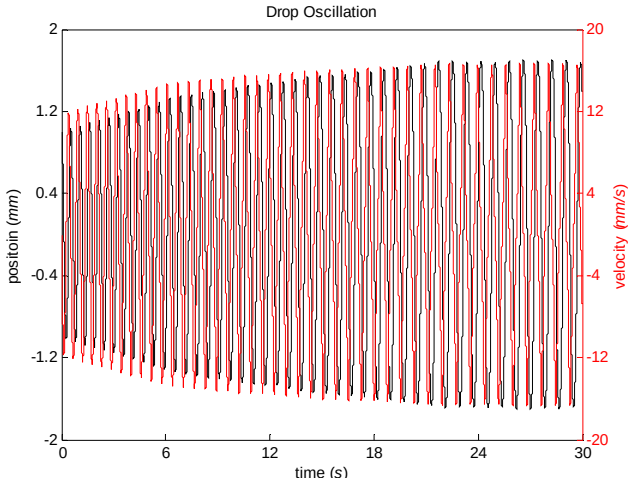


Figure 93. Result from the modified model. Due to the delayed thermal response, the droplet is set into a continuous oscillation.

In addition, a droplet with more sluggish response ($C_2 \geq 1.7$) is driven away from the heat source and never returns to the oscillatory behavior. This result is shown in Figure 94 for C_2 = 1.7. In this result, the amplitude of oscillation is gradually amplified over the first 20 *s*, by maintaining sufficient propulsion to push itself back to the center of the intensity profile. As the amplitude of the oscillation approaches the radius of the beam (L = 1.5 *mm*), where the jetting of air is small, there is no sufficient force to push the droplet back to the center. As a result, the droplet is finally thrown away from the intensity profile.

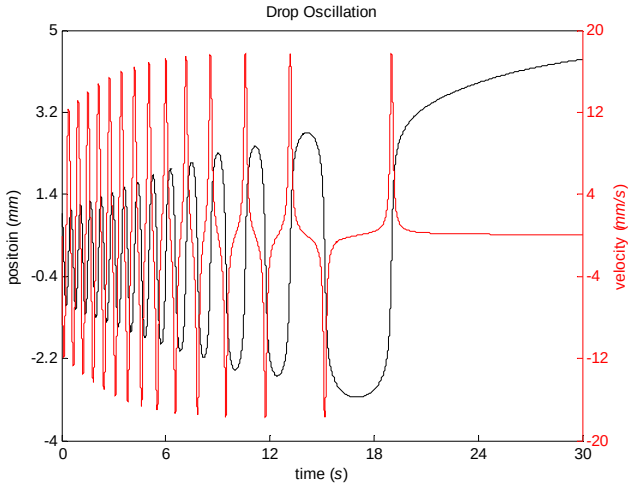


Figure 94. Simulation of a droplet with a sluggish thermal response (C_2 = 1.7). The droplet escapes from the energy source and never returns to oscillation.

Finally, a computation was performed to simulate a sudden temperature increase, ΔT_0 = 30 to 40 °C at t = 20 s in order to mimic the experiment shown in Figure 88. The simulation used $C_1 = 6\pi$ (Stokes drag) and C_2 = 1.0 and the result is presented in Figure 95. Accompanied by the sudden increase in the temperature at t = 20 s, there is a sudden jump in the velocity, and the amplitude of the oscillation increases gradually over the next few oscillations. As the droplet is displaced away from the center, the momentum flux of the gas is not sufficient to keep changing the increased momentum of the droplet. As a result, the droplet is driven away from the heat source, never to return to the oscillatory motion.

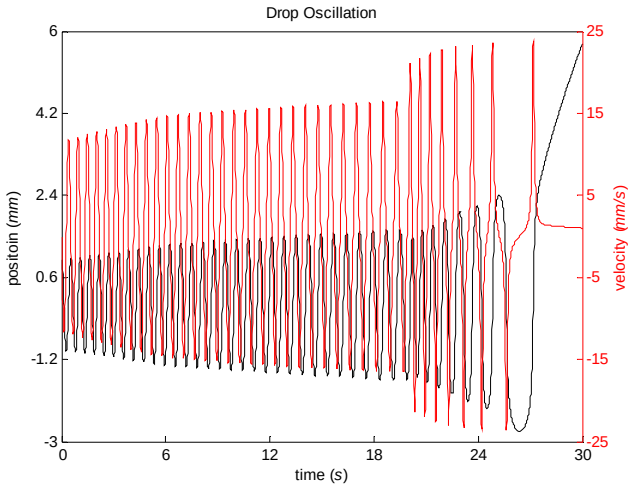


Figure 95. Simulation where a droplet diverts from the heat source after a sudden increase in the energy input at t = 20 s. The increase in the energy is imitated by an increase in the value of ΔT_0 = 30 to 40 °C. The model uses the Stokes drag law and C_2 = 1.0 for the thermal response.

These analyses are based on approximations, assumptions, and adjustments made to mimic the dynamics of the droplet oscillations observed in experiments. Although the model is not founded on sound physical arguments and other mechanisms may also come into a play to influence the dynamics, it seems to capture basic characteristics of the droplet oscillations, with qualitative agreement with experimental observations. It is suspected that further adjustments to the parameters can be incorporated into the model by comparing the output to experimental results, improving the present model. It is hoped that such improved model, though simple, may be used to further characterize motions of the droplet under different system configurations, *e.g.*, different and/or

moving intensity profiles, smaller droplet sizes, *etc*., without resorting to computationally expensive CFD.

5.3.4. Discussion

The experimental setup from the present studies has achieved speeds of $O(0.1\ mm/s)$ for the controlled delivery of a levitated droplet. One possible explanation for such low speed has may be due to the heating of the glass surface, which effectively reduces the temperature gradient across the droplet, reducing the effective propulsive force. As opposed to these slow motions, a faster delivery of droplets is desired in LOC systems. Based on the multitudes of observations during the oscillatory motion, a levitated droplet shows its capability to translate at a speed $O(1–10\ mm/s)$. Images from recordings, captured during the droplet oscillations, have been used to calculate velocities and accelerations that are well above the values achieved from the controlled delivery experiments. It is suspected that the controlled delivery scheme will be capable of achieving these speeds and accelerations only by gaining more detailed knowledge of the influence that various system parameters have on the dynamics of a droplet. A 1-D model is constructed in this perspective, enabling various parameters of the dynamics to be adjusted. Although not constructed from first principles with all potential influences present, the results from these models agree qualitatively with the experimental observations, where a droplet is set into continuous oscillation and escapes from the heat source by receiving a high energy input. This simple model may be improved by adjusting the system parameters to incorporate experimental data, instead of basing them on simple observations. In the end, the model may be used to capture behaviors of a levitated droplet under various input parameters, such as magnitude, size, flux, profile, and the motion of the heat source without resorting to a full CFD analysis.

5.4. Encapsulation

The delivery of a sensitive specimen, protected within a layer of another immiscible liquid, provides a contamination-free environment, for the inner droplet is not exposed directly to the atmosphere. Specifically, the encapsulation of an aqueous

solution, which is commonly used as a DNA carrier, is of practical interest for LOC applications due to the nature of tests requiring minimal cross-contamination.

A compound droplet system, in fact, can be levitated as shown in the image of Figure 96. In this image, a tiny water droplet could be encapsulated within a larger 10 *cSt* silicone oil droplet by spraying water mist from above the levitated droplet. Although hundreds of droplets are produced by a use of the spray, some of them fall onto the levitated droplet and are engulfed within the silicone oil, coalescing to form an internal droplet of the given size. It is noted here that this particular method performed for this experiment simply demonstrates the ability to levitate such a compound droplet, and it is not a suggested method for an LOC application. Instead, a merger of the hydrodynamic focusing technique of Utada, *et al.* (2005) and the drop-on-demand technique of Chen & Basaran (2002) are considered to be useful for generating a compound drop system with various volume ratios between inner and outer droplets.

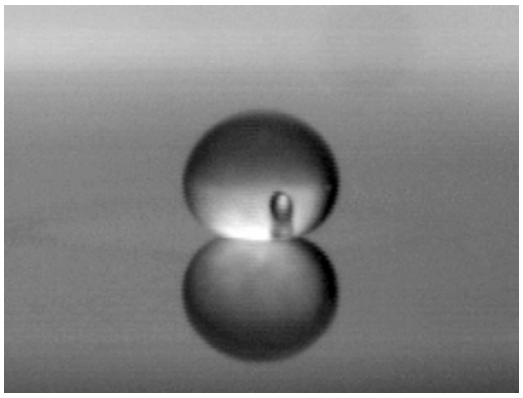


Figure 96. An encapsulated water droplet within a levitated 10 *cSt* silicone oil droplet.

The diameter of the levitated, silicone-oil droplet is roughly 1.6 *mm* and the diameter of the inner, water droplet is estimated to be ~ 200 μm. Due to its small mass, the water droplet is observed to follow thermocapillary convection. The circular path, traced by the droplet, has a period of ~ 0.13 *s*. This time scale provides the sense of the surface speed using the argument, $U_s \sim R_d / t$; with the period $t = O(0.1\ s)$, the free-surface speed of the droplet with the radius $R_d = O$ (1 *mm*) is O(10 *cm*/*s*). Furthermore, thermal-Marangoni velocity-scale can be used to argue that the temperature difference is

$\Delta T \sim \mu_l U_s / \gamma$ = 10 °C between the top and bottom regions of the levitated droplet. This temperature difference, in fact, is a reasonable estimate, given that it is an order of magnitude below the boiling point of silicone oil.

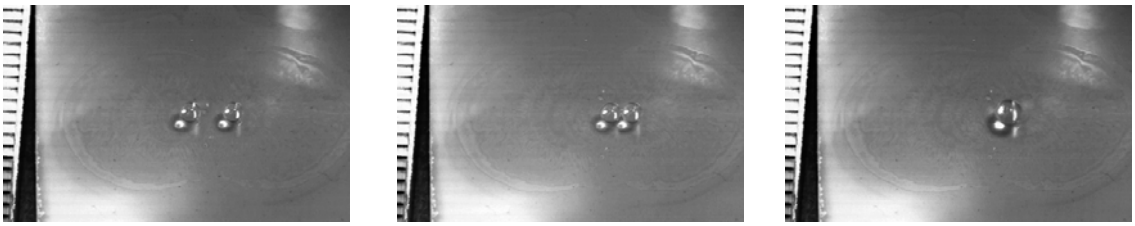
In order to realize the compound system shown above, the size of the inner droplet must be sufficiently small compared to that of the outer one. Attempts to inject larger droplets into levitated silicone-oil droplets have led to instances of immediate wetting. The reasons for this may be attributed to a higher density of water that effectively increases the mass of the compound-droplet system to the point where the lubricating film fails to support its weight. It suspected that the ratios of the volumes between the inner and the outer droplets play an important role in realizing the compound droplet systems. As the size of the encapsulating droplet becomes smaller, surface forces become more dominant, and the density mismatch should not matter as much. This will hopefully permit us to generate levitated, compound droplets containing a larger fraction of water, which is certainly a concern if levitated droplets are to be combined and their contents mixed. This is one of the parameters that future research is expected to investigate.

5.5. Levitated Droplet as a Mixing Chamber

One of the goals of LOC application is to mix two samples of liquid together. A general challenge exits, however, to mix liquids in LOC due to its viscously-dominated environment; an absence of turbulence makes the system an inefficient mixer. At a low Reynolds-number regime, efficient mixing can be achieved by a multitude of steps of stretching and folding the liquids, reducing constituent length scales to the point where diffusion can occur rapidly. In this regard, strong thermocapillary convection, present within a levitated droplet, may provide an effective environment to mix encapsulated droplets.

An experiment has been carried out to bring two levitated droplets together, simulating the operation necessary to merge two (or more) encapsulated droplets (Figure 97). In this experiment, a single laser head is used to levitate two droplets simultaneously by switching the locations of the heat spot between the droplets. This is accomplished by

feeding the step-function into the steerable mirror's input. These droplets were brought together by reducing the amplitude of voltage supply.



(a) (b) (c)

Figure 97. Merging of two levitated droplets, demonstrating a possible use of the coalesced droplet as a mixing chamber. A step function is used to levitate two droplets simultaneously, where the amplitude of the voltage is reduced to approach them together as seen in (a)-(c). The droplets are observed to oscillate about the heat spot due to an excess energy received from the laser. This oscillation is minimized by reducing the energy input.

Prior to the coalescence sequence shown in Figure 97(c), these droplets went into oscillatory motion. As discussed in Section 5.3.1, such oscillation can occur if a droplet receives too much energy from the heat source. As the droplets in Figure 97 were brought closer together, each one received additional energy from the hot spot that is intended for the other droplet. In order to minimize the oscillatory behavior, the energy input was manually reduced. The droplets were brought into apparent contact, as shown in Figure 97(b), at speeds less than 0.1 *mm/s* and in a near head-on collision. These two droplets, however, did not coalesce immediately. Instead, they moved and slid past each other, undergoing several off-axis collisions. Finally, the droplets underwent another head-on collision at a very slow speed again, but not coalescing immediately. It took about 4 *seconds* for these droplets to coalesce after the final contact.

There is a vast amount of work dedicated to the coalescence of two colliding droplets in a gas media (Neitzel & Dell'Aversana (2002)). For example, Qian & Law (1997) have studied the coalescence and bouncing of two colliding droplets approaching at different speeds and for different separation distances between the centers of mass of droplets. The graphical presentation of their outcome has been employed in an attempt to explain the temporary noncoalescence observed in this demonstration. Their results presented in Figure 98 show the different colliding regimes, as a function of Weber

number ($We = 2\rho_l R_d U_d^2/\sigma$) and the separation parameter B defined as the ratio of the distances between the centers of masses and the sum of the radii of the two droplets. For the head-on collisions of the two levitated droplets, the calculated Weber number is $We = 6.7\times10^{-4}$ (for 5 *cSt* silicone oil, R_d = 0.8 *mm*, U_d = 3 *mm/s*) and $B \sim 0$, which falls within the immediate coalescence regime (I) of Figure 98.

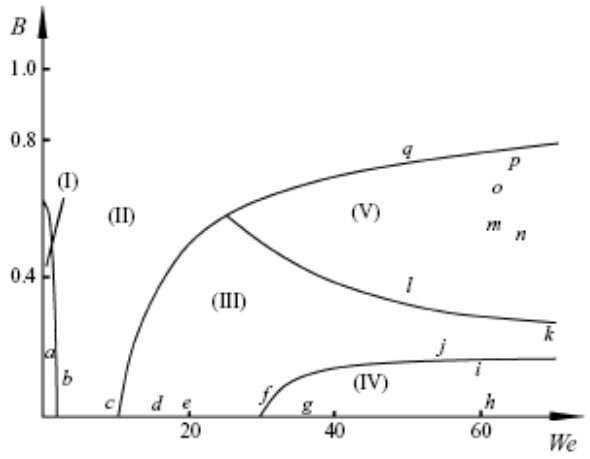


Figure 98. Various collision regimes of hydrocarbon droplets in 1 atm. air. Regimes (I) and (III) are coalescence, (II) is bouncing, (IV) is near head-on separation and (V) is off-center separation. The results from Qian & Law, (1997).

The discrepancy between the predicted coalescence from Qian & Law (1997) and the bouncing observed between the two levitated droplets must arise due to several factors. First, it is plausible that there is a very small off-set in the centers of the masses, and that the velocity vectors effectively set the system away from a perfect head-on collision course, resulting in regime (II). Another factor must be attributed to the presence of the free-surface motion. The free surfaces in the isothermal systems of Qian & Law remove the film out of the contact region. On the other hand, the surfaces of the levitated droplets move at a different speed and always replenish the contact region with air. In addition the free-surface speeds of two levitated droplets differ due to the differences in the volume of the droplets and the energy fluxes that the droplets receive at their respective positions.

The coalescence is desired to take place immediately in LOC applications. To do so, several conditions must exist to drain the film effectively from the contact region

between the droplets. Further investigations will be required to lay out an efficient procedure.

5.6. Evaporation Rate and Lifetimes of Droplets

The present research has demonstrated the levitation of a millimeter-scale droplet. Although the volumes of such droplets may be comparable to or even smaller than the ones used in conventional laboratory testing, it is desired that the droplet sizes be $O(100\ \mu m)$ and less to achieve more economical usage of expensive specimens for LOC applications. For such a small droplet to be levitated through heating, one must consider the effect of evaporation, since a droplet may evaporate completely before being delivered to a desired destination. Therefore, there is a design constraint based on the size and the evaporation rate of a levitated drop.

The evaporation rate has been determined experimentally by computing the volume of a levitated droplet from the images taken over a period of one hour at a frame rate of 2.5 minutes. The MATLAB code, developed for computing volumes in the nonwetting experiment, was slightly modified for this experiment. A 5 *cSt* silicone oil, which is more volatile than 10 cSt oil, has been levitated. In addition, we have employed Stephan's evaporation model Turns (2000) to describe the evaporation process, since there is no sound physical model that describes a complex evaporation mechanism from the surface of a levitated droplet.

Several restrictions must be imposed to use this model, simplifying the original complex system to a very simple one. These assumptions include (Turns (2000)):

1) A spherically symmetric droplet.
2) A quasi-steady evaporation process.
3) A uniform droplet temperature, which is less than the boiling point.
4) The mass fraction of vapor at the droplet surface is determined from the liquid-vapor equilibrium at the droplet temperature.
5) Thermophysical properties (including the diffusivity) are assumed to be constant.

All of these assumptions are not satisfied for the present problem in a strict sense. For example, the condition 1 is not accurate since a levitated droplet is not perfectly spherical. On the other hand, it is argued here that the deviation from the sphere is very slight since the capillary length scale, defined as

$$l_{\text{cap}} = \left(\frac{\sigma}{\rho g} \right)^{1/2}, \tag{75}$$

is $l_{\text{cap}} \sim 1.5\ mm$, whereas the radius of the levitated droplet is roughly 0.8 *mm*. This slight departure from spherical shape can also be confirmed from the images of levitated droplets, such as shown in Figure 82 and Figure 96. Condition 2 is also a good approximation since the system can be considered to be in steady state. Conditions 3–5 are not well suited for the present analysis, because of the presence of energy and mass transport between the droplet and the surroundings. Thus, the temperature and concentration of the vapor phase (of liquid) is not uniform around the droplet and the properties of liquid should vary accordingly in a strict sense.

Although restricted in its use, these simplifications lead to the following expression for the evaporation rate

$$\frac{d\left(D^2\right)}{dt} = -K_{\text{evap}}, \tag{76}$$

which states that the square of droplet diameter D^2 is a linear function of time with a characteristic evaporation constant K_{evap}.

The experimental result is presented in Figure 99 showing the changes in the values of D^2 of the levitated droplet as a function of time. In some instances, the size of the droplet is observed to increase; this is an error associated with out-of-plane displacement of the droplet, driven by air currents, which could not be eliminated completely. A straight line is used to fit the data, yielding

$$D^2\left(t\right) = 2.482 - 0.004797t \tag{77}$$

with an R-squared value of 0.96.

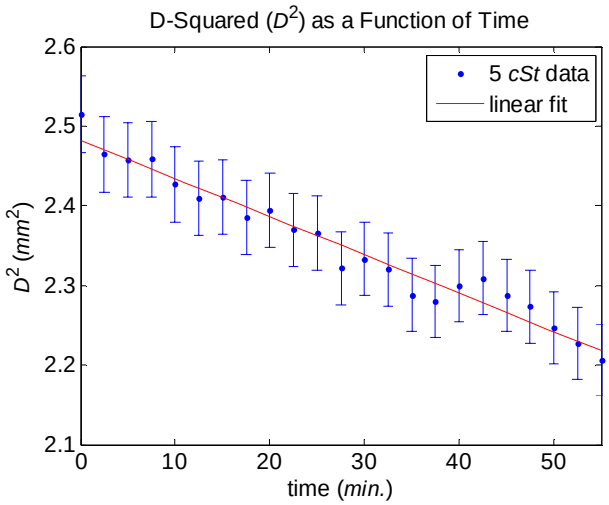


Figure 99. Changes in square of diameter of a levitated droplet over a period of ~ 1 *hour*. A consistent evaporation process reduces the diameter from 1.6 to 1.5 *mm*. 5 *cSt* silicone oil, which is more volatile than 10 *cSt* oil, is used for this experiment.

By assuming that the characteristic evaporation constant of the droplet is K_{evap} = .004797 $mm^2/min.$, a droplet with $O(100\ \mu m)$ diameter has a lifetime of roughly 100 *seconds*, which should be an order of magnitude larger than what is necessary for LOC applications. Consequently, evaporation should not pose a problem for such a droplet.

5.7. Contact Area Analysis

As discussed earlier, very tiny droplets with sizes of $O(100\ \mu m)$ or less are more desirable for LOC applications. These sizes, however, may pose a problem due to the increased capillary pressure within, and more spherical shape assumed by, the droplet. As a result, the size of the contact area, and thus the area over which the lubricating pressure acts, decreases, reducing the effect of the lubricating film to support the weight of the droplet. In order to levitate a droplet, a balance must exist between its weight and the lubrication force, as seen in the sketch of Figure 100.

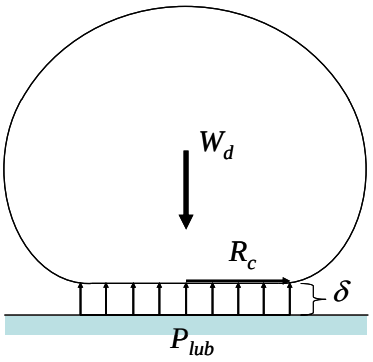


Figure 100. Schematics showing the force balance of a levitated droplet. The weight of the droplet is balanced by the lubricating pressure acting over the contact area.

This balance is expressed as

$$W_d = F_{\text{lub}} \tag{78}$$

where W_d is the weight of the droplet and F_{lub} is the force exerted by the lubricating film. Since F_{lub} is the resultant force due to the pressure field acting over the contact area, equation (78) can be rewritten in terms of P_{lub}, the average pressure in the lubricating film and $A_c = \pi R_c^2$, the contact area, as

$$W_d = P_{\text{lub}} A_c . \tag{79}$$

According to the equation above, an increase in the lubricating pressure reduces the contact area needed to balance the weight of the droplet. The sections to follow will discuss two different approaches used to arrive at the expressions for the changes in the contact area as a function of droplet size.

5.7.1. Analysis Based on Lubricating Film Pressure

The changes in the size of the contact area are derived based on the assumptions that the lubricating pressure scales by $P_{\text{lub}} \sim \mu_g U_s R_c / \delta^2$, as discussed in Dell'Aversana & Neitzel (2004) and employed in Section 3.5.1 to estimate the shear rate of the lubricating film. With the weight of the droplet $W_d \sim \rho_l g R_d^3$ and contact area $A_c \sim R_c^2$ the force balance in equation (79) becomes

$$\rho_l g R_d^3 \sim \frac{\mu_g U_s R_c^3}{\delta^2}. \tag{80}$$

The formulation above requires another scaling for the film thickness δ. It has been shown in Section 3.5.1 that the temperature gradient, and hence the surface-tension gradient, is relatively small in the contact region bounded by the radius R_c. Therefore, the shear stress balance exists between liquid and gas phases in this region

$$\frac{\mu_l U_s}{R_d} \sim \frac{\mu_g U_s}{\delta}, \tag{81}$$

where R_d is radius of the droplet, μ_l and μ_g are viscosities of the liquid and gas phases, respectively, and U_s is the free-surface velocity. Upon a rearrangement, the scale for the average film thickness is obtained as

$$\delta \sim \frac{\mu_g}{\mu_l} R_d . \tag{82}$$

This is a good estimate for the present analysis; the viscosity ratio is $O(0.001)$, yielding the film thickness of $O(1\ \mu m)$ for a droplet with the radius $O(1\ mm)$. By substituting this expression into equation (80), the following expression is obtained for the radius of contact area

$$\frac{R_c^3}{R_d^3} \sim \mu Bo Ca^{-1}, \tag{83}$$

where $\mu = \mu_g / \mu_l$ is the viscosity ratio between gas and liquid phases, $Bo = \rho_l g R_d^2 / \sigma_0$ is the Bond number and $Ca = \gamma \Delta T / \sigma_0$ is the capillary number. This expression states that the contact radius increases with the viscosity ratio, complemented by an increase in the film thickness (equation(82)) and corresponding decrease in the film pressure. Also, the expression states that the contact area increases with Bo. This follows from the fact that a larger deformation is expected for a bigger droplet due to the increased gravitational effect in comparison to the capillary effect, resulting in a larger contact area. Finally, the contact radius decreases with an increase in Ca due to an increase in the thermocapillary surface speed ($\propto \gamma \Delta T$), which results in an increase in the lubricating film pressure.

5.7.2. Analysis Based on Capillary Pressure

This section will present an alternative method for estimating the size of contact radius based on the assumption that the lubricating film pressure is of the same order of magnitude as the capillary pressure (*i.e.*, $P_{\text{lub}} \sim P_{\text{cap}}$). The pressure jump across the curved interface of a droplet is given by

$$\Delta P = \sigma\left(\frac{1}{R_a} + \frac{1}{R_b}\right), \tag{32}$$

where R_a and R_b are the principal radii of curvature of the interface within the lubricated region of the drop. By assuming that the deformation on a levitated droplet is sufficiently small, given that its size is very tiny, the radii of curvatures can be assumed to be of the same order of magnitude as the droplet radius R_d,

$$R_a \sim R_b \sim R_d . \tag{84}$$

Under these assumptions, the scale for the capillary pressure can be expressed as

$$P_{cap} \sim \frac{\sigma}{R_d} \tag{85}$$

where σ is surface tension and R_d is the radius of the droplet. Substituting equation (85) into equation (79) (and $P_{\text{lub}} \sim P_{\text{cap}}$) the expression for the contact radius becomes

$$\frac{R_c^2}{R_d^2} \sim Bo , \tag{86}$$

which only depends on the Bond number. Again, the expression states that the contact radius should increase with the Bond number, due to the increased effect from the body force as compared with that from capillarity.

5.7.3. Surface Evolver Simulations

Surface Evolver can be used to simulate the shapes of levitated droplets and they can be used to compare the sizes of the contact radius as a function of Bond number, as discussed in the previous sections. Various volumes of droplets (with density and surface tension of 5 *cSt* silicone oil), subjected to gravity, are assumed to be deposited on a perfectly nonwetting plane and solved for the minimum-energy configurations. The results for several droplet-sizes are presented in Figure 101. The first droplet in (a) is about the size of a levitated droplet typically observed in experiments. As the volume of the droplet is reduced by half, as shown in (b), surface-tension forces starts to overcome gravity, the effect of which is seen as a more spherical shape and reduced contact area. The image in (c) shows the droplet with ~ 1 *mm* diameter. The last image in (d) shows the droplet with the radius roughly 100 μm with almost perfect spherical symmetry. Here, the capillarity completely overwhelms the body force ($Bo \sim 4.55\times10^{-3}$).

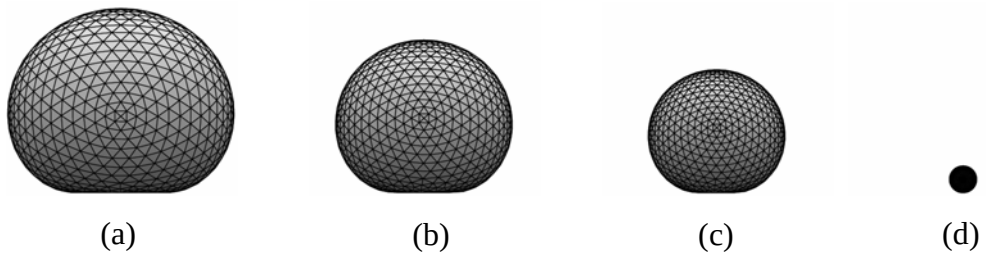


Figure 101. Static droplet profiles computed from Surface Evolver. The volumes (and the radii) are (a) 2.5 (0.81); (b) 1.25 (0.67); (c) 0.6 (0.52) and; (d) 0.005 (0.106) mm^3 (*mm*). These images are to-scale to one another.

The contact areas can be computed from these results by computing the areas of meshed elements crossing a hypothetical plane that is parallel to the nonwetting surface and is displaced 1 *nm* into the droplet. It is important to note that the Surface Evolver computations are for static droplets and, as such, the only pertinent parameter is the Bond number or the radius of the droplet; considerations of shear stress used to arrive at equation (83) are irrelevant in the current analysis. In this sense, only the dependency on Bond number is explored in equation (83).

From knowledge of the droplet volume defined in Surface Evolver simulations, the droplet radius is defined as

$$R_d = \left(\frac{3}{4\pi} \mathscr{V} \right)^{1/3}, \tag{87}$$

which is a good assumption for droplets with small Bond number. The droplets in the present analysis lies within the range of $0.023 < Bo < 0.45$.

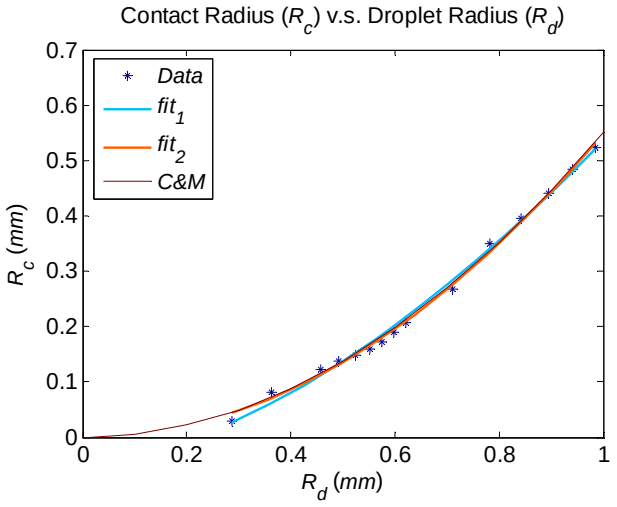


Figure 102. Sizes of contact radii as a function of the droplet radii. The data from Surface Evolver are shown as the dotted legend. The two scaling arguments are used for the fits through the data points. In addition, the result from Charles & Mason (1960) (*C&M* in the legend) is compared with the data from Surface Evolver.

The dotted points in Figure 102 show the variation of contact radius with the droplet radius, as computed from Surface Evolver. As the equivalent radius of the droplet decreases, so does the contact radius due to the increased capillary effect. Two functions are used to fit the data points (blue and red curves), both of which are based on the scaling arguments discussed in the previous sections. The first fit (fit_1, the blue curve) follows the form of equation (83), which is based on the force balance between the lubricating film and the weight of the droplet, yielding a relationship for the contact radius of the form

$$R_c \propto R_d^{5/3}. \tag{88}$$

MATLAB is used to fit the data, resulting in the following expression,

$$R_c = 0.5812 R_d^{5/3} - 0.04571 \qquad (89)$$

with the R-squared value of 0.996. The second fit (fit_2, the red curve) follows from equation (86), which is based on the capillary pressure, yielding

$$R_c \propto R_d^2 . \qquad (90)$$

Again, the best fit through the data points gives the equation of the form

$$R_c = 0.5506 R_d^{\,2} - 0.002229 \qquad (91)$$

with the R-squared value of 0.997.

In addition, these curves are compared with a theoretical curve derived by Charles & Mason (1960), which is indicated in the legend as "*C&M*". The curve is expressed in the following form

$$R_c = R_d^2 \left(\frac{2\Delta\rho g}{3\sigma} \right)^{1/2}, \qquad (92)$$

where R_d is the droplet radius, $\Delta\rho$ is the density difference between the droplet and surrounding phases, g is the gravity, and σ is the surface tension. For this analysis, the density difference is approximated by the liquid density ($\Delta\rho \sim \rho_l$). It is worthwhile to note that the formulation from Charles & Mason is a power law, with the contact radius growing like the square of the droplet radius, which agrees with the analysis based on the capillary pressure (equation (90)). In fact, the results from Charles & Mason match well with the Surface Evolver output. For an instance, coefficients appearing in the second fit (equation (91)) and *C&M* (equation (92)) are 0.5506 mm^{-1} and 0.5505 mm^{-1}, respectively, indicating that two curves effectively lie on top of each other. It is plausible that these two analyses agree so well because they are based on static models. Small differences between these results may be attributed to several factors. First, the contact area computed in Surface Evolver is evaluated at a virtual plane, 1 *nm* above the nonwetting surface: The contact area will never approach to zero even as the droplet size is reduced since the hypothetical plane always crosses the droplet surface. Second, the contact area computed in Surface Evolver is sensitive to the minimization procedure. The meshed

elements at the bottom of the droplet, which are in contact with the nonwetting plane, coarsen as Surface Evolver minimizes the energy, introducing errors. Vertex averaging, which smoothes out the coarsened mesh, results in another form of error by increasing the overall energy of the droplet and moving the system away from the minimum energy state. Thus, a compromise must be made between these errors during Surface Evolver computations.

It is suspected that the contact radius of a levitated droplet is well-modeled by the analyses carried out in this section. Further experiments are required to determine the size of the contact radius as a function of droplets size for thermocapillary levitation.

5.7.4. Discussion on Droplet Squeezing

The relationship between contact area and droplet sizes has been determined in the previous sections. With capillary forces overwhelming the body force, the shapes of tiny droplets are nearly spherical. Consequently, their contact areas shrink and the lubricating film can no longer exert sufficient force to balance the weight of the droplet. Therefore, it may be difficult, or even impossible to levitate *freely* a droplet with a radius of roughly 100 μm. As a result, a droplet with the radius size of $O(100\ \mu m)$ may require a squeezing in order to increase the contact area upon which the lubricating film acts.

Following a discussion from Charles & Mason (1960), the magnitude of force F required to deform a droplet with an initial diameter $2R_d$ to a final height of $2H$ (Figure 103) is given by

$$F = \frac{32\sigma}{\pi R_d}\left(R_d - H\right)^2 . \qquad (93)$$

For a 5 *cSt* silicone droplet with R_d = 100 μm, the force required to squeezed the droplet to half the original size (H = 50 μm) is roughly 0.5 *dynes*. This force can also be considered as the “restoring force”, with which the free-surface of the droplet would push into the lubricating film in an attempt to maintain a spherical shape or the minimum energy-state.

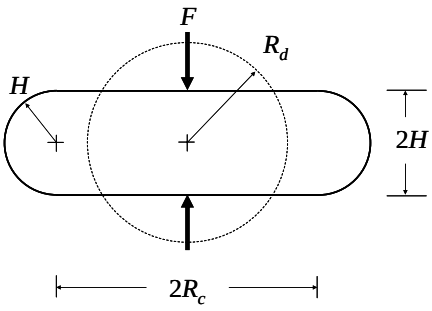


Figure 103. Flattened droplet with original radius R_d, squeezed by applying a force, F. The flattened droplet has a height $2H$, with the contact radius R_c.

To realize a system where a warm droplet is squeezed between two cooled plates, the restoring force of equation (93) must be balanced by the pressure exerted by the lubricating film acting over an enlarged contact area. A scaling argument discussed below will be used to estimate the average force exerted by the lubricating-film pressure acting over the contact region. A squeezed droplet may be realized if the lubrication force, obtained from the scaling argument, equals the restoring force, *i.e.*,

$$\frac{\text{force from lubrication}}{\text{force required to deform}} = \frac{F_{\text{lub}}}{F} = 1. \qquad (94)$$

As argued earlier, the force from the lubricating film is the product of lubricating film pressure multiplied over the contact area

$$F_{\text{lub}} \sim \frac{\mu_g U_s}{\delta^2} R_c A_c . \qquad (95)$$

Additionally, the average film thickness δ is derived from the shear-stress balance at the contact region (and assuming tangential stress due to surface tension gradient is negligible). The shear-stress balance in the contact region is then,

$$\mu_g \frac{U_s}{\delta} \sim \mu_l \frac{U_s}{2H}, \qquad (96)$$

where $2H$ is the height of the deformed droplet, as seen in the sketch of Figure 103. As a result, the average film thickness yields

$$\delta \sim \frac{\mu_g}{\mu_l}(2H) \qquad (97)$$

Furthermore, the size of the contact area is evaluated from the first-order estimate from Charles & Mason (1960), which describes the size of contact radius as function of the deformed droplet height H as

$$R_c = \frac{4}{\pi}\left(R_d - H\right). \tag{98}$$

The contact area is simply $A_c = \pi R_c^2$. Using the thermal-Marangoni velocity scale as before ($U_s \sim \gamma\Delta T/\mu_l$, where ΔT defines an arbitrary temperature difference between a hot region on the droplet and the cold plate) the expression for the force scale due to the lubricating film is

$$F_{\text{lub}} \sim \frac{16}{\pi^2}\frac{\gamma\Delta T}{\mu}\frac{\left(R_d - H\right)^3}{H^2}. \tag{99}$$

Here, μ is the viscosity ratio between gas and liquid phases ($= \mu_g/\mu_l$). The following expression is, then, the ratio of the forces

$$\frac{F_{\text{lub}}}{F} = \frac{1}{2\pi}\frac{Ca}{\mu}\frac{R_d}{H}\left(\frac{R_d}{H} - 1\right), \tag{100}$$

where Ca is the capillary number ($= \gamma\Delta T/\sigma$).

The ratio of the forces presented in equation (100) is plotted against the shape parameter H/R_d, the ratio of the final droplet height and the original droplet radius, in Figure 104. In this analysis, a droplet with the properties of 5 *cSt* silicone oil is squeezed from an initial radius of R_d = 100 μm. The imposed temperature difference is assumed to be at 10 °C , which drives the air as the lubricating medium. All of the fluid properties are evaluated at the room temperature.

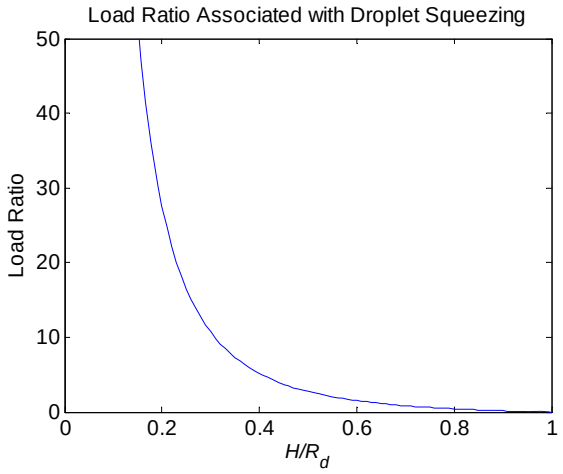


Figure 104. Ratio of the forces from lubricating film and that required to induce deformation. The properties of 5 *cSt* silicone oil and air at 25 °C are used, with the initial droplet radius of 100 μm and ΔT = 10 °C.

As indicated by the graph, the ratio is zero when no squeezing is applied on a perfectly spherical droplet ($H/R_d \rightarrow 1$), indicating that the lubricating mechanism is not at work. However, the ratio grows larger with deformation, where the value equals to 1 roughly at $H/R_d = 0.67$. The ratio becomes even larger with further deformation. This may suggest that the "load-carrying potential" of the lubricating film increases with the squeezing due to higher temperature gradient generated between hot and cold spot on the free surface. The ratio becomes about 5 around $H/R_d = 0.40$. A further squeezing increases the ratio asymptotically to infinity as $H/R_d \rightarrow 0$. The argument from the load ratio may suggest that a higher squeezing is preferred on a sandwiched droplet, though stability of the lubricating-film flow must be taken into considerations. To achieve a high compression, a higher temperature difference may be imposed on the droplet, increasing the stability of the lubricating film.

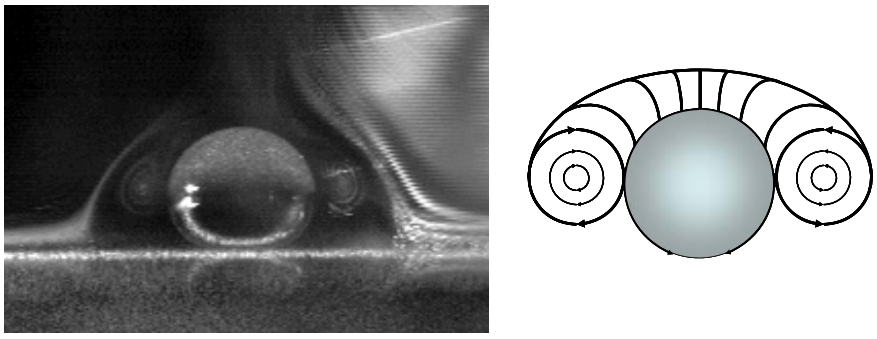
It is also important to note that different techniques are required for the formation and heating of the squeezed droplet. As the scaling suggests, it may be difficult to initiate the squeezing on a spherical drop. Therefore, the droplet should be formed between the two plates with thermocapillary convection already present within, instead of initiating the squeezing on a spherical droplet. In addition, the laser beam must heat just the

periphery of the droplet instead of its top (as was done throughout the present research) since the lubricating film would be depleted from the top of the droplet.

5.8. The Flow Field around a Levitated Droplet

5.8.1. Observations

Smoke particles from incense have been used to help visualize the flow field around a levitated droplet. A sheet of He-Ne laser is used to illuminate a plane parallel to the image plane at the center of the droplet. Figure 105(a) shows a single frame taken from a video recording of a stationary levitated droplet. Visible within the image is a circular path that is traced out by the incense particles, as sketched in Figure 105(b) for illustrative purposes. Due to the symmetry in the flow (and thus the pressure) field around the droplet, the droplet stays stationary when placed at the center of Gaussian beam. The droplet is relatively stable in this position even though a weak air current disturbs it.



(a) (b)

Figure 105. (a) Flow visualization of around a statically levitated droplet. The incense particles trace out a circular path, driven by the free-surface motion of the droplet. Due to symmetry in the flow (and pressure) field, the droplet can be positioned stably at this location even when there is air current to push the droplet off from the heat source; (b) schematics of a generalization of axisymmetrical flow pattern around the droplet.

In addition, the same flow-visualization has been applied to a translating droplet (at speeds less than 1 *mm/s*). A visual inspection of the video sequences could not detect any difference in the flow fields between the stationary and the translating droplet. Although difficult to observe with the naked eye, a variation of surface velocity on the droplet should result in an asymmetry in the flow field around the droplet. The flow

asymmetry drives the surrounding gas from the trailing (cold) end of the droplet, resulting in the net propulsion towards the leading (warmer) end of the droplet and the center of the Gaussian beam profile. .

5.8.2. Propulsion Estimate Based on Pressure Distribution

Due to the presence of the circulating flow around the droplet, the estimation of propulsive forces based on the momentum flux (in a 2-D sense) is not straightforward. This section will attempt to derive an estimate by integrating the pressure field around the droplet thereby eliminating the momentum flux from the picture. The derivation presented in this section, however, is based on several assumptions that may depart from the real physical system and thus should be used as a first order estimate.

First, the pressure on the free surface must be evaluated. This is done by assuming inviscid, loss-free flow in the regions away from the droplet surface with the air moving at the same speed as the free surface on the droplet. Under these restrictive assumptions, Bernoulli's equation can be integrated between a stagnation point (sufficiently away from drop) and the free surface, yielding the gage pressure on the free surface to be

$$P_s = -\frac{1}{2}\rho_g U_s^2, \tag{101}$$

where ρ_g is the density of the gas and U_s is the speed of the free-surface. The infinitesimal force acting in the *x*–direction due to the pressure distribution is given by

$$dF = -P d\underset{\sim}{S} \cdot \hat{e}_x, \tag{102}$$

where $d\underset{\sim}{S}$ is the outwardly pointing area-element vector and $\hat{e}_x$ is the unit vector in the *x*-direction. By assuming that the droplet is spherical, *i.e.*, the unit normal vector from the surface points radially outward in a spherical-coordinate system (Figure 106), the area element can be expressed as

$$d\underset{\sim}{S} = R_d^2 \sin\phi \, d\theta \, d\phi \; \hat{e}_r, \tag{103}$$

where R_d is the droplet radius, with the unit vectors in *x*- and *r*-directions related by

$$\hat{e}_x = \hat{e}_r \sin\phi \cos\theta. \tag{104}$$

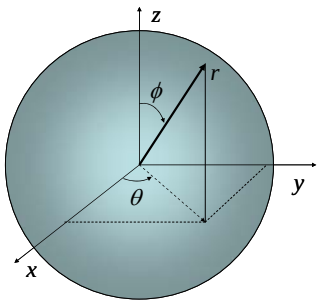


Figure 106. Spherical coordinate-system used for the estimate of the propulsive force. The shape of the droplet is assumed to be spherical.

The integral of equation (102) over the surface of the spherical droplet leads to the expression for the net force, acting in the *x*-direction,

$$F = \frac{1}{2}\rho_g R_d^2 \int_{\phi=0}^{\pi}\int_{\theta=0}^{2\pi} U_s^2 \sin^2\phi\cos\theta d\theta d\phi . \qquad (105)$$

Equation (105) yields $F = 0$ if the speed of the free-surface is independent of the azimuthal direction θ, which is the case if the droplet is placed directly beneath the center of the Gaussian beam.

To simplify the integration of equation (105), the velocity distribution on the free-surface of a droplet is further assumed to have only a meridional component (*i.e.*, no swirl is present), which depends only on the azimuthal direction, *i.e.*, $U_s = U_\phi(\theta)$. These assumptions are not strictly accurate because the speed must approach zero at top and bottom of the droplet due to the circulatory flow-field within the droplet. By making these assumptions, however, the integral can be simplified to yield

$$F = \frac{\pi}{4}\rho_g R_d^2 \int_0^{2\pi} U_\phi^2(\theta)\cos\theta d\theta . \qquad (106)$$

By arguing that the flow field is symmetric about the *x*-*z* plane (see Figure 106), satisfying $U_\phi(\theta) = U_\phi(2\pi - \theta)$, the term appearing inside of the integral also becomes symmetric, and equation (106) can be rewritten as

$$F = \frac{\pi}{2}\rho_g R_d^2 \int_0^{\pi} U_\phi^2(\theta)\cos\theta d\theta . \qquad (107)$$

It can be shown that the integral in equation (107) is positive-definite, *i.e.*, $F > 0$ under the hypotheses that the free-surface velocity is monotonically decreasing in the azimuthal direction, *i.e.*, $dU_\phi / d\theta < 0$ and the free-surface speed is always positive, *i.e.*, $U_\phi > 0$, in the range $0 < \theta < \pi$. The first of these assumptions is based on the assumed Gaussian nature of the incident energy on a droplet and the resultant motion of the free surface–the induced thermocapillary-flow would follow the gradient of surface energy between the heated and cooled regions on the free surface. By this convention, it is argued that the regions of the surface receiving higher energy flux would be driven more vigorously towards the cooler regions below the droplet. Since the energy flux from the laser decreases monotonically from the center of the Gaussian beam, it is argued here that the free-surface speed decreases accordingly (monotonically) from the leading edge to the trailing edge (if the droplet is placed to the left of the Gaussian profile). The second of the assumptions is that the flow is always directed from the top of the droplet towards the bottom, and that there is no returning flow on the free-surface, which is required for a levitated droplet to provide the necessary lubrication.

To prove the argument $F > 0$ under these circumstances, the integral in equation (107) is first expanded

$$\begin{aligned} \int_0^{\pi} U_\phi^2(\theta)\cos\theta d\theta &= \int_0^{\pi/2} U_\phi^2(\theta)\cos\theta d\theta + \int_{\pi/2}^{\pi} U_\phi^2(\theta)\cos\theta d\theta \\ &= \int_0^{\pi/2} U_\phi^2(\theta)\cos\theta d\theta - \int_{\pi/2}^{\pi} U_\phi^2(\theta)\cos(\pi-\theta) d\theta \end{aligned} \quad . \qquad (108)$$

By defining a new variable $\psi = \pi - \theta$ the second integral can be rewritten, yielding the expression

$$\begin{aligned} &= \int_0^{\pi/2} U_\phi^2(\theta)\cos\theta d\theta + \int_{\pi/2}^{0} U_\phi^2(\pi-\psi)\cos(\psi) d\psi \\ &= \int_0^{\pi/2} U_\phi^2(\theta)\cos\theta d\theta - \int_0^{\pi/2} U_\phi^2(\pi-\psi)\cos(\psi) d\psi \,, \qquad (109) \\ &= \int_0^{\pi/2} \left[U_\phi^2(\theta') - U_\phi^2(\pi-\theta')\right]\cos\theta' d\theta' \end{aligned}$$

where θ' is a dummy variable. The term in the bracket is always positive, *i.e.* $U_\phi^2(\theta') - U_\phi^2(\pi - \theta') > 0$, since the speed is assumed to decrease monotonically and always positive. In addition, $\cos\theta' > 0$ always in the interval $0 < \theta < \pi/2$. Therefore, the integral is always positive. Though restricted by several assumptions, the above result shows the generation of net propulsion towards the heat source without evaluating the momentum flux.

To estimate the magnitude of the force, the integral in (107) is evaluated using a monotonically decreasing velocity profile,

$$U_\phi(\theta) = \frac{(U_H + U_C)}{2} + \frac{(U_H - U_C)}{2}\cos\theta. \qquad (110)$$

The profile states that the free-surface on the hot (leading) side, $U_\phi(\theta = 0) = U_H$, is moving faster than that on the cooler (rear) side $U_\phi(\theta = \pi) = U_C$, and possesses a smooth variation in the azimuthal direction with a period 2π. Such a profile follows from the assumptions, which are based on the monotonically decreasing energy gradient on the free surface generated by the monotonically decreasing Gaussian beam intensity. The graphical presentation of the assumed profile is presented in Figure 107.

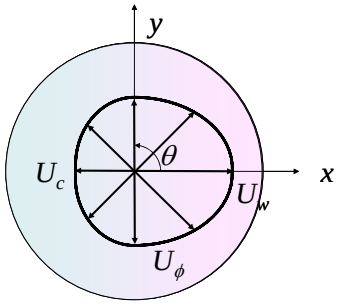


Figure 107. Variation of the surface-velocity profile around the azimuthal direction on the free surface of the droplet. The speed decreases monotonically around the azimuthal direction due to the monotonicity of the Gaussian nature of the incident energy profile.

The resultant force for this specific case is given by

$$F = \frac{1}{8}\rho_g R_d^2 \pi^2 \left(U_H^2 - U_C^2\right), \qquad (111)$$

which indicates that the estimate is proportional to the difference in the square of the free-surface speeds between the warmer and cooler ends of the droplet. The present estimate given by equation (111) is of the same order of magnitude as the one derived based on the momentum flux ($F \sim \rho_g R_d^2 U_s^2$), assuming that the difference in the free-surface speed is sufficiently large between front and back of the drop. For example, it was argued in Chapter 1 that net-jetting speed of $O(10\ cm/s)$ is required to accelerate a *mm*-scale droplet at $O(10\ mm/s^2)$. Based on the new estimate, the warmer side must be moving $O(10\ cm/s)$ faster than the cooler side to achieve the same acceleration. For the accelerations measured from the controlled-delivery experiments, $a = O(0.01–0.1\ mm/s^2)$, the differences in the speed are estimated to be $O(0.1–1\ mm/s)$.

5.9. Final Remarks on Droplet Levitation

Droplet levitation, successfully demonstrated in the present study, exploits the mechanism of permanent nonwetting. In addition, it has been demonstrated that positions of a levitated droplet can be controlled by moving the laser beam on the test surface. Also, levitation of a compound droplet has been demonstrated, indicating a potential delivery method for an aqueous droplet with minimal contamination from the surrounding. Furthermore, it was demonstrated that two levitated droplets can be merged together, and be used as a mixing chamber. All of these demonstrations show potential for levitated droplets to be used in LOC applications

The speed of a levitated droplet, under a controlled fashion, remained $O(0.1\ mm/s)$ in the present system setup. Although such speed is lower than that observed for droplets undergoing oscillatory behavior (with speeds of $O(1\ mm/s)$ and higher), it should be possible to control a levitated droplet at higher speeds with further improvement of the experimental setup and the better understanding of involved physics. In addition, a simple physical model is discussed, providing insights into the oscillatory behavior of a levitated droplet. Though the model is simple, it captures the effects of different physical parameters on the dynamics, agreeing qualitatively with observations.

The diameter of the levitated droplet was about 1.6 *mm*. However, the use of droplets with sizes $O(100\ \mu m)$ and smaller is desired in LOC applications for they are more economical and allow for quicker sample processing. In these situations, the

evaporation rate must be understood to ensure that the droplet survives until it reaches its final location. The evaporation rate of 5 *cSt* silicone oil has been measured, providing an estimate that a droplet of with 100 μm diameter has a lifetime of 100 *s*, which should be sufficient for LOC applications.

In addition to the evaporation rate, the size of the contact area is another important factor that must be taken into consideration, for it determines whether a small droplet would stay afloat with help from the lubricating film flow. Surface Evolver has been used to simulate the shapes of levitated droplets and to compute the contact radius of a droplet. The results obtained through scaling arguments show that that size of the contact radius varies with the droplet radius raised to a powers of 5/3 and 2. The square-law, which is derived from the capillary pressure balance, agrees with the derivations of Charles & Mason (1960). These results quantitatively suggest that small droplets require "squeezing" in order to generate an effective lubricating force for levitation. In order to squeeze the drop, the force exerted by the lubricating film must overwhelm that required to deform the droplet. The ratio of these forces increases with the compression, indicating that a moderate compression is preferred by a squeezed droplet.

Finally, flow visualization helped to visualize a vortex structure around the droplet. It is argued that the net propulsion is generated by breaking the symmetry of the vortex and the pressure distribution around the droplet.

These studies on levitation are rudimentary, and the conclusions are based on the limited resources available that were available for the present analysis. Further investigations will be required to realize a robust system that employs levitated droplets as a liquid handling scheme. The author hopes that these analyses will be of a useful resource for future investigators on the subject of droplet levitation based on thermocapillary permanent nonwetting.

6. Conclusion and Recommendations

The results presented in this thesis are aimed at promoting the integration of permanent nonwetting droplets into potential engineering applications. The first part of the work discusses failure mechanisms of thermocapillary-nonwetting systems, triggered by the application of high compressive loading. Film failure occurs primarily when the system's temperature difference is relatively low, corresponding to slower speeds for the free-surface and induced lubricating film. The film becomes more stable as the vigor of thermocapillary convection increases with increased applied temperature gradient across the droplet, allowing the system to sustain a higher load. As a consequence of the stabilized film, droplets can be pushed further to the point where pinning failures will result. These quantitative and qualitative descriptions of failures will be useful for designing a load-bearing system using nonwetting droplets.

The second part of the thesis focuses on the development of a system that allows a moving free-surface to be reconstructed from a series of interferograms within the contact regions. This reconstructed surface can reveal details of the relevant to the physics of both phases within the "contact" region, the heart of a permanent nonwetting system. The technique uses a minimization algorithm, comparing the local intensity of the image and a model to evaluate the unknown phase difference between the reference and the reflected beams. A smooth phase-structure, retrieved by the procedure described in this report, allows various analyses to be carried out, such as the use of FFT demonstrated in the present thesis. The system described here is a promising tool to analyze the dynamic response for different operating conditions such as input amplitude and frequency of excitation, volume of the droplet, and the squeezing imposed on the droplet.

Finally, the work in this thesis has succeeded in demonstrating droplet levitation and its controlled translation, the mechanics of which are based on the mechanisms responsible for thermocapillary-driven permanent nonwetting. The weight of a droplet is supported by the force exerted by the lubricating film driven underneath the droplet by thermocapillary convection set into motion via infrared heating. Droplets can be translated by moving the locations of the incident energy, resulting in asymmetry in the flow field around the droplet, such that more air is driven from the cooler end of the

droplet, generating net propulsion towards the region with higher energy intensity. These results, backed by simple physical-descriptions and modeling, will be a useful foundation upon which these behaviors of the droplet could be exploited as a liquid-delivery scheme in a LOC system in the near future.

Additional work must be carried out to permit the levitation/translation of aqueous droplets in lab-on-a-chip architectures. As pointed out in the thesis, water is a difficult medium to manipulate via thermocapillarity. However, the encapsulation of water droplets in silicone oil provides benefits from the standpoint of levitation/translation, evaporation control, and sample-to-sample contamination. Future work in this area should focus on the development of techniques for producing individual, nanoliter-size compound droplets of variable water/oil volume-ratio and the design of injection and heating schemes to permit such droplets to be successfully squeezed between parallel planes and translated without wetting. Finally, the merging and mixing of the contents of such compound drops has not been addressed in this work and requires study to fully realize the potential of the proposed LOC scheme.

Bibliography

Amarouchene, Y., Cristobal, G. & Kellay, H. 2001 Noncoalescing Drops. *Physical Review Letters* **87**, 206104-206101 -206104-206104.

Balasubramaniam, R., Lacy, C. E., Woniak, G. & Subramanian, R. S. 1996 Thermocapillary Migration of Bubbles and Drops at Moderate Values of Marangoni Number in Reduced Gravity. *Physics of Fluids* **8**, 872-880.

Basaran, O. A. 2002 Small-Scale Free Surface Flows with Breakup: Drop Formation and Emerging Applications. *AIChE Journal* **48**, 1842-1848.

Batchelor, G. K. 1967 *An Introduction to Fluid Dynamics.* Cambridge University Press.

Benintendi, S. W. & Smith, M. K. 1999 The Spreading of a Non-Isothermal Liquid Droplet. *Physics of Fluids* **11**, 982-989.

Bousse, L., Cohen, C., Nikiforov, T., Chow, A., Kopf-Sill, A. R., Dubrow, R. & Parce, W. J. 2000 Electrokinetically Controlled Microfluidic Analysis Systems. *Annual Review of Biophysics and Biomolecular Structure* **29**, 155-181.

Bradley, G. & Weaire, D. 2001 Instabilities of Two Liquid Drops in Contact. *Computing in Science & Engineering* **3**, 16-21.

Brakke, K. A. *The Surface Evolver* Brakke, Kenneth A.

Charles, G. E. & Mason, S. G. 1960 The Coalescence of Liquid Drops with Flat Liquid/Liquid Interfaces. *Journal of Colloid Science* **15**, 236-267.

Chaudhury, M. K. & Whitesides, G. M. 1992 How to Make Water Run Uphill. *Science* **256**, 1539-1541.

Chen, A. U. & Basaran, O. A. 2002 A New Method for Significantly Reducing Drop Radius without Reducing Nozzle Radius in Drop-on-Demand Drop Production. *Physics of Fluids* **14**, L1-L4.

Cho, S. K., Moon, H. & Kim, C.-J. 2003 Creating, Transporting, Cutting, and Merging Liquid Droplets by Electrowetting-Based Actuation for Digital Microfluidic Circuits. *Journal of Microelectromechanical systems* **12**, 70-80.

Chung, S. K. & Trinh, E. H. 1998 Containerless Protein Crystal Growth in Rotating Levitated Drops. *Crystal Growth* **194**, 384-397.

Couder, Y., Fort, E., Gautier, C. H. & Boudaoud, A. 2005 From Bouncing to Floating: Noncoalescence of Drops on a Fluid Bath. *Physical Review Letters* **94**, 177801-177801-177804.

Darhuber, A. A., Davis, J. M., Troian, S. M. & Reisner, W. W. 2003 Thermocapillary Actuation of Liquid Flow on Chemically Patterned Surfaces. *Physics of Fluids* **15**, 1295-1304.

Darhuber, A. A., Valentino, J. P., Davis, J. M. & Troian, S. M. 2003 Microfluidic Actuation by Modulation of Surface Stresses. *Applied Physics Letters* **82**, 657-659.

de Gennes, P. G. 1985 Wetting: Statics and Dynamics. *Reviews of Modern Physics* **57**, 827-863.

Dell'Aversana, P., Banavar, J. R. & Koplik, J. 1996 Suppression of Coalescence by Shear and Temperature Gradients. *Physics of Fluids* **8**, 15-28.

Dell'Aversana, P., Monti, R. & Gaeta, F. S. 1995 Marangoni Flows and Coalescence Phenomena in Microgravity. *Advanced Space Reserve* **16**, 95-98.

Dell'Aversana, P. & Neitzel, G. P. 1998 When Liquids Stay Dry. *Physics Today* 38-42.

Dell'Aversana, P. & Neitzel, G. P. 2004 Behavior of Noncoalescing and Nonwetting Drops in Stable and Marginally Stable States. *Experiments in Fluids* **36**, 299-308.

Dell'Aversana, P., Tontodonato, V. & Carotenuto, L. 1997 Suppression of Coalescence and of Wetting: The Shape of the Interstitial Film. *Physics of Fluids* **9**, 2475-2485.

Drazin, P. G. & Reid, W. H. 2004 *Hydrodynamic Stability.* Cambridge University Press.

Ford, M. L. & Nadim, A. 1994 Thermocapillary Migration of an Attached Drop on a Solid Surface. *Physics of Fluids* **6**, 3183-3185.

Gallerdo, B. S., Gupta, V. K., Eagerton, F. D., Jong, L. I., Craig, V. S., Shah, R. R. & Abbott, N. L. 1999 Electrochemical Principles for Active Control of Liquids on Submillimeter Scales. *Science* **283**, 57-60.

Garner, F. H. & Haycock, P. J. 1959 Circulation in Liquid Drops. *Proceedings of Royal Society of London, Series A, Mathematical and Physical Sciences* **252**, 457-475.

Garnier, N., Grigoriev, R. O. & Schatz, M. F. 2003 Optical Manipulation of Microscale Fluid Flow. *Physical Review Letters* **91**, 054501-054501-054504.

Gau, H., Herminghaus, S., Lenz, P. & Lipowsky, R. 1999 Liquid Morphologies on Structured Surfaces: From Microchannels to Microchips. *Science* **283**, 47-48.

Golovin, A. A., Nepomnyashchy, A. A. & Pismen, L. M. 1995 Pattern Formation in Large-Scale Marangoni Convection with Deformable Interface. *Physica D* **81**, 117-147.

Hendricks, C. L. L., van Vliet, L. J., Rieger, B., van Kempen, G. M. P. & van Ginkel, M. *Dipimage: A Scientific Image Processing Toolbox for Matlab* Quantitative Imaging Group, Delft University of Technology

Hill, M. J. H. 1984 On a Spherical Vortex. *Philosophical Transactions of the Royal Society of London. A* **185**, 213-245.

Huntley, J. M. & Saldner, H. O. 1997 Temporal Phase Unwrapping: Application to Surface Profiling of Discontinuous Objects. *Applied Optics* **36**, 2770-2775.

Jain, K. K. 2003 Lab-on-a-Chip and Microarrays: Discovery and Development. *Pharmacogenomics* **4**, 123-125.

Jones, T. B. 2001 Liquid Dielectrophoresis on Microscale. *Journal of Electrostatics* **51-52**, 290-299.

Kline, S. J. & McClintock, F. A. 1953 Describing Uncertainties in Single-Sample Experiments. *Mechanical Engineering* **75**, 3-8.

Koschmieder, E. L. & Prahl, S. A. 1990 Surface-Tension-Driven Bérnard Convection in Small Containers. *Journal of Fluid Mechanics* **215**, 571-583.

Lam, P., Wynne, K. J. & Wnek, G. E. 2002 Surface-Tension-Confined Microfluidics. *Langmuir* **18**, 948-951.

Linke, H., Alemán, B. J., Taormina, M. J., Francis, M. J., Dow-Hygelund, C. C., Narayanan, V., Taylor, R. P. & Stout, A. 2006 Self-Propelled Leidenfrost Droplets. *Physical Review Letters* **96**, 154502-154501- 154504.

Lyuksyutov, I. F., Naugle, D. G. & Rathnayaka, D. D. 2004 On-Chip Manipulation of Levitated Femtodroplets. *Applied Physics Letter* **85**, 1817-1819.

Miller, K. E. & Synovec, R. E. 2000 Review of Analytical Measurements Facilitated by Drop Formation Technology. *Talanta* **51**, 921-933.

Mizev, A. I. 2004 Experimental Study of the Effect of Gas-Phase Thickness on Stability and Structure of the Flow in a Two-Layer Liquid-Gas System. *Journal of Applied Mechanics and Technical Physics* **45**, 784-787.

Monti, R. & Savino, R. 1996 Correlation between Experimental Results and Numerical Solutions of Navier-Stokes Problem for Noncoalescing Liquid Drops with Marangoni Effects. *Physics of Fluids* **9**, 260-262.

Monti, R., Savino, R. & Tempesta, S. 1998 Wetting Prevention by Thermal Marangoni Effect. Experimental and Numerical Simulation. *European Journal of Mechanics -B / Fluids* **17**, 51-77.

Napolitano, L., Monti, R. & Russo, G. 1986 Marangoni Convection in One- and Two-Liquids Floating Zones. *Naturwissenshaften* **73**, 352-355.

Neitzel, G. P. & Dell'Aversana, P. 2002 Noncoalescence and Nonwetting Behavior of Liquids. *Annual Review of Fluid Mechanics* **34**, 267-289.

Omrane, A., Santesson, S., Aldén, M. & Nilsson, S. 2004 Laser Techniques in Acoustically Levitated Micro Droplets. *Lab on a Chip* **4**, 287-291.

Pasquetti, R., Cerisier, P. & Niliot, C. L. 2002 Laboratory and Numerical Investigations on Bérnard-Marangoni Convection in Circular Vessels. *Physics of Fluids* **14**, 277-288.

Qian, J. & Law, C. K. 1997 Regimes of Coalescence and Separation in Droplet Collision. *Journal of Fluid Mechanics* **331**, 59-80.

Rayleigh, L. 1879 Further Observations Upon Liquid Jets, in Continuation of Those Recorded in the Royal Society's "Proceedings" For March and May. *Proceedings of the Royal Society A* **29**, 71.

Reynolds, O. 1881 On Drops Floating on the Surface of Water. *Chemical News* **44**, 221-222.

Sammarco, T. S. & Burns, M. A. 1999 Thermocapillary Pumping of Discrete Drops in Microfabricated Analysis Devices. *AIChE Journal* **45**, 350-366.

Savino, R. & Monti, R. 1997 Modeling of Non-Coalescing Liquid Drops in the Presence of Thermocapillary Convection. *Meccanica* **32**, 115-133.

Savino, R., Paterna, D. & Lappa, M. 2003 Marangoni Flotation of Liquid Droplets. *Journal of Fluid Mechanics* **479**, 307-326.

Schatz, M. & Neitzel, G. P. 2001 Experiments on Thermocapillary Instabilities. *Annual Review of Fluid Mechanics* **33**, 93-129.

Schwartz, J. A., V., V. J. & C., G. P. R. 2004 Droplet-Based Chemistry on a Programmable Micro-Chip. *Lab Chip* **4**, 11-17.

Servin, M., Marroquin, J. L. & Cuevas, F. J. 2001 Fringe-Follower Regularized Phase Tracker for Demodulation of Closed-Fringe Interferograms. *Journal of The Optical Society of America A* **18**, 689-695.

Servin, M. & Quiroga, J. A. 2001 Isochromatics Demodulation from a Single Image Using the Regularized Phase Tracking Technique. *Journal of Modern Optics* **48**, 521-531.

Smith, M. K. 1995 Thermocapillary Migration of a Two-Dimensional Liquid Droplet on a Solid Surface. *Journal of Fluid Mechanics* **294**, 209-230.

Smith, M. K. & Neitzel, G. P. 2006 Multiscale Modeling in the Numerical Computations of Isothermal Nonwetting. *Journal of Fluid Mechanics* **554**, 67-83.

Sreenivas, K. R., De, P. K. & Arakeri, J. H. 1999 Levitation of a Drop over a Film Flow. *Journal of Fluid Mechanics* **380**, 297-307.

Stone, H. A., Strook, A. D. & Ajdari, A. 2004 Engineering Flows in Small Devices: Microfluidics toward a Lab-on-a-Chip. *Annual Review of Fluid Mechanics* **36**, 381-411.

Sumner, L. B., Wood, A. M. & Neitzel, G. P. 2003 Lubrication Analysis of Thermocapillary-Induced Nonwetting. *Physics of Fluids* **15**, 2923-2933.

Sumner, L. B. S. & Neitzel, G. P. 2001 Oscillatory Thermocapillary Convection in Liquid Bridges with Highly Deformed Free Surfaces: Experiments and Energy-Stability Analysis. *Physics of Fluids* **13**, 107-120.

Takeda, M., Ina, H. & Kobayashi, S. 1982 Fourier-Transform Method of Fringe-Pattern Analysis for Computer-Based Topography and Interferometry. *Journal of Optical Society of America* **72**, 156-160.

Taylor, G. I. 1964 Disintegration of Water Drops in an Electric Field. *Proceedings of Royal Society of London, Series A* **280**, 383-397.

Turns, S. R. 2000 *An Introduction to Combustion: Concepts and Applications.* The McGraw-Hill Company Inc.

Utada, A. S., Lorenceau, E., R., L. D., Kaplan, P. D., Stone, H. A. & Weitz, D. A. 2005 Monodisperse Double Emulsions Generated from a Microcapillary Device. *Science* **308**, 537-541.

van den Doel, L. R., Nagy, P. T., van Vliet, L. J. & Neitzel, G. P. 2004 Regularized Phase-Tracker with Iso-Phase Scanning Strategy for Analysis of Dynamic Interferograms of Nonwetting Droplets under Excitation. *Applied Optics* **44**, 2695-2704.

Weigl, B. H., Bardell, R. L. & Cabrera, C. R. 2003 Lab-on-a-Chip for Drug Development. *Advanced Drug Delivery Reviews* **55**, 349-377.

Wheeler, A. J. & Ganji, A. R. 1996 *Introduction to Engineering Experimentation.* Prentice Hall, Inc.

Whitesides, G. M. & Stroock, A. D. 2001 Flexible Methods for Microfluidics. *Physics Today* 43-48.

Wixforth, A., Stroble, C., Gauer, C., Toegl, A., Scriba, J. & Guttenberg, Z. v. 2004 Acoustic Manipulation of Small Droplets. *Analytical and Bioanalytical Chemicstry* **379**, 982-991.

Xie, J. C., Lin, H., Han, J. H., Dong, X. Q., Hu, W. R., Hirata, A. & Sakurai, M. 1999 Experimental Investigation of Thermocapillary Migration of Isolated Drops. *Advances in Space Research* **24**, 1409-1415.

Yuan, H. & Prosperetti, A. 1999 The Pumping Effect of Growing and Collapsing Bubbles in a Tube. *Journal of Micromechanics and Microengineering* **9**, 402-413.

VITA

Peter Takahiro Nagy (Terayama)

Peter Takahiro Nagy was born in Tokyo, Japan in January 1977 as the first son of a Hungarian father, Imre G. Nagy, and a Japanese mother, Emi Terayama. He attended public elementary school (Ootsukadai Shougakkou), and a private international school (St. Mary's International School) from junior-high school until graduating high school in 1995. He moved to the United States to study at the University of Rochester, in New York, where he received a Bachelor of Science in Mechanical Engineering in June, 1999. Following graduation, he moved to the Georgia Institute of Technology to pursue a doctorate degree in Mechanical Engineering. In his leisure time, he enjoys playing guitar, listening to jazz, reading classic novels, and sipping good beers accompanied by good conversation.